

TECHNISCHE UNIVERSITEIT DELFT

MASTER THESIS

**Development of nanowire-based
fluxonium devices**

Author:
Marta PITA-VIDAL

Supervisors:
Prof. dr. ir. Leo P.
KOUWENHOVEN
Dr. Angela KOU

*In partial fulfilment of the requirements
for the degree of Master of Science in Applied Physics*

February 4, 2019

TECHNISCHE UNIVERSITEIT DELFT

Abstract

Master of Science in Applied Physics

Development of nanowire-based fluxonium devices

by Marta PITA-VIDAL

This thesis presents the design, development and first spectroscopy measurements of nanowire-based fluxonium devices. We demonstrate the strong external flux and gate voltage tunability of their spectrum, which allows to accurately tune their first transition frequency over a range of more than 10 GHz. We also show the nanowire fluxonium resilience to magnetic fields up to 800 mT, demonstrating its compatibility with the creation of Majorana bound states (MBSs) at the junction ends, what would open the door to the exploration of new physics and new technological applications. First, the emergence of MBSs in a nanowire fluxonium would result in new Majorana signatures, obtained by radio-frequency spectroscopy techniques. This would complement the current experimental evidence for the creation of MBSs in semiconducting nanowires and would allow to characterize their coupling energy scales, that are, up to date, unknown. And second, the nanowire fluxonium devices presented here can be used for addressing a qubit whose state is topologically protected from local perturbations. Integrating topological qubits into a cQED platform would solve the currently existing problems of the lack of a universal set of quantum gates and reliable methods for qubit operation and readout, establishing a path for the development of topological quantum computing.

Contents

Abstract	iii
Introduction	1
Outline of the thesis	2
1 Physics behind a nanowire fluxonium	3
1.1 Majoranas as quasiparticle excitations	3
1.1.1 Majoranas in 1D p-wave superconductors	4
1.1.2 Topological quantum computation using Majoranas	6
1.1.3 Majoranas in semiconducting nanowires	8
1.2 Superconducting qubits	14
1.2.1 Josephson junction based qubits	14
1.2.2 Circuit QED	18
1.2.3 Fluxonium	20
1.3 Nanowire fluxonium	28
1.3.1 Nanowire Josephson junction	30
1.3.2 Spectrum of a nanowire fluxonium	34
1.3.3 cQED with a nanowire fluxonium: implementation of quantum gates	37
2 Design and fabrication	41
2.1 NbTiN thin films on Si/SiN	42
2.1.1 Kinetic inductance	42
2.1.2 RF properties	44
2.2 Lumped element readout resonators resilient to magnetic field	46
2.2.1 Narrow strips to minimize the appearance of vortices	46
2.2.2 Artificial pinning sites to trap vortices	48
2.3 Design for E_C and E_L	48
2.3.1 E_C : parallel plate capacitor	49
2.3.2 E_L : superinductance meandering path	49
2.4 Gradiometric design and flux-bias line design	50
2.5 Gate-lines design	52
2.6 Nanowire deposition and junction etch	53
3 Spectroscopy measurements	55
3.1 Measurement setup	55
3.2 S21 measurements	57
3.2.1 E_J dependence	58
3.2.2 External flux dependence	59
3.3 Two-tone spectroscopy	60
3.3.1 E_J and external flux dependence	60
3.3.2 Spectra at different E_J values	61
3.4 In-plane magnetic field compatibility	66

3.4.1	Spectroscopy measurements up to 300 mT	66
3.4.2	Resonator compatibility at higher fields	67
Conclusion and outlook		69
	Search for Majorana signatures	69
	Alternative materials and possible design changes	70
	Other experiments on the Majorana fluxonium platform	71
Acknowledgements		73
Bibliography		75

Introduction

Quantum computing¹ has received increasing attention during the last couple of decades due to its potential applications in a variety of areas. Examples of these are faster search [2] and factorization [3] algorithms, cryptographic solutions for secure communication [4] or an expected computational speedup of simulations of quantum systems [5], [6]. From a scientific perspective, the last may be one of the most appealing promises of quantum computation and would have important consequences in areas like Computational Chemistry, Pharmacology or Material Sciences. Being able to simulate classically intractable systems would lead to a better understanding of the dynamics of complex chemical reactions or of the folding configurations of large molecules like proteins and would help designing medicines for targeted purposes, new materials with specific properties, more efficient catalysts and other chemicals.

The power of a quantum computer resides in the quantum superposition and entanglement properties of its basic constituents, the qubits [1]. A qubit is a quantum system whose state can be any superposition of two orthonormal basis states, $|0\rangle$ or $|1\rangle$. In order to be useful for quantum computation, the qubit state must be addressable for operation and readout and, at the same time, maintain quantum coherence over time scales larger than the operation times. Different qubit candidates compete nowadays to be the leading physical platform for quantum computation. The most relevant solid state examples being semiconducting spin qubits, NV centers in diamond, superconducting qubits involving Josephson junctions and topological qubits. The latter are expected to show long quantum coherence times, due to the intrinsic protection of their state against local noise [7], and are the qubit platform in which we will focus in this work.

A topological qubit is based on the properties of Majorana bound state (MBS) quasiparticles [8]. These quasiparticle excitations are predicted to appear at the edges of some materials when their bulk enters a topological phase [9]. Both the theoretical treatment of MBSs and their experimental realization have been shown to be very challenging. Most efforts until now have been put into the development and optimization of the required materials for realizing MBSs, into computational simulations for understanding the systems and geometries where these quasiparticles are expected to emerge and into the experimental implementation of simple systems to obtain signatures of the existence of MBSs and of their basic properties. During the last years, different works showed strong evidence of the emergence of MBSs at the ends of semiconducting wires and a high quality of the required materials. The field is now ready to take the next step and start working on the realization of more advanced devices.

¹We will not treat in detail the theory behind quantum computing in this work. More information about the topic can be found in reference [1].

Here, we present the first implementation and measurements of one of these new devices, a nanowire fluxonium, which has been made with a two-fold goal. On the one hand, it aims to constitute a system that permits the integration of a topological qubit, as a topologically protected quantum memory, in the well-established architecture of superconducting circuits. On the other hand, it aims to provide new signatures and completely new information about fundamental aspects of Majorana bound states, contributing to the understanding of their physics.

Outline of the thesis

In chapter 1 we will go in detail through the theory behind a nanowire fluxonium. We will introduce both topological qubits and the superconducting quantum circuitry typically used to implement qubits based in Josephson junctions, like fluxonium. We will see how the fluxonium architecture can complete the non-universal set of topologically protected gates on the Majorana qubit and help finding new signatures and information of MBSs. After that, we will dive into the specific design for the device studied in this work. In chapter 2 we will see how to overcome the multiple challenges that one encounters when trying to fabricate a nanowire fluxonium and will explain the reasons behind the specific geometries and materials used for each of the elements that constitute the device. Finally, chapter 3 is about the first characterization measurements carried out on a nanowire fluxonium. We will present the measurement setup for heterodyne detection of the transmitted signal and the different spectroscopy measurements carried out that demonstrate the strong tunability and magnetic field compatibility of our nanowire fluxonium devices, opening the door to many new experiments. Let's get started.

Chapter 1

Physics behind a nanowire fluxonium

As introduced, a Majorana fluxonium brings two important approaches to quantum computing together: topological and superconducting qubits. This chapter aims to give a brief overview of the theory and main experimental achievements in these two fields, before presenting the idea of a nanowire fluxonium.

In section 1.1 we introduce Majorana zero-energy modes (MZMs) and describe their main properties: topological protection and non-Abelian exchange statistics (section 1.1.1). We then focus on their potential in the area of quantum computing (section 1.1.2) and discuss some experimental MZM realizations (section 1.1.3).

Section 1.2 explores a very different topic: superconducting circuit qubits. It starts by very briefly going through the main technological achievements in this area, focusing mainly on the use of Josephson junctions as the non-linear element (section 1.2.1) and on the development of circuit quantum electrodynamics (cQED) to address the qubit (section 1.2.2). Among the various qubit proposals, we go into a bit more of detail for fluxonium. This qubit did not receive as much attention as others, like the transmon, since its development in 2012 [10], but it is ideal for our purposes: finding new Majorana signatures and being able to address topological qubits.

Only by the end of the chapter we will be ready to meet the awaited nanowire fluxonium. In section 1.3 we explain how to couple a Majorana qubit and a fluxonium together. We also go in detail through the Hamiltonian description and expected spectrum for this device (section 1.3.2) and explain how to carry out coherent state transfer between the topological qubit and the fluxonium (section 1.3.3).

1.1 Majoranas as quasiparticle excitations

The name of Majorana particles comes from 1937, when Ettore Majorana found a real solution to Dirac's equation predicting the existence of a fermionic elementary particle which would be its own antiparticle and which would therefore have zero energy [11]. Though Ettore Majorana had particles in mind when he found the solution, quasiparticle excitations at the edges of p-wave superconductors can also be their own antiparticles and have zero energy [12]–[17]. These are known as Majorana zero-modes (MZMs) or Majorana bound states (MBSs). Their properties, analogous to the ones of Majorana's elementary particles, are from where MZMs take their name.

Their theoretical prediction in a condensed matter system in 1991 by Moore and Read [18] and the simple one-dimensional model introduced by Kitaev in 2001 [9] triggered the appearance of several proposals for the experimental realization of such states in diverse physical systems. One of the proposals suggested the use of semiconducting nanowires with strong spin-orbit coupling proximitized by a conventional s-wave superconductor [19], [20]. This is the system in which the first Majorana signatures were found [21] and also the one that we will use in this work.

1.1.1 Majoranas in 1D p-wave superconductors

A MZM is a quasiparticle excitation which is its own hole. If γ is its annihilation operator, this means that it must fulfill $\gamma^\dagger = \gamma$. The simplest way to achieve this in an electron-hole condensed matter system it having γ be of the form

$$\gamma = c^\dagger + c \quad (1.1)$$

where c is the electron annihilation operator. This expression has a striking similarity to the definition of a Bogoliubov quasiparticle in BCS formalism for s-wave superconductors [16], [22]

$$\gamma_\sigma = uc_\sigma^\dagger + vc_{\sigma^*} \quad (1.2)$$

where c_σ is the annihilation operator of a fermion with spin $\sigma = \uparrow, \downarrow$. The main difference between equation 1.1 and equation 1.2 is that, for an s-wave superconductor, Cooper pairs are a singlet state formed by fermions with opposite spin, while the two components of a MZM should have equal spin. This means that, even if superconductivity seems to help in order to obtain MZMs, conventional s-wave superconductivity is not enough. A system that would be capable of hosting MZMs would be a superconductor with triplet pairing (a p-wave superconductor in the case of one dimension (1D)).

Kitaev's toy model [9], a tight-binding Hamiltonian for fermions with p-wave pairing, is the simplest model showing that a 1D spinless p-wave superconductor can host unpaired MZMs at its ends. The Hamiltonian for the continuum version of Kitaev's model reads

$$\mathcal{H} = \int dx \left\{ \psi^\dagger(x) \left(\frac{\partial_x^2}{2m} - \mu \right) \psi(x) + \Delta (\psi^\dagger(x) \partial_x \psi^\dagger(x) + h.c.) \right\}. \quad (1.3)$$

Here, $\psi(x)$ annihilates a fermion at position x , μ denotes the chemical potential, m the effective electron mass and Δ the superconducting pairing potential.

The Bogoliubov-de Gennes (BdG) form of this Hamiltonian, for a Nambu spinor ordered as $\Psi(x) = (\psi(x), \psi^\dagger(x))^T$ is

$$H_{BdG} = \left(\frac{p^2}{2m} - \mu \right) \tau_z + \Delta p \tau_y, \quad (1.4)$$

where τ_i , with $i = x, y, z$, are the Pauli matrices acting in the electron-hole space and $p = -i\hbar\partial_x$ is the momentum operator.

The excitation energies obtained by diagonalizing H_{BdG} are

$$E_p = \pm \sqrt{\left(\frac{p^2}{2m} - \mu \right)^2 + \Delta^2 p^2} \quad (1.5)$$

which are always gapped excepting when $\Delta = 0$ for positive μ , or when $\mu = 0$. These parameter points where the gap closes correspond to topological quantum phase transitions. If one of these parameters, μ or Δ , varies continuously in space going from negative to positive values, a domain wall is generated at the x point at which it passes through zero. In Box 1 we see, combining the procedures in references [16] and [23], that such domain wall hosts a zero-energy quasiparticle excitation that is exponentially localized at the interface between the topological and the trivial regions. Furthermore, we prove that its annihilation operator γ obeys the Majorana property $\gamma^\dagger = \gamma$, showing therefore that this localized quasiparticle is a Majorana mode.

Box 1 - MZM at a topological-trivial interface of a 1D p-wave superconductor

If the chemical potential varies linearly in space^a, $\mu(x) = \alpha x$, the BdG Hamiltonian in equation 1.4, in real space and expanded to first order in p (because relevant momenta at the domain wall are small), reads

$$H_{BdG}(x) = -\alpha x \tau_z + \Delta \tau_y i \partial_x \quad (1.6)$$

In order to look for zero energy excitations, we want to solve the equation $H_{BdG}(x)\Phi(x) = 0$. Using the commutation relations of Pauli matrices, specifically $\tau_y \tau_y = 1$ and $\tau_y \tau_z = 2i \tau_x$, we have

$$2\alpha x \tau_x \Phi(x) = \Delta \partial_x \Phi(x). \quad (1.7)$$

Therefore we have

$$\Phi(x) = \exp\left(\frac{\alpha x^2 \tau_x}{\Delta}\right) \Phi(0), \quad (1.8)$$

and expanding on the eigenbasis of τ_x

$$\Phi(x) = u_+ \exp\left(\frac{\alpha x^2}{\Delta}\right) \begin{pmatrix} 1 \\ 1 \end{pmatrix} + u_- \exp\left(\frac{-\alpha x^2}{\Delta}\right) \begin{pmatrix} 1 \\ -1 \end{pmatrix}. \quad (1.9)$$

For $\Phi(x)$ to be normalizable, either u_+ or u_- will be zero, depending on whether α is positive or negative, respectively. In any case we obtain a wave function **localized at $x = 0$** , at the topological phase transition, with two exponential tails on the sides. This is shown schematically in figure 1.1.

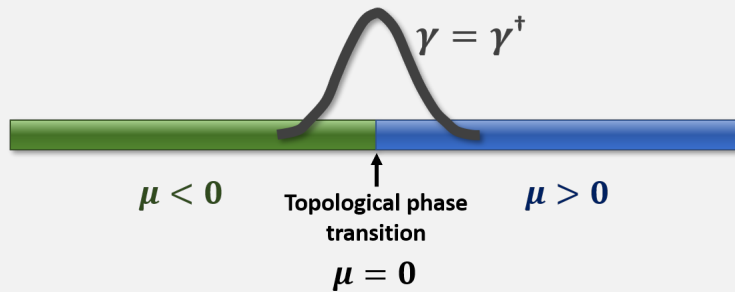


FIGURE 1.1: **Schematic of a MZM at a topological phase transition.** Green and blue represent regions of a system with Hamiltonian 1.3 in different topological phases.

For a normalized eigenspinor $\Phi(x)$, one can calculate its Bogoliubov operator in terms of the original electron operators as [16]

$$\gamma = \int dx \Phi^\dagger(x) \Psi(x). \quad (1.10)$$

We do that in order to check that this zero-energy bound state is actually a Majorana mode.

$$\gamma = \int dx \Phi^\dagger(x) \Psi(x) = \begin{cases} \int dx \sqrt{\frac{\Delta}{\alpha\pi}} e^{i\theta_-} \exp\left(\frac{-\alpha x^2}{\Delta}\right) (\psi(x) - \psi^\dagger(x)) & \text{if } \alpha > 0 \\ \int dx \sqrt{\frac{\Delta}{-\alpha\pi}} e^{i\theta_+} \exp\left(\frac{\alpha x^2}{\Delta}\right) (\psi(x) + \psi^\dagger(x)) & \text{if } \alpha < 0 \end{cases}. \quad (1.11)$$

If $\theta_+ = 0$ or π and $\theta_- = \pi/2$ or $3\pi/2$, we have, in both cases $\gamma^\dagger = \gamma$. So the quasiparticle excitations appearing at the interface are, up to a phase factor, Majorana bound states.

^aThe proof is analogous for any other dependence $\mu(x)$, with the only condition of it being positive at one side of the domain wall and negative at the other side.

1.1.2 Topological quantum computation using Majoranas

MZMs are considered to be good candidates for low-decoherence quantum information processing mainly due to two of their properties. First, they are **spatially separated** and therefore, if the qubit state is encoded in the ground-state manifold of a system with several MZMs, it will be protected from local perturbations due to this spatial separation. Second, they exhibit **non-Abelian exchange statistics**: when the positions of two Majorana bound states are exchanged, the many-body state of the system undergoes a unitary rotation in the ground-state manifold, and these transformations, in general, do not commute. These rotations, which are insensitive to small variations on the path and final position of the MZMs, are good candidates for quantum gates over the qubit state.

Qubit state and protected operations

Since MZMs cost no energy, the presence of N pairs of non-interacting Majorana zero modes in a system results in a degenerate ground state. The only thing that distinguishes different MZMs is their position, we label each of them with $i = 1, \dots, 2N$. One can not assign a number quantum state to a MZM, however, two Majoranas can be paired forming a fermionic mode. For $j = 1, \dots, N$,

$$c_j = \frac{1}{2}(\gamma_{2j-1} + i\gamma_{2j}) \quad (1.12)$$

is a fermionic operator¹, which can be empty, $n_j = c_j^\dagger c_j = 0$, or occupied, $n_j = 1$. The quantum states of N pairs of Majoranas with fixed fermionic occupations can be represented as $|n_1, n_2, \dots, n_N\rangle$ and constitute a basis of the degenerate ground-state

¹One can check that this is actually a fermionic operator by seeing that it fulfills the fermionic anticommutation relations $\{c_j, c_k\} = \{c_j^\dagger, c_k^\dagger\} = 0$ and $\{c_j, c_k^\dagger\} = \delta_{jk}$.

manifold. A general superposition state of the system can be written in this basis as

$$|\Psi\rangle = \sum_{n_j=0,1} \alpha_{n_1, n_2, \dots, n_N} |n_1, n_2, \dots, n_N\rangle, \quad (1.13)$$

with complex coefficients $\alpha_{n_1, n_2, \dots, n_N}$. In principle, the dimensionality of the manifold of all possible ground states is then 2^N . A system with $2N$ MZMs can therefore encode the quantum state of N qubits.

The most important property of quantum information encoded in the the Majorana manifold is its topological protection. Since its state depends only on the parity, or occupation, of non-local fermions, split among Majoranas located at different points, no local perturbation can change this quantum state and cause decoherence. The main cause of decoherence for this type of qubits would instead be an uncontrolled change in total fermion parity, normally called quasiparticle poisoning.

One way of coherently changing the state of the system, and therefore implementing a **quantum gate**, is by explicitly moving the non-interacting MZMs around each other [8]. The adiabatic exchange of two Majoranas, γ_j and γ_k , is equivalent to the application of a unitary operator $U_{j,k}$ on the state of the system [23]–[25],

$$U_{j,k} = \exp\left(\pm \frac{\pi}{4} \gamma_j \gamma_k\right) = \frac{1}{\sqrt{2}}(1 \pm \gamma_j \gamma_k), \quad (1.14)$$

with the $+$ or $-$ sign depending on whether the exchange is carried out clockwise or counterclockwise. Therefore, exchanging two Majorana modes leads to an, in general, non-trivial rotation of the state in the ground state manifold. These operations are normally called braiding operations. The way of carrying out this transformation is non-local and the final result depends only on the topology of the exchange and not on details of the specific path followed by each of the quasiparticles. This is why quantum gates based on braiding are protected against local perturbations.

Physically moving MZMs around is the only way of braiding *non-interacting* MZMs. However, there are alternative experimental approaches for the realization of non-abelian braiding operations that involve temporarily turning on and off interactions between them. This can be done, for example, by using gate voltages to control the tunnelling coupling between adjacent MZMs [26]. A different proposal suggests to use a magnetic field control parameter rather than an electrostatic to tune the Coulomb interaction between pairs of Majoranas, controlling the flux trough the split junction of a transmon coupled to them [27]. In these cases the braiding operation is also topologically protected, because it depends on the sequence of Majorana couplings and not on details of the sequence timing [27].

Even if there are several challenging points for the experimental implementation of braiding, it seems reasonable that, due to the existence of different alternative approaches, if big efforts were put towards this goal, it could be implemented in the coming years. However, an important aspect to consider regarding the quantum states that can be achieved by carrying out braiding operations is that the total fermion parity of the Majorana system is fixed. The parity of a single fermionic state j , $P_j = 2n_j - 1$, can be either -1 or $+1$ depending on its occupation. One can express P_j in terms of the Majorana operators as $P_j = i\gamma_{2j-1}\gamma_{2j}$. The total fermion parity of the system, P , is just the product of all the P_j 's, $P = i^N \prod_{j=1}^N \gamma_{2j-1}\gamma_{2j}$. If this parity is fixed, then only half of the degenerate ground-state manifold is accessible. That would be a problem when trying to realize quantum gates. Braiding operations

alone can not change P , so they can not constitute a universal set of gates if one takes as the qubit state the state of the Majorana system defined above (equation 1.13). A simple example of an operation that is not accessible by braiding is a single qubit rotation [7], which would change the parity of only one of the fermionic states.

Hybrid qubits, unprotected operations and logical qubits

Many different proposals suggest ways of overcoming the problem of the lack of a universal set of braiding operations. Some combine a topological qubit with extra non-topological ways of implementing gates [28], [29]. It is possible, for example, to couple the fermion parity of a part of a topological qubit to a flux qubit [28] or to a transmon [29] to implement parity protected rotations, and also to readout the qubit. The most recent proposals, however, define elementary units, or logical qubits, containing four Majoranas γ_i , $i = 1, 2, 3, 4$ [29]–[33]. In this case, the computational space has fixed total parity, so parity conservation in the Majorana system is an advantage rather than a problem. In these proposals, the basis states of the qubit, $|+\rangle$ and $|-\rangle$, are encoded in the parity of the first pair of Majoranas $i\gamma_1\gamma_2$. Pauli operators can be expressed as a function of γ_i as

$$\hat{x} = -i\gamma_2\gamma_3, \quad \hat{y} = i\gamma_1\gamma_3, \quad \hat{z} = -i\gamma_1\gamma_2. \quad (1.15)$$

Individually addressing different pairs of Majoranas allows to initialize, manipulate and readout the qubit state. In references [32] and [33], for example, quantum dots are used to selectively address pairs of Majoranas and achieve a universal set of gates, some of them topologically protected.

In this work we will explore a hybrid qubit proposal, first suggested by Pekker *et al.* in 2003 [30]. It involves coupling a logical topological qubit to a fluxonium, a type of non-topological superconducting qubit that can reliably be rotated and read out and that will be presented in section 1.2. In section 1.3, we will go into more detail on how to integrate a fluxonium and a topological qubit together and on how to control their interaction to be able to implement gates and read out the topological qubit state.

1.1.3 Majoranas in semiconducting nanowires

In section 1.1.1 we saw that a Majorana bound state can appear at the interface between a topological region and a trivial region of a spinless p-wave superconductor. However, p-wave superconductors are rare in nature and not as common as superconducting materials with s-wave pairing. Luckily, several proposals presented engineered physical systems with Hamiltonians topologically equivalent to the one in equation 1.4, obtained by combining materials with different properties. In this section we introduce one of the simplest ones, a superconductor proximitized semiconductor nanowire with a strong spin-orbit coupling [19], [20], which will be the platform used in this work.

Main physical ingredients

In any known physical system, electrons have spin $\frac{1}{2}$. Therefore, any realistic Hamiltonian must include a spin degree of freedom. In this section we will use σ to denote Pauli matrices acting on spin space, while τ Pauli matrices will still be acting on particle-hole space.

For a Hamiltonian with time-reversal symmetry, states with opposite spin are degenerate and form Kramer's pairs. In order to break this degeneracy and be able to obtain an effectively spineless system, time-reversal symmetry must be broken. This can be done by applying magnetic field, which breaks Kramer's pairs by **Zeeman effect**. We will include a $V_Z\sigma_z$ term in the system's Hamiltonian, where $V_Z = g\mu_B B/2$ is the applied Zeeman field, with B the applied magnetic field, g the g -factor of the semiconductor and μ_B is the Bohr magneton.

Furthermore, for regular superconductors, superconducting pairing is of s-wave type, it couples electrons of opposite spin. One way of effectively obtaining p-wave pairing is using a material with strong **spin-orbit interaction** and coupling it to an **s-wave superconductor**. By proximity effect [34], [35], superconductivity will be induced in the semiconductor. Spin-orbit interaction gives rise to split bands with momentum dependent spin direction that, together with the induced superconductivity and the gap open by Zeeman effect, will result on an effective p-wave pairing.

The BdG Hamiltonian for a physical system with these characteristics, with a Nambu spinor ordered as $\Psi(x) = (\psi_\uparrow(x), \psi_\downarrow(x), \psi_\downarrow^\dagger(x), -\psi_\uparrow^\dagger(x))^T$, is

$$H_{BdG} = \left(\frac{p^2}{2m} - \mu + \alpha p \sigma_x \right) \tau_z - V_Z \sigma_z + \Delta \tau_x. \quad (1.16)$$

Here, the last term represents spin-singlet pairing, without momentum dependence, inherited from the s-wave superconductor by proximity effect. Δ is the induced pairing potential in the semiconductor. As before (eq. 1.3), μ denotes the chemical potential and m the effective electron mass. α is the strength of the Rashba spin-orbit coupling.

We have written the spin-orbit field along the x-direction, perpendicular to the Zeeman field, which is along the z-direction. The spectrum of Hamiltonian 1.16 is shown in figure 1.2 c) and d) for two different values of V_Z . The rest of spectra in figure 1.2 correspond to different parameters of the Hamiltonian being zero. As we see, by applying a magnetic field perpendicular to the direction of the spin-orbit one can separate spins by Zeeman effect and open a gap at zero momentum. If we tune μ to be in the gap, there is a single band crossing the Fermi points p_F and $-p_F$ in figure 1.2, therefore the system will effectively behave as a spineless system. Since spin-orbit interaction rotates the spin of this band as a function of momentum, the two Fermi points have opposite spin components in the direction of B_{SO} and s-wave pairing induces pairing between them. The resulting state will be effectively a p-wave superconductor.

By changing either the chemical potential μ or the Zeeman splitting V_Z the system can enter or exit the topological regime. The condition for topological superconductivity is $|V_Z| > \sqrt{\Delta^2 + \mu^2}$ [20].

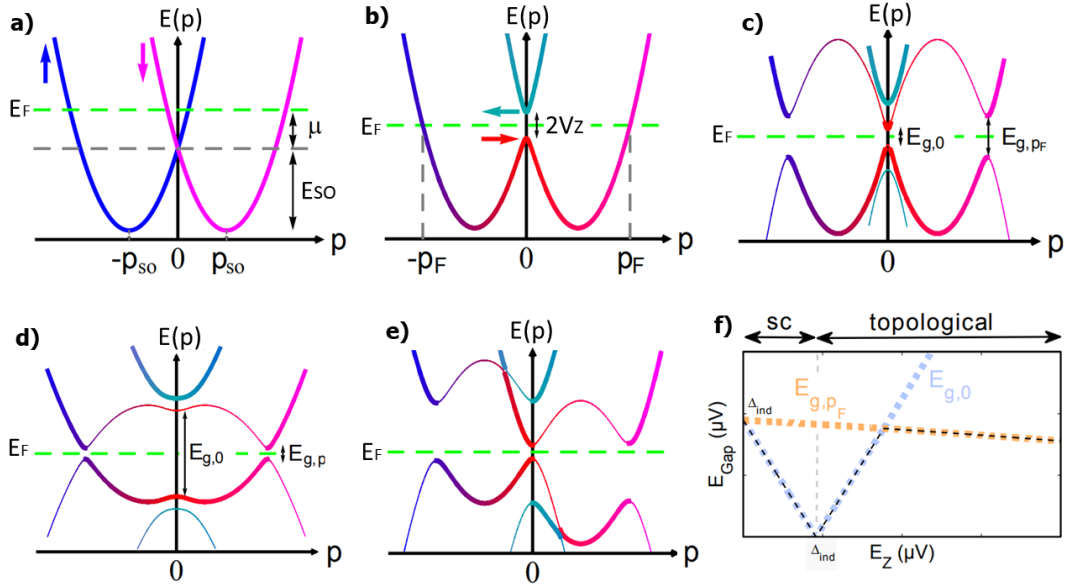


FIGURE 1.2: **Energy spectrum for Hamiltonian 1.16.** In panels a) - e), different spin flavours are indicated by different colours. Dark blue and magenta indicate opposite spins in the direction of the S-O effective field B_{SO} . Red and light blue indicate opposite spins in the direction of the external magnetic field B . a) For $B = 0$ and $\Delta = 0$. Bands with opposite spin in the B_{SO} direction split towards positive and negative momenta. The chemical potential μ is measured with respect to the split bands crossing. b) For $\Delta = 0$. B , perpendicular to the direction of B_{SO} , opens a gap with magnitude $2V_Z$ at the bands crossing. If the applied field was parallel to B_{SO} , rather than perpendicular, then the two parabolas in figure a) would shift vertically in different directions without opening a gap. c) With the incorporation of s-wave pairing, gaps open at the crossings between the hole lines (thin) and the electron lines (thick). d) Same as c) but increasing the magnitude of B . The gap at $p = p_F$, and not the one at $p = 0$, dominates now the overall gap Δ_{ind} . e) Same as d) but now with B having parallel and perpendicular components. f) Gap at $p = 0$ is shown in blue. It decreases with B until it fully closes at the topological transition and then increases again. Orange shows the gap at $p = p_F$ and black indicates the overall gap size. Figure adapted from [36].

Material platforms

To engineer a system with the required properties presented above, it is necessary to find separate materials that individually fulfill each of them. In this work we will use semiconducting nanowires proximitized with a thin film of superconductor on their surface.

A typical **superconductor** used for this purpose is thin proximitized Al, even if NbTiN or other superconductors can also be used. The main challenge is having clean and homogeneous superconductor-semiconductor interfaces to obtain a good induced gap. Experimental studies show that semiconducting nanowires in proximity to Nb or Al can inherit, by proximity effect, a superconducting gap of size comparable to the gap of the superconductor [34], [35]. However, the softness of the gap (i.e. the detrimental conductance inside the gap coming from unwanted subgap states) depends strongly on the amount of disorder in the semiconductor-semiconductor interface. If the gap is softer, the probability of thermal quasiparticle excitations increases, so it is important to try to reduce as much as possible the native oxide and other defects on the surface of the nanowire before Al deposition. For the first Majorana experiments in nanowires, the superconductor was deposited on

chip, so the native oxide on the surface of the wire had to be etched away before deposition [21], [36]. Now, much cleaner interfaces and harder gaps can be achieved using epitaxial thin aluminum films grown *in situ* on the nanowire surface without breaking vacuum [37].

Typically used **semiconducting materials** are InAs or InSb nanowires with spin-orbit energy $E_{SO} = m\alpha^2/2$ between 0.2 and 1 eVÅ for both of them and g -factor of 8 – 15 and 40 – 50 respectively [17]. The material's g -factor is one of its most relevant parameters. A large effective Zeeman gap is favourable for protecting the system from small perturbations. It can in principle always be improved by applying a stronger magnetic field B . However, if B approaches the s -wave superconductor critical field it can detriment the induced superconductivity and the relative effect of the spin-orbit coupling. This is why large g -factors, which give greater Zeeman splitting for the same external field, are beneficial. The magnitude of E_{SO} , which measures the energy of the bands crossing point with respect to the bottom of the band, is also important. The gap at non-zero momentum in panels c) and d) of figure 1.2 is proportional to the ratio E_{SO}/V_Z [38]. It is easy to find an intuitive explanation for this, thinking about the reason why this gap opens. This happens because induced superconductivity couples opposite spin components of electrons at p_F and $-p_F$. Strong V_Z intensifies the spin component in the direction of the applied field, which is independent from momentum, while strong E_{SO} intensifies the spin component in the direction of the effective B_{SO} field, which is opposite for p_F and for $-p_F$. This is why E_{SO} contributes to opening the gap at $\pm p_F$ while V_Z contributes to closing it. Since V_Z has to be large, it is also necessary to have a large spin-orbit energy.

In this work we use Vapour-Liquid-Solid (VLS) InAs nanowires with epitaxial Al [37] covering two out of the six wire facets. Development of the VLS growth techniques during the last 50 years resulted in the current availability of high quality crystalline nanowires of this and other materials. The typical length of InAs wires can easily be of around 8 μm . InSb VLS nanowires of diameters of around 80 nm, but with typical lengths shorter than the ones of InAs wires, are also available and often used for Majorana research [39]. However, its low surface energy makes it more difficult to start the growth than for InAs. The main problem of short nanowires, in this case of around 3 μm , is that, if MZMs emerge at their ends, they are closer to each other than in InAs wires. This can make the MZMs wavefunctions overlap, and therefore hybridize and split away from zero energy [40]. This effect could hinder some of the characteristic signatures and be also detrimental for most MZMs applications. Something special about InSb wires is that recent development allows for the creation of wires with shadow junctions [41]. These type of wires are useful when one wants to study a system with a Josephson junction. In this technique, a second wire is used to create a shadow on the proximitized aluminum during deposition. Since these junctions are directly made after nanowire growth, without extra aluminum etching steps, they can be more homogeneous and with less impurities and defects.

As we see, different types of nanowires have different advantages and disadvantages. On the one hand, InSb is a very promising option, due to its combination of a large g -factor with a large spin-orbit interaction. However, InAs wires offer other advantages. As we said, they are in general longer. Furthermore, they are resilient to much higher temperatures during processing than InSb. This means that standard processing techniques can be used for InAs wires, while new processes have to be created and optimized in the case of InSb. Time will say which of the two materials

is more suitable for Majorana applications.

When dealing with real nanowires there are several aspects to take into account that are not included in the idealized one-dimensional model in equation 1.16. The combination of B and μ values that bring the wire into the topological regime will be more complex than the simple quadratic relation $|V_Z| > \sqrt{\Delta^2 + \mu^2}$ found before (see figure 1.3 a)) [42]–[45]. One first aspect to consider is the three-dimensionality of real wires. **Several bands** should be included when modeling a real system and will give rise to several topological regions in B - μ space, corresponding to different bands meeting or not the topological condition (see figure 1.3 b)). Other physical aspects that have a big impact on the B - μ topological phase diagram are the **electric field and charge density distributions** inside the nanowire. Rashba spin-orbit interaction depends strongly on the electric field direction and magnitude. Its strength will change for different gate voltages and it will have a position dependence due to inhomogeneous electric field inside the wire. Regarding the charge distribution, the strength of coupling to the superconductor, and therefore to the induced superconducting gap, will be determined by the regions where the density of states is accumulated in the wire cross section. Including in numerical models a realistic geometry and an appropriate treatment of electrostatics and the superconductor/semiconductor interface has therefore a big impact on the topological phase diagram and on the magnitude of the topological gap [44], [45]. Another physical phenomenon that is not considered in the simplified models is the magnetic field **orbital effect**, which can increase the effective g -factor by a factor of 2 or 3, as shown in references [46] and [47]. This effect results in more complex phase diagrams, but also in the need of lower magnetic field magnitudes to enter the topological regime (see figure 1.3 c)).

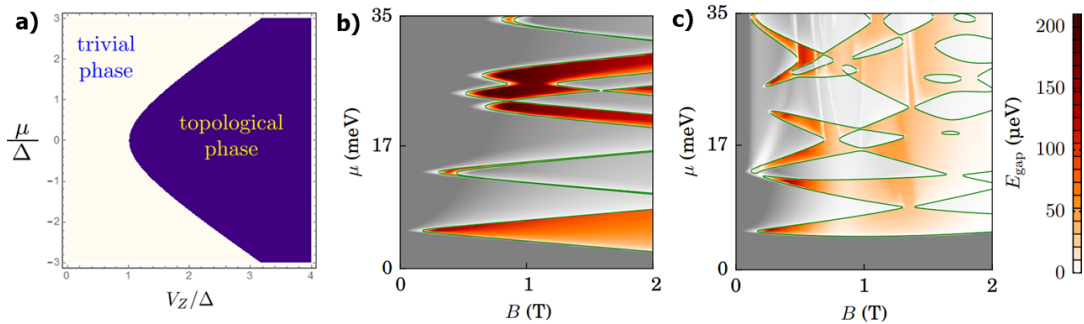


FIGURE 1.3: **Topological phase diagram of idealized and realistic nanowire systems.** **a)** Parabolic topological phase condition calculated analytically from an idealized model $|V_Z| > \sqrt{\Delta^2 + \mu^2}$. Figure adapted from [17]. **b)** and **c)** Phase diagrams for a model including realistic treatment of the cross-section geometry and induced superconductivity. Orbital effect is considered in panel c) but not in b). Color scale shows the magnitude of the gap, with orange and grey scales indicating topological and trivial regions respectively. Topological phase transitions are shown in green. Figures **b)** and **c)** are adapted from [43].

One last experimental aspect to consider is the direction of the applied **magnetic field**. As we said, it must be applied in a direction perpendicular to the one of the S-O effective field B_{SO} . This direction is in general unknown in a real setup. However, we know it is the cross product of the momentum, which is along the wire, and the electric field. Therefore, applying the external magnetic field parallel to the direction of the wire ensures that it is perpendicular to B_{SO} . Aligning the field along the wire

has also been shown to be beneficial for the topological gap [43], due to conservation laws arising from mirror symmetries. This is what is typically done and what we will do throughout this work. This direction will be denoted by z .

Experimental signatures of Majoranas

The first type of experiments looking for MBS signatures were tunneling conductance measurements of the density of states (DOS) at one end of the nanowire [21], [36], [48]. In these experiments, differential tunnel conductance was measured at low bias voltages applied between a metallic probe and the superconducting nanowire, and a small gate was used to open or close the tunnel junction in between. The measured conductance comes from Andreev reflection processes at the normal metal - superconductor interface. For a wire in the trivial regime there are no states inside the gap, so conductance should be suppressed at low bias. However, resonant tunneling into a local Majorana bound state at the end of the wire is expected to result in a $2e^2/h$ -quantized conductance peak at the center of the gap, at zero bias. This signature allows to distinguish the topological and trivial phases. Electrostatically tuning the chemical potential μ of the wire with a gate and increasing the external magnetic field B , a **zero-bias peak** emerges at the critical value $B_C = \sqrt{\Delta^2 + \mu^2}$, indicating a trivial to topological transition [21], [36], [48]. Stronger evidence of this transition has recently been given by the observation of the expected $2e^2/h$ -quantized conductance peaks at zero-bias in InSb/Al nanowires [49].

Even if these signatures can arise from the presence of MZMs, they can not be conclusive, since there are alternative explanations for the appearance of zero-bias conductance peaks coming from trivial Andreev bound states in non-topological wires [50], [51].

A second type of signature of MZMs, more relevant for the type of devices studied in this work, is the unconventional **4π -periodic Josephson effect** characteristic of junctions between two topological superconductors. The excitation spectrum of a Josephson junction (JJ) between superconductors in the trivial state is 2π -periodic in phase difference across the junction (or, equivalently, $h/2e$ -periodic in the flux threaded through a loop containing the junction). Therefore all physical properties of the junction have the same periodicity. However, when two topological superconductors form a JJ, MZMs appear at both ends and give rise to coherent single-electron tunneling processes. In this case, the Josephson effect becomes, for fixed fermion parity, 4π -periodic instead of 2π -periodic [9], [52], [53].

Measuring this type of periodicity change when the wire enters the topological regime can provide new evidence of the generation of MZMs and complement the zero-bias peaks measurements. It can in principle be probed by measuring the periodicity of any physical quantity that depends on the excitation spectrum of the junction. One option is studying the Josephson current $I = 2e \frac{\partial E}{\partial \phi}$, where ϕ is the superconducting phase difference across the JJ and E is the energy dispersion of the junction excitations. However, parity changes can hinder the observation of this effect, so supercurrent measurements should be performed at a frequency higher than the characteristic frequency of quasiparticle poisoning. One way of doing this is studying the ac Josephson effect in the presence of a bias voltage across the junction. In the case of 4π -periodicity, the Josephson frequency of the generated ac current is half of the usual one for trivial superconductors at both sides of the JJ [54]. This change in Josephson frequency has recently been shown as a function of magnetic

field [54], complementing the set of experimental signatures of topological superconductivity in semiconducting nanowires.

The experimental observation of this effect in real semiconducting nanowires with many channels is challenging because typically only one channel enters the topological regime and gives the 4π effect, while every non-topological channel contributes to the supercurrent with 2π -periodicity, which can hinder the 4π -periodic part. The device studied in this work, the nanowire fluxonium, is compatible with the experimental observation of this 4π -periodic Josephson effect, even in the presence of several 2π -periodic trivial channels. Experiments carried out in this device can furthermore determine the magnitude of the interaction energy between MZMs sitting at both sides of the junction [30]. The interest of this device lays therefore not only on its applications for quantum computation, but also in its ability to provide new signatures of topological superconductivity and contribute to the characterization of JJs hosting MZMs. The nanowire fluxonium will be explained in detail in section 1.3.

1.2 Superconducting qubits

The idea of using Josephson junctions (JJs) to realize quantum bits started already at the end of the 90's [55], with the creation of the first charge [56], phase [57] and flux [58] qubits. But it was mainly after the Yale proposal for using a circuit Quantum Electrodynamics (cQED) architecture to address this type of qubits [59] when most efforts were put into the development of this new technology [60] [61]. Since then, the celebrated transmon qubit was developed [62] and several milestones were achieved. Two qubits were coupled using a coplanar waveguide transmission line [63], single and multiple qubit gates were implemented [64] and simple quantum algorithms were experimentally demonstrated [65]. In the last years, efforts were put on finding geometries that allow scaling up easily and, above all, on increasing gate fidelity and coherence times.

cQED has proven to be one of the best developed architectures for quantum computing. The basic element of superconducting qubits, which determines their physics due to its 2π -periodic Josephson effect, is the Josephson junction. Substituting a conventional JJ with a junction hosting Majoranas at its ends should therefore fundamentally alter the behaviour of these qubits. This would allow to investigate the behaviour of topological phases of matter taking advantage of an already well established technology. This is what we plan to do. But let's start by better understanding the physics behind superconducting qubits, with an emphasis on fluxonium.

1.2.1 Josephson junction based qubits

The Josephson junction is the key element of superconducting qubits, because it brings non-linearity into the system's Hamiltonian, which results in an anharmonic distribution of eigenenergies that would otherwise be evenly spaced. In this way, the two lowest energy levels $|g\rangle$ and $|e\rangle$, whose transition can be addressed independently from other transitions, define the two basis states of the superconducting

qubit.

Josephson junction based qubits can be classified in two big groups, depending on the topology of the space where the relevant degrees of freedom are defined. These degrees of freedom are the gauge-invariant superconducting phase difference across the junction ϕ and its conjugated reduced charge variable n , the number of Cooper pairs transferred through the junction

$$n = -i\hbar \frac{\partial}{\partial \phi}, \quad \phi = i\hbar \frac{\partial}{\partial n}. \quad (1.17)$$

If the superconductors at both sides of the junction are isolated from each other, one can be seen as a floating island and the other as a superconducting reservoir. In this case the phase difference is only defined modulo 2π , since every physical property of the junction is 2π -periodic, as we saw in the previous section. Its conjugated charge n , the number of Cooper pairs occupying the island, must be an integer. A circuit model for this configuration is shown in figure 1.4 a), where the two separate pieces of superconductor (grey) are coupled via a Josephson junction (red) and a coupling capacitor (blue).

The situation changes if the two sides of the junction are shunted together by a piece of superconductor with a certain (finite [66]) inductance (see figure 1.4 b)). Two ϕ values differing by 2π are not physically equivalent anymore, so the phase is defined in the entire real axis. Furthermore, the number operator n has now a continuous spectrum due to the possibility of continuously displacing the Cooper-pair condensate towards one side of the junction.

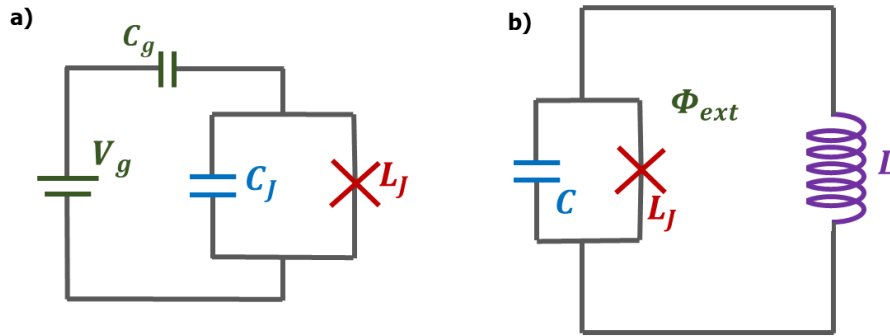


FIGURE 1.4: **Superconducting qubits circuit models.** **a)** Circuit model for the Cooper pair box and for the transmon, corresponding to Hamiltonian 1.20. **b)** Circuit model for the rf SQUID and for the fluxonium, corresponding to Hamiltonian 1.28.

We will now take a closer look to these two topologically distinct classes of qubits, building a Hamiltonian to describe their physics. We ignore for now the auxiliary circuitry for qubit control and readout, which will be presented in the next section.

The Josephson and capacitive elements are common for both classes of qubits. If the superconducting gap Δ is greater than other relevant energy scales of the system, such that no thermal fermionic excitations appear, only Cooper pairs tunnel coherently across the junction and the Josephson element can be incorporated in the circuit Hamiltonian via the Josephson energy associated with this transmission. For

a typical superconductor-insulator-superconductor (SIS) JJ the transmission probability of all Andreev bound states in the Josephson junction is low² and the junction potential has a cosine dependence on ϕ [67]

$$V_{SIS} = -E_J \cos(\phi). \quad (1.18)$$

Here, E_J is the **Josephson energy**, proportional to the junction critical current. E_J is a measure of the ability of Cooper pairs to tunnel through the junction and can be associated to an effective non-linear inductance $L_J = \Phi_0^2 / (2\pi)^2 E_J \cos(\phi)$.

The capacitive element can be described by the **charging energy** E_C ,

$$E_C = \frac{e^2}{2C}, \quad (1.19)$$

which sets a second energy scale of the system. For the case of island qubits, $C = C_g + C_J$ is the total capacitance of the island and has contributions from both the capacitance of the junction C_J and the capacitance between the island and a gate used to electrostatically tune its charge C_g . For inductively shunted qubits C is simply the capacitance across the junction.

Island qubits: the Cooper pair box

One of the conceptually simplest qubits containing a JJ is the Cooper pair box. It consists of a superconducting island coupled via a Josephson junction to a superconducting electrode (figure 1.4 a)). The circuit Hamiltonian in this case can be directly written combining the Coulomb and Josephson energy contributions presented above [68], [69]

$$H_C = 4E_C(n - n_g)^2 - E_J \cos(\phi). \quad (1.20)$$

Here, $n_g = C_g V_g / 2e$ is a dimensionless charge induced by the gate with potential V_g , also called offset charge. The factor 4 multiplying the charging energy comes from the fact that the energy cost of transferring a Cooper pair through the junction is 4 times larger than for transferring a single electron.

If the capacitance C is low, which is the typical regime for a Cooper pair box, then the charging energy dominates over the Josephson energy E_J . In this case, the quantum eigenstates of the system are characterized by the number of Cooper pair charges in the island n [68]. The qubit transitions are very anharmonic and have a strong dependence on n_g . The Cooper pair box was one of the first superconducting qubits realized experimentally. Quantum-coherent oscillation of a Cooper pair box prepared in a superposition of two states were first seen in 1999 by Nakamura *et al.* [56]. Proving that a quantum system can be put in the coherent superposition of two different quantum states is proving that it can act as a qubit, so that observation was a great achievement.

The main problem of a Cooper pair box turned out to be its strong sensitivity to gate voltage, since it implies a strong sensitivity to noise coming from offset charges.

²If one or more ABS channels has a large transparency, the junction potential has a more complex ϕ -dependence. We will study this in section 1.3.

Increasing the Josephson energy with respect to E_C makes the effect of the supercurrent through the junction more noticeable, so the mixing of number states becomes stronger. This makes the qubit's spectrum less dependent on gate charge, flattening out the charge dispersion. At large E_J/E_C ratios the spectrum becomes similar to the one of a slightly anharmonic oscillator, with the anharmonicity coming from the nonlinear inductance of the Josephson junction. A Cooper pair box operated in the regime $E_J \gg E_C$ is called **transmon** [62].

Inductively shunted qubits

An alternative realization of a qubit with a JJ is one for which the two sides of the junction are connected together forming a loop, possibly including other inductive elements. Now, the phase degree of freedom across the junction, ϕ , is directly related to the magnetic flux through the loop Φ_{ext} , so a junction flux variable $\Phi = \Phi_0 \frac{\phi}{2\pi}$ and a loop phase variable $\varphi_{\text{ext}} = 2\pi \frac{\Phi_{\text{ext}}}{\Phi_0}$ are normally defined, where $\Phi_0 = \frac{h}{2e}$ is the superconducting flux quantum. The external flux constrains the flux drops across the different elements in the loop to add up to Φ_{ext} .

Probably the simplest type of flux qubit is the **rf SQUID**, just a loop with a Josephson junction. The circuit model for this qubit is shown in figure 1.4 b), which includes an inductive term (in purple) denoting the always present magnetic self-inductance of the loop, L . Its Hamiltonian is similar to the one of the Cooper pair box or the transmon, equation 1.20, but now, apart from the Josephson and the charging energies, the **inductive energy** E_L coming from L has to be included

$$E_L = \frac{\Phi_0^2}{4\pi^2 L}. \quad (1.21)$$

Since, as we said, the phase drop at the loop inductance is constrained to be $\phi - \frac{2e}{\hbar} \Phi_{\text{ext}}$, the inductive term of the Hamiltonian becomes

$$H_L = \frac{(\Phi - \Phi_{\text{ext}})^2}{2L} = \frac{1}{2} E_L \left(\phi - \frac{2e}{\hbar} \Phi_{\text{ext}} \right)^2. \quad (1.22)$$

Adding this element to Hamiltonian 1.20 we obtain the Hamiltonian of an rf SQUID

$$H_f = 4E_C n^2 - E_J \cos(\phi) + \frac{1}{2} E_L \left(\phi - \frac{2e}{\hbar} \Phi_{\text{ext}} \right)^2. \quad (1.23)$$

As we said before, the presence of the inductive term breaks the phase periodicity of the system. Since ϕ and n are conjugate variables, we can think of them as a position and a momentum respectively. The E_C term on the Hamiltonian would then correspond to a kinetic energy, C being the effective mass. The two terms depending on ϕ can be thought as a potential. E_L contributes to an overall parabolic shape of this potential, while the E_J term makes it have an oscillatory dependence on ϕ due to its cosine dependence.

Different combinations of the three characteristic energies, E_C , E_J and E_C , result on different properties of the qubit spectrum. The first qubits of this type had E_J/E_L slightly larger than 1. In this case, the last two terms in Hamiltonian 1.23 form a double well potential around $\phi = \pi$ and the qubit states are the lowest states in each of the wells, each of them with a different persistent current configuration.

E_J controls the height of the potential barrier between the wells, and therefore the strength of the mixing of the two qubit states.

Another type of qubit, similar to the one described here, was first developed in Delft in 2000, it was called Josephson persistent current qubit or just **flux qubit** [58], [70]. It included two extra junctions in the loop, so for it the potential was defined in a two-dimensional phase space, corresponding to the phase drops in each of these junctions. Coherent quantum state oscillations were first observed in this qubit in 2003 [71].

Some of these first qubit proposals were, with time, developed further than others. New types of qubits also appeared afterwards. Manucharyan *et al.* proposed in 2009 a type of flux qubit with a very large inductance, the **fluxonium** [10]. A large L brings down its inductive energy E_L , making it less sensitive to flux noise. We will study the fluxonium qubit in detail in section 1.2.3, after introducing the circuit QED architecture, which allows to address this type of qubits with radiofrequency signals.

1.2.2 Circuit QED

Since the appearance of the first superconducting qubits, different ways of addressing the qubit were implemented. A capacitively coupled single electron transistor was used to address the first Cooper pair box [56] and a dc-SQUID was used to control and readout a flux qubit [58], for example. The current leading architecture for addressing (operating and measuring) superconducting qubits is circuit Quantum Electrodynamics (cQED). It was introduced in 2004 by Blais *et al.* [59]. In this approach, the superconducting qubit is coupled to a readout resonator and qubit control is achieved by sending microwaves to the qubit-resonator system and measuring their transmission or reflection. The name cQED comes from the analogy of this system, in which RF photons interact with artificial multilevel systems (or atoms) with Quantum Electrodynamics, the discipline that studies the interaction of photons of light with atoms.

Qubit-resonator interaction

The readout resonator can be modeled as a single-mode LC circuit, with inductance L_r , capacitance C_r and resonant frequency $\nu_r = \omega_r/2\pi$, $\omega_r = 1/\sqrt{L_r C_r}$. The typical way of coupling the qubit to the readout resonator is via a coupling capacitor C_c , which introduces a coupling term into the Hamiltonian of the total system H_{Q+r} .

$$H_{Q+r} = \hbar\omega_r a^\dagger a + gn(a^\dagger + a) + H_Q. \quad (1.24)$$

Here, H_Q is the qubit Hamiltonian and $\hbar\omega_r a^\dagger a$ is the Hamiltonian of the uncoupled resonator, with a being the annihilation operator of a photon in the resonator. The interacting part of the Hamiltonian links the charge degree of freedom at the qubit n to the voltage at the resonator $V = -iV_{ZPF}(a^\dagger + a)$, where the coupling constant g depends on C_c and is a measure of the coupling strength [59], [60]. The circuit model for this system is shown in figure 1.5 a).

Hamiltonian 1.24 can be written in the basis of the qubit eigenstates $|k\rangle$ as

$$H_{Q+r} = \hbar\omega_r a^\dagger a + \hbar \sum_{j,k} g_{jk} |j\rangle \langle k| (a^\dagger + a) + \sum_j \epsilon_j |j\rangle \langle j|. \quad (1.25)$$

With ϵ_k being the eigenenergie of the qubit eigenstate $|j\rangle$ and $g_{jk} = g \langle j|n|k\rangle$.

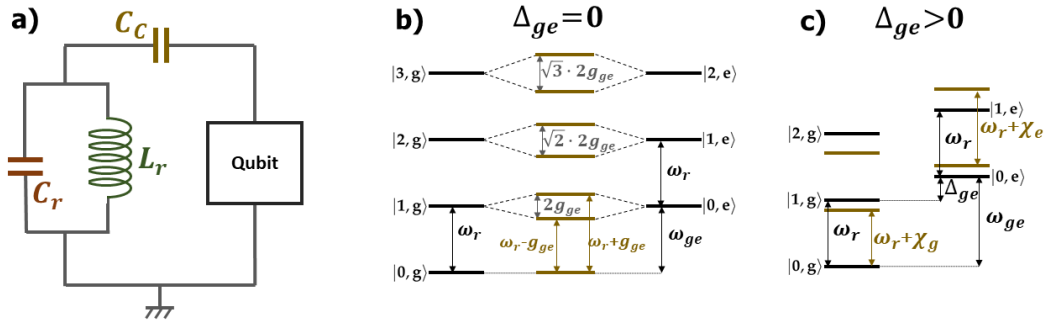


FIGURE 1.5: **Circuit QED.** **a)** Circuit model corresponding to Hamiltonian 1.24, showing a qubit capacitively coupled to a readout resonator. The qubit black box can be any of the circuit models shown in figure 1.4 for different types of qubits. **b)** and **c)** Energy levels of for the resonator-qubit system when they are uncoupled (black) and for non-zero coupling constant g_{ge} (brown). Here we only show two of the qubit states, $|g\rangle$ and $|e\rangle$. Panel **b)** corresponds to zero detuning. Non-zero coupling lifts the degeneracy by an amount proportional to the coupling strength. Panel **c)** corresponds to the dispersive regime $|g_{jk}|\sqrt{n+1} \ll |\Delta_{jk}|\forall j,k$.

The resonator's level separation depends on the qubit state, $|g\rangle$ or $|e\rangle$.

The detuning with respect to the resonator of a qubit transition $|j\rangle \rightarrow |k\rangle$, with frequency $\omega_{jk} = (\epsilon_j - \epsilon_k)/\hbar$, is typically denoted by Δ_{jk} , $\Delta_{jk} = \omega_{jk} - \omega_r$. For **zero detuning** of one of the qubit transitions, the effect of the interaction term in the Hamiltonian is to lift the degeneracy by an amount proportional to g_{jk} , which depends on the number of resonator photons n , $2g_{jk}\sqrt{n+1}$. For **large detuning** of all qubit transitions, $|g_{jk}|\sqrt{n+1} \ll |\Delta_{jk}|\forall j,k$, it is common to treat Hamiltonian 1.25 with perturbation theory. In this case, the interaction results on a pull on the resonator frequency which depends on the state of the qubit and on the number of photons in the resonator. This pull, or dispersive shift, is typically denoted by χ_i for the qubit in state $|i\rangle$ and is a function of the Δ_{jk} 's and g_{jk} 's [62]. In second order perturbation theory we have [72]

$$\chi_i = n\hbar \sum_j \left(\frac{|g_{ij}|^2}{\Delta_{ij}} - \frac{|g_{ji}|^2}{\Delta_{ji}} \right). \quad (1.26)$$

Schematics of the zero-detuning and dispersive regimes discussed above are shown in figures 1.5 b) and c) respectively, for qubit levels g and e only.

For the case of a Cooper pair box or a transmon, the study of the resonator-qubit system can be very simplified due to selection rules that suppress most of the matrix elements $\langle j|n|k\rangle$. For the transmon, only nearest-neighbour matrix elements $\langle j|n|j\pm 1\rangle$ are relevant. When considering only the two lowest energy states of the qubit $|g\rangle$ and $|e\rangle$, the ones relevant for quantum computation, only g_{ge} and g_{ef} have an effect on the relevant dispersive shifts and simple expressions are found for χ_e and χ_g in the dispersive regime [62], [72]

$$\chi_e = n\hbar \frac{|g_{eg}|^2}{\Delta_{eg}} - n\hbar \frac{|g_{fe}|^2}{\Delta_{fe}} \quad \chi_g = -n\hbar \frac{|g_{eg}|^2}{\Delta_{eg}}. \quad (1.27)$$

As we will see in the next section, this simplification is not valid for a fluxonium

qubit, for which many virtual transitions contribute to the dispersive shifts.

Qubit control and dispersive readout

Protocols for qubit control and readout in circuit QED normally rely on the dispersive regime presented above. The pull of the qubit on the resonator frequency can be used to **readout** the qubit state. In experiments, the resonator is capacitively coupled to a feedline with two ports, for which the scattering matrix is measured. When measuring the transmission spectrum through the feedline versus frequency, a dip appears at the resonant frequency of the resonator. If the qubit is in state $|i\rangle$, this dip appears at $\omega + \chi_i$. By measuring the transmitted amplitude or phase close to ω_r one can therefore measure the state of the qubit.

Regarding qubit **control**, it can be achieved by driving the qubit-resonator system with frequency close to ω_{ge} [64], [73]. Depending on the exact pulse frequency, amplitude and duration, qubit rotations around different axes can be realized. For the main superconducting qubits, the cQED architecture permits realizing a universal set of gates that can be combined to obtain any desired gate on single and multiple qubit states.

1.2.3 Fluxonium

As introduced in section 1.1.2, a fluxonium is a type of inductively shunted superconducting qubit [10], [74], [75]. It can be described by the Hamiltonian model presented before for an rf SQUID (equation 1.23), shown again here drifting the phase variable by $\frac{2e}{\hbar}\Phi_{\text{ext}}$ for convenience

$$H_f = 4E_C n^2 - E_J \cos\left(\phi + \frac{2e}{\hbar}\Phi_{\text{ext}}\right) + \frac{1}{2}E_L(\phi)^2. \quad (1.28)$$

A fluxonium is typically operated in a regime $E_L \ll E_C < E_J$. Typical parameters are $E_L/h \sim 0.5$ GHz, $E_C/h \sim 2.5$ GHz and $E_J/h \sim 10$ GHz. Its circuit model is shown in figure 1.4 b).

Fluxonium spectrum: intra-well plasmons and inter-well fluxons

The spectrum of fluxonium is strikingly rich. It is shown in figure 1.6 as a function of Φ_{ext} , for different values of E_J and fixed E_C and E_L values. State and transition energies here and throughout this work are sometimes shown in units of frequency, omitting the conversion factor $\hbar = 1.05 \times 10^{-34}$ m²kg/s.

Column i) shows the potential vs. ϕ for $\Phi_{\text{ext}} = 0$. E_J contributes to the ϕ periodic part, while E_L changes the magnitude of the overall parabolic shape of the potential. The energy levels shown in the second column depend on the potential shape and on the value of C , which is the particle mass in the equivalent mechanical system of a particle with velocity $\dot{\phi}$ moving on this potential. Transition energies, which are the quantity measured in experiments, are shown in column iii). The transitions shown here are only the ones from the ground state to higher energy states, they are the available transitions for a system at zero temperature, for which only the lowest energy state is populated.

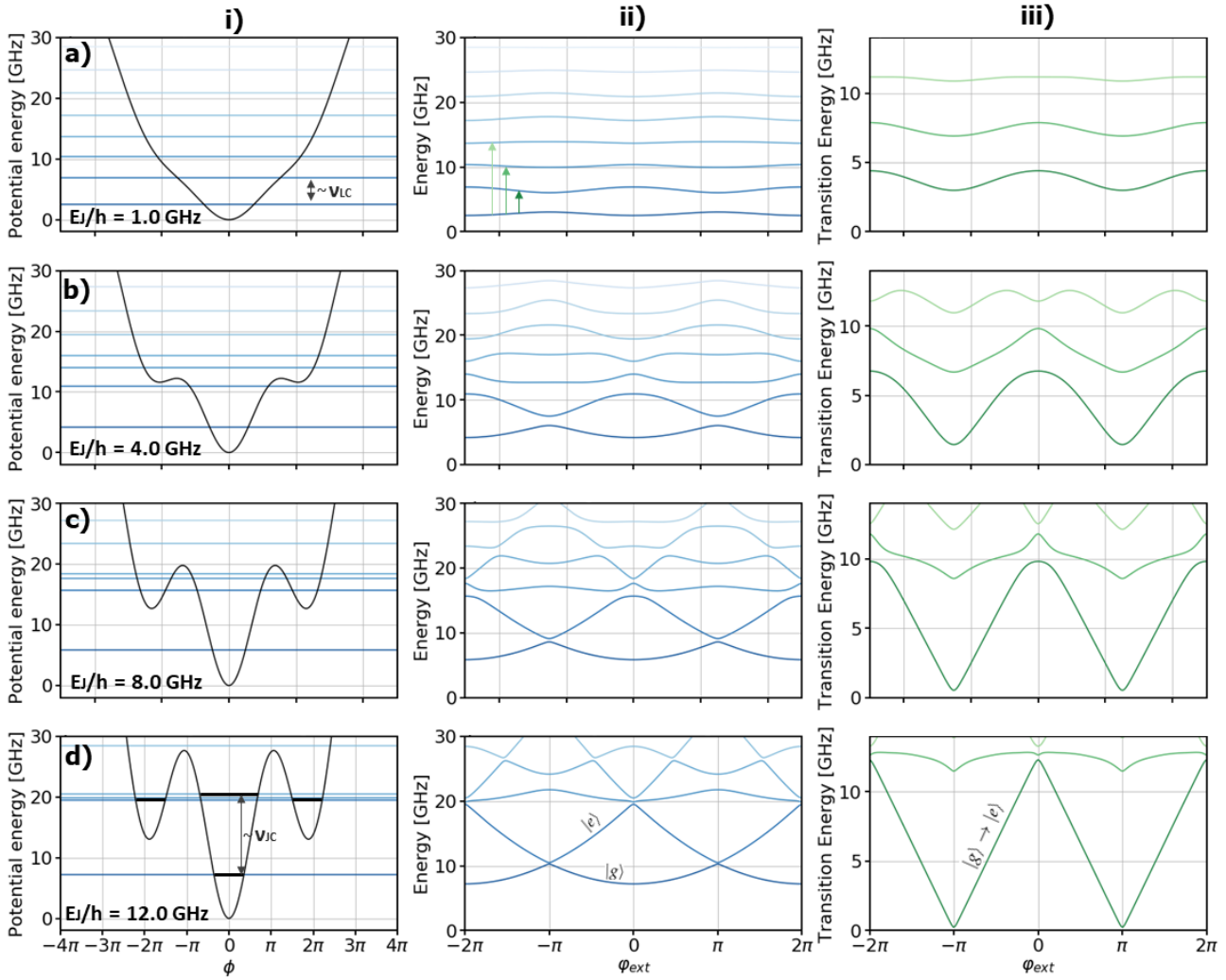


FIGURE 1.6: **Fluxonium potential, spectrum and transition energies for increasing E_J .** Column i) shows the fluxonium potential in Hamiltonian 1.28, at zero external flux and for various values of E_J . Energy levels are superimposed as horizontal blue lines. Rows a), b), c) and d) correspond to $E_J/h = 1, 4, 8$ and 12 GHz respectively. Column ii) shows the lowest eigenenergies of Hamiltonian 1.28. Column iii) shows the lowest energy transitions from the ground state to the lowest excited states, indicated with color-matching arrows in panel a) ii). For all panels $E_L/h = 0.7$ GHz and $E_C/h = 2.4$ GHz.

For **low E_J values** the spectrum is very weakly anharmonic. In this case the states are basically vibrational modes determined by $E_L/h = 0.7$ GHz and $E_C/h = 2.4$ GHz, with some small flux modulation given by E_J . The spacing between eigenenergies in this case is close to the plasma frequency $\nu_{LC} = \omega_{LC}/2\pi = \sqrt{8E_C E_L}/h$, where $\omega_{LC} = 1/\sqrt{LC}$. This plasma frequency is indicated in figure 1.6 a) i). For this specific set of parameters its value is $\nu_{LC} = 3.7$ GHz.

For **large E_J values** the spectrum has a strong dependence on external flux and becomes strongly anharmonic (see figure 1.6 d)). States associated with the lowest energy transitions are no longer vibrational modes of the LC oscillator. The low energy states are in this case localized at one of the potential wells formed due to the strong periodic E_J modulation of the potential and they are typically called fluxons. This localization is highlighted in figure 1.6 d) i). Since these wells are spaced by integer multiples of Φ_0 , a fluxon can be viewed as an integer number of flux quanta trapped in the loop [10]. Comparing rows c) and d) we observe that, as E_J increases

and the wells become deeper (their depth is of the order of E_J/h), tunneling coupling between different fluxon states decreases. This can be seen in the reduction of the splitting between low-energy fluxon states at $\Phi_{\text{ext}} = \pm\Phi_0/2$ in column ii). Transitions between fluxons localized at different wells, **fluxon transitions**, have a strong Φ_{ext} -dependence (see column iii) in figure 1.6). However, transitions between different states localized in the same well have a small Φ_{ext} -dependence, they are called **plasmon transitions** and their frequency can be closely approximated by the junction plasma frequency ν_{JC} , determined by E_J and E_C . This plasma frequency $\nu_{JC} = \sqrt{8E_C E_J}/h$ is shown in figure 1.6 d) i).

To better understand the origin of the strong Φ_{ext} -dependence of the low energy states in the fluxonium regime, it is useful to look at figure 1.7. It shows the evolution of the potential with external flux. For low E_J (figure 1.7 a)), the phase modulation over the parabolic potential is small. Since the effect of Φ_{ext} is only reflected as a shift of this modulation, the potential does not change much for different values of the external flux. For higher E_J the wells configuration depends strongly on Φ_{ext} . The lowest energy states are localized at these wells, so their energy is also affected by Φ_{ext} .

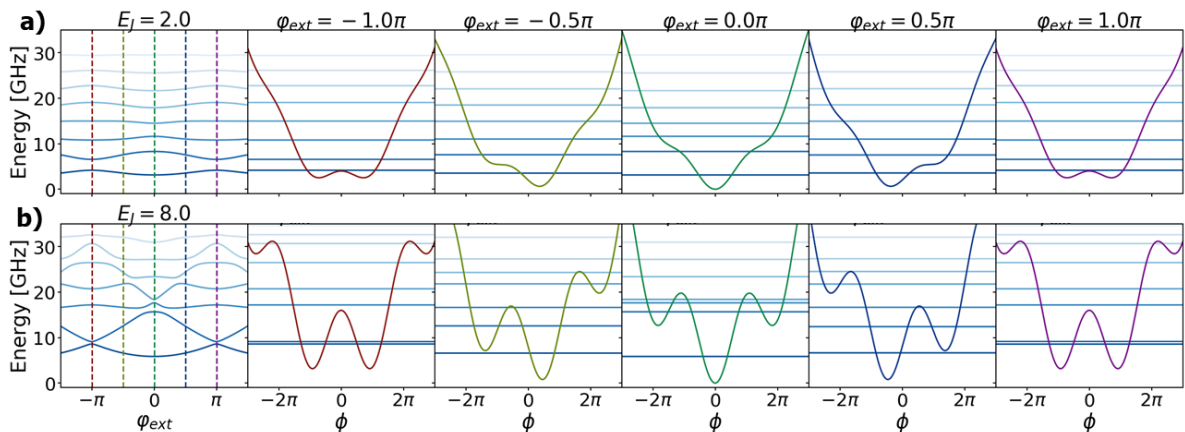


FIGURE 1.7: **Fluxonium potential for two E_J values and different Φ_{ext} values.** The first column shows the fluxonium low energy spectrum for two different E_J values. The rest of the panels show the fluxonium potential in Hamiltonian 1.28 at different values of the external flux, indicated with vertical color lines on the spectra. Horizontal blue lines over the potential plots indicate the system eigenenergies at the corresponding Φ_{ext} . Row **a)** and row **b)** correspond to $E_J/h = 2$ GHz and $E_J/h = 8$ GHz respectively. For all panels $E_L/h = 0.7$ GHz and $E_C/h = 2.4$ GHz, as in figure 1.6.

The parameter regime typically referred as **fluxonium regime** is the one for which the first transition $|g\rangle \rightarrow |e\rangle$ is of fluxon type, between fluxons localized at different wells, and for which the lowest energy well hosts at least two states, allowing for plasmon transitions [75]. The spectrum shown in figure 1.6 row d) is a good example of this regime. In this case, the qubit states $|g\rangle$ and $|e\rangle$ are fluxon states and the fluxon-like transition $|g\rangle \rightarrow |e\rangle$ can be flux-tuned over the entire frequency range typically accessible in experiments. At low external applied flux the qubit $|g\rangle$ state can be thought as a persistent current state in the fluxonium loop, while the $|e\rangle$ state corresponds to a superposition of persistent currents in opposite directions. For $\Phi_{\text{ext}} = \pm\Phi_0/2$, however, the two lowest energy states are the even and odd superpositions of persistent currents flowing in opposite directions.

Sources of decoherence

The relaxation and dephasing times (T_1 and T_2) depend on the susceptibility of the qubit to different loss mechanisms and on the noise of the system's parameters.

Susceptibility to different **loss mechanisms** depends, in different ways, on the point in external flux at which the qubit is operated [76]. It originates from the coupling of ϕ to a bath that can dissipate energy at the frequency of the qubit transition. Such a bath can be modeled as a frequency dependent admittance and the relaxation rate for transition $\langle j | \rightarrow | k \rangle$ can be estimated with Fermi's golden rule [75]–[77]

$$\Gamma_{ij} = \frac{1}{(2e)^2} |\langle j | \phi | k \rangle|^2 S_{I_Y}(\omega_{jk}) \quad (1.29)$$

Where S_{I_Y} is the spectral density of the current noise in the admittance Y modelling the loss bath.

The total qubit relaxation rate is the sum of Γ_{eg} corresponding to different loss mechanisms and it determines T_1 , its inverse. One of these mechanisms is the **Purcell effect**, which comes from the coupling of fluxonium to the 50Ω feedline via the resonator. Relaxation due to Purcell effect is only relevant when the qubit transition is close to the resonator frequency [76].

Other contributions are **capacitive loss** and **inductive loss**. The first comes from a real part of the impedance at the the surface of dielectrics in coupling and shunt capacitors and increases linearly with frequency. The second originates from a lossy permeability (with a real part) and is inversely proportional to frequency. Due to their frequency dependence, these two dissipation mechanisms are expected to be more relevant at $\Phi_{\text{ext}} = 0$ and $\Phi_{\text{ext}} = \pm\Phi_0/2$ respectively, the points where ω_{ge} reaches its maximum and minimum values.

A different loss mechanisms, which has been shown to be the leading source of decoherence for fluxonium [77], is **quasiparticle tunneling** across the junction. Equilibrium quasiparticle population decreases exponentially with temperature, but non-thermal quasiparticles are still present at low temperatures due to cosmic rays, radioactive decay of materials in the cryostat, infrared photons coming from the exterior of the cryostat and other (some of them unknown) sources. The dissipation effects due to quasiparticles can however be reduced by operating the fluxonium at certain flux points. Qubit T_1 times have been shown to increase by more than one order of magnitude between $\Phi_{\text{ext}} = 0$ and $\Phi_{\text{ext}} = \pm\Phi_0/2$ [77]. At $\Phi_{\text{ext}} = \pm\Phi_0/2$ fluxonium becomes insensitive to loss due to tunneling of quasiparticles across the junction. This is due to destructive interference of hole-like and electron-like tunneling channels at that flux point.

From expression 1.29 we see that by reducing the matrix element $|\langle e | \phi | g \rangle|$ of the qubit transition one can increase T_1 . For transmon and other qubits this matrix element needs to be high enough because, as we saw in equation 1.27, it determines the magnitude of the dispersive shift. This is the case for fluxonium, for which higher transitions influence the dispersive shift strongly, as we will see in the next section.

Qubit dephasing can also be produced by noise in different system's parameters, as fluctuating offset charges, external flux noise or variations in E_L , E_C or E_J .

Shunting the Josephson junction with a dc connection eliminates the qubit sensitivity to *constant offset charges*, characteristic of island qubits. This is due to the

possibility of a continuous displacement of the Cooper pair condensate can compensate any offset charge. We can see this by applying a gauge transformation $\psi'(\phi) = e^{in_g\phi}\psi(\phi)$ ³ to Hamiltonian 1.28, which makes it equivalent to the same Hamiltonian with an offset charge n_g [66]. This protection eliminates most problems coming from $1/f$ charge noise in other types of qubits. We should note, however, that a large shunting inductance does not protect against high frequency ac charge noise [66].

It would be too easy if we could get rid of charge sensitivity without paying anything in return. Including a flux knob on the system makes it sensitive to **external flux** fluctuations due to the strong dependence of the qubit transition on Φ_{ext} . $\Phi_{\text{ext}} = 0$ and $\Phi_{\text{ext}} = \pm\Phi_0/2$ are however sweet spots where flux variations do not have an effect to first order (see figure 1.6).

Supercurrent fluctuations of the junction (or E_J **fluctuations**) can also change the qubit frequency and lead to dephasing [75]. For regular fluxonium the value of the supercurrent is not expected to vary, due to the fixed geometry of the junction. As we will see in section 1.3, this will not be the case for the devices studied in this work due to major differences between our junctions and regular SIS junctions. Sensitivity to E_J fluctuations can be reduced by operating the fluxonium qubit at a flux sweet spot for E_J somewhere between $\Phi_{\text{ext}} = 0$ and $\Phi_{\text{ext}} = \Phi_0/2$, which must exist due to the opposite effect of changing E_J at $\Phi_{\text{ext}} = 0$ and $\Phi_{\text{ext}} = \Phi_0/2$.

Other circuit parameters, as E_C and E_L could show fluctuations in our device due to vortices appearing in the corresponding circuit elements at non-zero magnetic field. Measures taken to reduce this effect will be discussed in chapter 2.

Matrix elements

As we saw in section 1.2.2, the matrix elements of qubit transitions have a strong impact on the dispersive shift of the resonator. We have just seen that they also influence the coupling to different sources of decoherence. In this section we take a look at the magnitude and flux dependence of number and phase matrix elements for the lowest energy transitions of fluxonium. Figure 1.8 shows matrix elements for the same E_J values for the spectra in figure 1.6.

As we see, $\langle g|n|f\rangle$ and $\langle g|\phi|f\rangle$ are zero at $\Phi_{\text{ext}} = 0$ and $\Phi_{\text{ext}} = \pm\Phi_0/2$. This occurs because at Φ_{ext} multiple of $\Phi_0/2$ the state wavefunctions have a well defined ϕ -parity due to the symmetry of the potential. Figure 1.9 shows the amplitude of the first three energy levels wave functions as a function of both flux and charge. Ground $\psi_g(\phi)$ and second excited $\psi_f(\phi)$ states are symmetric with respect to coordinate inversion at these flux points, explaining the suppression of the matrix elements

$$\langle g|\phi|f\rangle = \int_{-\infty}^{\infty} d\phi\psi_g(\phi)\psi_f(\phi)\phi \quad (1.30)$$

and $|\langle g|n|f\rangle| \propto |\langle g|\phi|f\rangle|$ [75]. We expect to observe this suppression of the matrix elements as a forbidden $|g\rangle \rightarrow |f\rangle$ transition at zero and half flux in the spectra.

We can also observe that the matrix element $\langle g|\phi|e\rangle$ is strongly enhanced close to half flux ($\Phi_{\text{ext}} = \pm\Phi_0/2$). This is due to the strong hybridization of the two fluxon

³In is not possible to do the same for an island qubit, like the transmon. Due to the 2π phase periodicity its wavefunction this gauge transformation can only be carried out for integer values of n_g in this case (which proves the transmon insensitivity to *integer* offset charges).

states when the two lowest energy fluxon wells have equal depths.

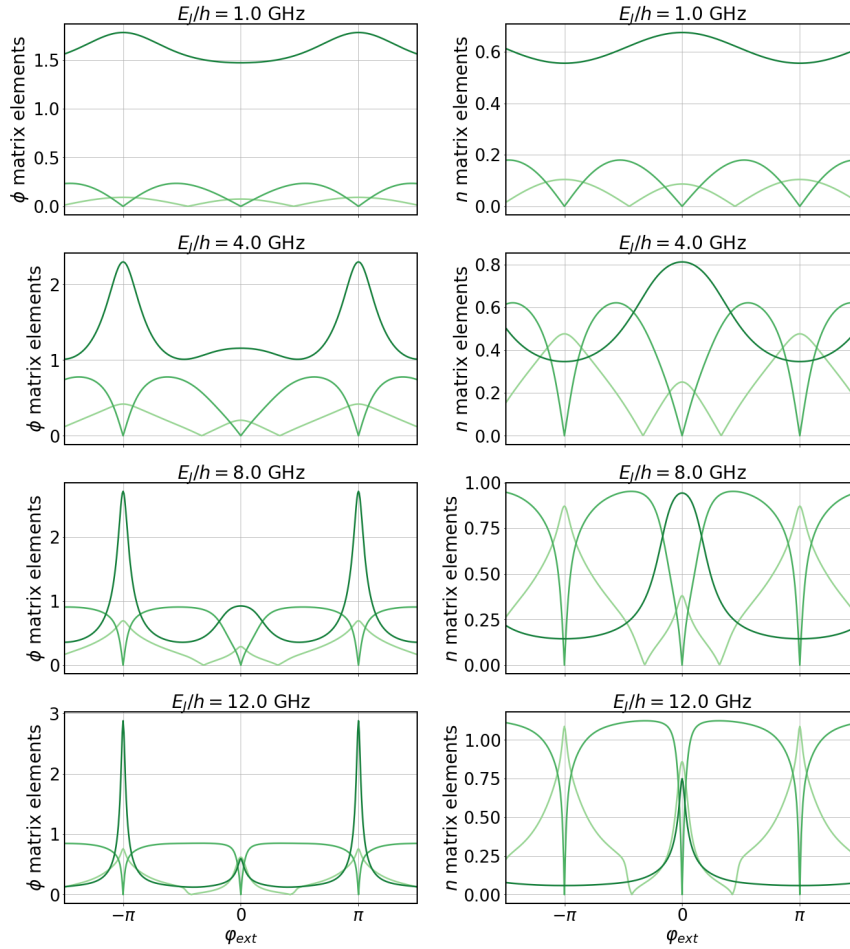


FIGURE 1.8: n and ϕ matrix elements for fluxonium transitions as a function of external flux. Matrix elements shown correspond to the three lowest transitions starting from the ground state shown in figure 1.6 iii). Higher color intensity denotes lower energy transitions. For all panels $E_L/h = 0.7$ GHz and $E_C/h = 2.4$ GHz.

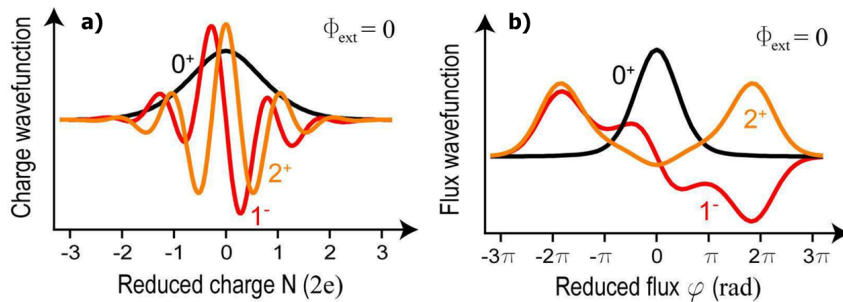


FIGURE 1.9: **Amplitude of fluxonium wavefunctions for the three lowest energy states at zero external flux.** **a)** As a function for reduced charge n . **b)** As a function of phase. $|g\rangle = |0\rangle$, $|e\rangle = |1\rangle$ and $|f\rangle = |2\rangle$. Symbols + and - indicate even and odd parity of the wavefunction, respectively. Circuit parameters are $E_L/h = 0.5$ GHz and $E_C/h = 2.5$ GHz and $E_C/h = 9.0$ GHz, similar to the ones for figure 1.6 d). Figure adapted from [10].

Circuit QED with fluxonium

In this work we will use a shared inductance to couple the fluxonium to the readout resonator. Capacitive coupling (see figure 1.10 a)) has been shown to lead to capacitive loss at the surface of the coupling capacitor dielectric and to increase relaxation rates [76]. We expect therefore to get rid of this loss mechanism by switching to inductive coupling. As shown in figure 1.10 b), a piece of inductance of the fluxonium loop is shared with the inductive part of the resonator. In chapter 2 we will see how this is implemented in experiments.

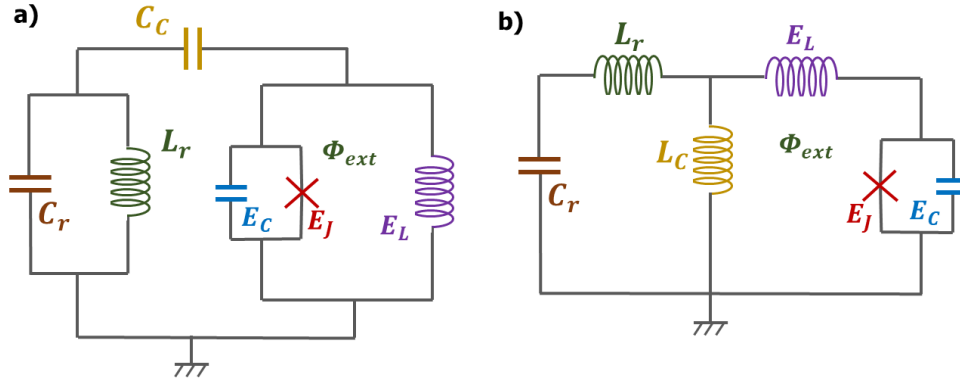


FIGURE 1.10: **Circuit model for a fluxonium circuit coupled to a single mode resonator.** Coupling circuit elements are shown in yellow. **a)** Capacitive coupling to the n degree of freedom via a coupling capacitor C_C . **b)** Inductive coupling to the ϕ degree of freedom via a shared inductance L_C .

Inductive coupling leads to similar effects as the ones discussed in section 1.2.2. Now, the matrix elements relevant for the dispersive shifts are the phase matrix elements (see left column of figure 1.8). Contrary to the case of a transmon qubit, for fluxonium there are no selection rules that suppress the dependence of the dispersive shift χ on transitions to high energy levels. Fluxonium dispersive shifts have been studied up to fourth order perturbation theory by Zhu *et al.* [72] and have been shown to have contributions from matrix elements for transitions in which the state of interest is not even involved.

Of interest for calculating the dispersive shifts at the $|g\rangle$ and $|e\rangle$ qubit states is the $|g\rangle \rightarrow |f\rangle$ plasmon transition. As we see in figure 1.8 the matrix element for the fluxon $|g\rangle \rightarrow |e\rangle$ transition is lower than $\langle g|\phi|f\rangle$, away from half-flux. For not very large Δ_{gf} 's, the latter transition contributes dominantly to the dispersive shift. If the qubit is operated having the readout very detuned from the fluxon transition, but close to the intra-well plasmon transition, which remains at a small frequency window for all flux values, one can avoid relaxation by Purcell effect without suffering from a low dispersive shift.

Figure 1.11 shows the χ_g dispersive shift on the resonator, for two different readout frequencies and for the four different E_j values discussed in previous figures. Column i) corresponds to the readout close to the first transition and detuned for the second. Column ii) shows the opposite case. As we mentioned, for the fluxonium regime (row d)) the reduced matrix element for the $|g\rangle \rightarrow |e\rangle$ fluxon transition results in a suppressed χ_g when the resonator is detuned from other transitions (see fig 1.11 d i)). Far from the fluxonium regime the $|g\rangle \rightarrow |e\rangle$ is not suppressed, due to the absence of deep fluxon wells. As a consequence, coupling of the qubit transition to the readout is much stronger (see fig 1.11 a i)).

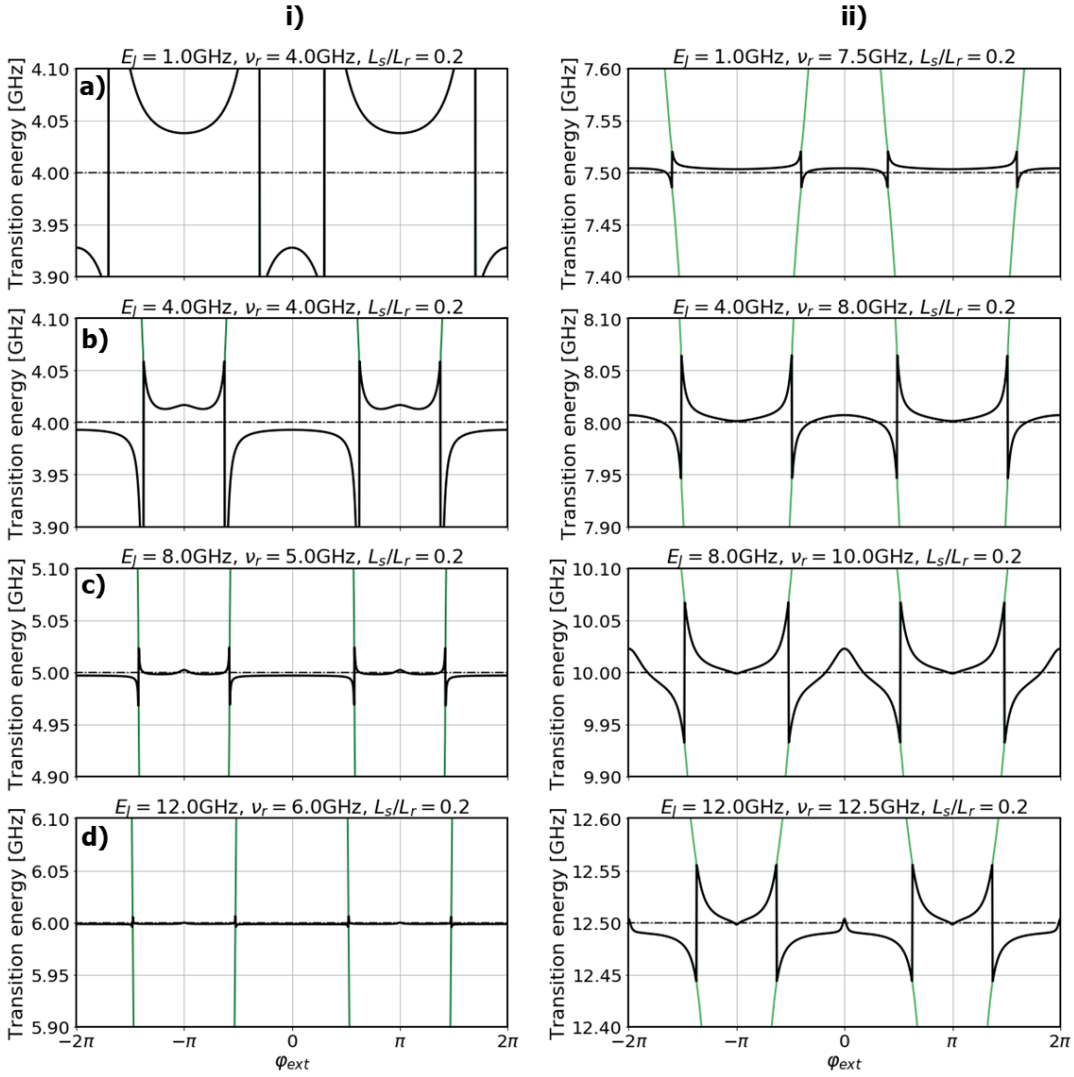


FIGURE 1.11: **Numerically computed dispersive shifts χ_g for an inductively coupled fluxonium-resonator system.** The choice of E_L , E_C and (row-dependent) E_J parameters is the same as in figures 1.6 and 1.8. Each column corresponds to a different value of the readout frequency. Readout for **column i)** is chosen to be detuned from the $|g\rangle \rightarrow |f\rangle$ transition and close to the $|g\rangle \rightarrow |e\rangle$ transition. For **column ii)** readout is close to the $|g\rangle \rightarrow |f\rangle$ transition. Green lines denote qubit transitions. Continuous (dashed) black line denotes readout transition for the coupled (uncoupled) system. Diagonalization of the inductively coupled Hamiltonian is carried out following the method in reference [78].

More interesting may be to take a look at the difference in dispersive shifts for fluxonium in state $|e\rangle$ and $|g\rangle$ respectively, since this determines, together with the matrix element $\langle g|\phi|e\rangle$, the visibility of the $|g\rangle \rightarrow |e\rangle$ transition in two-tone spectroscopy measurements. A large $|\chi_e - \chi_g|$ facilitates characterizing the fluxonium spectrum and also reading out of the qubit state. Figure 1.12 shows $|\chi_e - \chi_g|$, averaged over Φ_{ext} , for different E_J and readout frequency ν_r values. Panel a) corresponds to ν_r detuned from the second transition, as in column i) in figure 1.11. $|\chi_e - \chi_g|$ in this case is much larger for small E_J due to the absence of fluxon wells. As E_J goes up, $|\chi_e - \chi_g|$ decreases, what reduces the visibility of the $|g\rangle \rightarrow |e\rangle$ transition at low readout frequencies. In panel b) we see that, for ν_r close to ω_{gf} , $|\chi_e - \chi_g|$

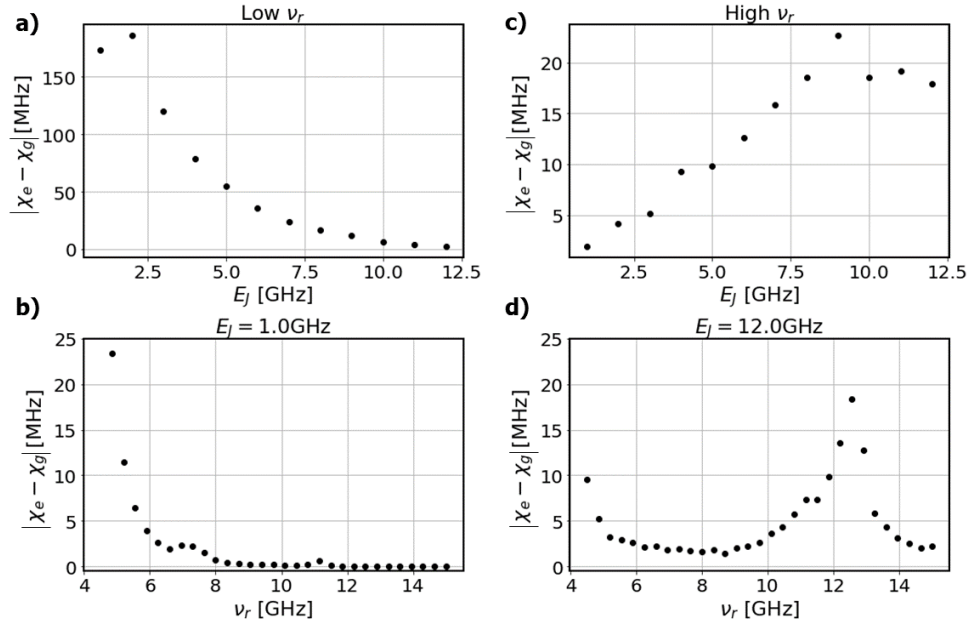


FIGURE 1.12: **Numerically computed difference in dispersive shifts χ_e and χ_g for fluxonium.** **a)** and **b)** show the E_J dependence of average $|\chi_e - \chi_g|$ for readout frequency far and close to ω_{gf} respectively. **c)** and **d)** show the ν_r dependence of average $|\chi_e - \chi_g|$ for small and large E_J values. Diagonalization of the inductively coupled Hamiltonian is carried out following the method in reference [78].

is larger in average. Panels c) and d) show the evolution of average $|\chi_e - \chi_g|$ in frequency, for two values of E_J . At low readout frequencies the dispersive shift is large in both cases. For low E_J this is due to the combination of a large $|g\rangle \rightarrow |e\rangle$ matrix element with a low detuning Δ_{ge} . For high E_J the average dispersive shift increases at low frequencies due to the strong contribution of $\langle g|\phi|e\rangle$ at half flux, but it is low at other flux points. When ν_r gets close to the plasmon transition (at around 12 GHz in this case), there is a spike in $|\chi_e - \chi_g|$ due to the contribution of $\langle g|\phi|f\rangle$.

When coupling fluxonium to the readout resonator, apart from the effect of the qubit on the resonator frequency, we should also take into account shifts of the qubit transitions due to the presence of the resonator, specially when fitting experimental data. This effect is shown in figure 1.13, obtained following the coupled Hamiltonian diagonalization procedure of reference [78]. Shifts of the fluxonium transitions with respect to the bare frequencies are stronger for low E_J values. This is due to the stronger influence of the fluxonium inductance L on the energy levels when E_J is low. Seen from the fluxonium part, coupling to the readout effectively changes L , affecting the transition energies. As expected, this effect is more prominent when increasing the coupling strength (see figure 1.13 ii)).

1.3 Nanowire fluxonium

A nanowire fluxonium, the device studied in this work, is a regular fluxonium in which the Josephson junction has been replaced by a semiconducting nanowire with two superconductor proximitized sections leaving a gap in between: the junction. An schematic of the nanowire Josephson junction is shown in figure 1.14 b). If the

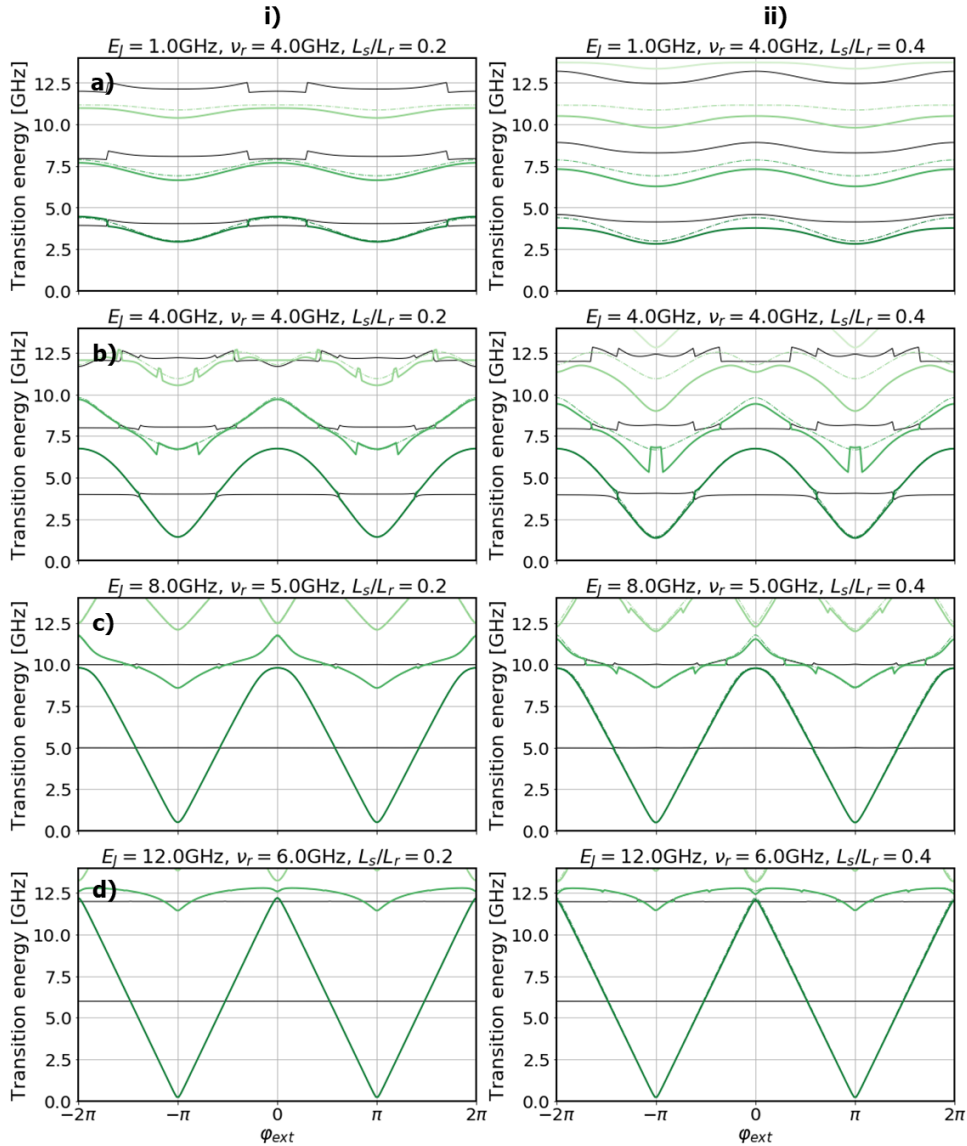


FIGURE 1.13: **Transition frequencies of the inductively coupled resonator-fluxonium system.** Each row corresponds to a different E_J value, analogously to figures 1.6, 1.8 and 1.11. Different columns correspond to different shared inductance L_C over resonator inductance L_r ratios, 0.2 for **i)** and 0.4 for **ii)**. Resonator transitions starting from zero photons are indicated with black lines. Continuous green lines denote transitions of states localized at the fluxonium part. Dashed green lines are included for comparison with the bare resonances of fluxonium with the same circuit parameters. Diagonalization is carried out following the method in reference [78].

two superconducting sections are driven into the topological regime, four Majorana bound states emerge at their ends, forming a qubit (see section 1.1). A circuit model for this device is shown in figure 1.14 a), where the two grey sections represent the topological parts of the wire.

The nanowire fluxonium was first proposed by Pekker *et al.* [30]. They saw that replacing the conventional junction by a junction hosting MZMs alters the spectrum of the qubit due to the 4π -periodic Josephson effect and that this spectrum strongly depends on the parity state of the Majorana qubit. In this section we will see how to use a nanowire fluxonium both to find new signatures of MZMs and to realize coherent state transfer between the topological qubit and the fluxonium.

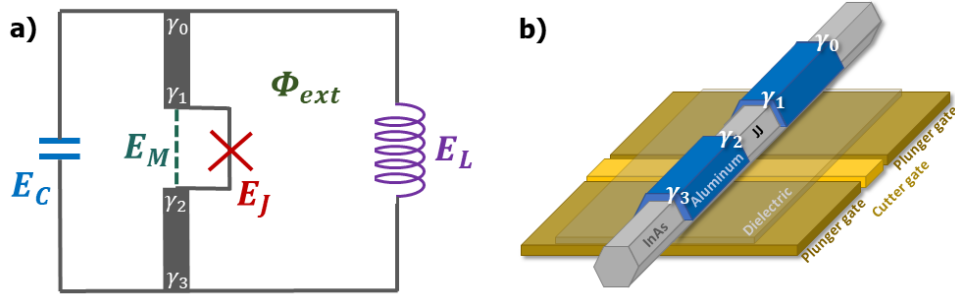


FIGURE 1.14: **Nanowire fluxonium.** **a)** Circuit model for a nanowire fluxonium in the topological regime, corresponding to Hamiltonian 1.38. **b)** Schematic (not to scale) of the nanowire Josephson junction showing in yellow the cutter gate that is used to electrostatically tune the transmission of the Andreev bound states at the junction and in brown the gates that tune the chemical potential of the topological sections.

1.3.1 Nanowire Josephson junction

Without considering for now any topological effect on this device, we already notice a main difference with respect to a fluxonium with an SIS junction. A superconductor-nanowire-superconductor (SNS) Josephson junction does not necessarily have the cosine potential showed in equation 1.18 for an SIS junction. Until now, since we only considered SIS junctions, which are typically the junctions used in regular superconducting qubits, it was safe to assume that the transmission probability of all Andreev bound states (ABSs) was low. In this limit, as we will see, the ϕ dependence of junction potential can be safely approximated by a cosine. In a semiconductor wire junction this is not necessarily the case. A more general expression, if the junction is short (i.e. much shorter than the superconducting coherence length), takes into account the contributions from different transmission channels. Previous work has demonstrated the possibility of using SNS junctions as the nonlinear element in superconducting qubits [79]–[82]. In order to better understand the similitudes and differences between these devices and qubits based on traditional SIS junctions, we will very briefly discuss here the basic physics of ABSs at a Josephson junction.

An Andreev bound state is a fermionic mode localized at the junction that appears as a result of constructive interference of Andreev reflection processes [83]. The energy of a (degenerate) ABS with transmission probability T and at zero field is [84]

$$E_{ABS}(\phi) = -\Delta \sqrt{1 - T \sin^2(\phi/2)}. \quad (1.31)$$

Here, Δ is the induced superconducting gap in the nanowire. Each ABS contributes to tunneling of Cooper pairs across the junction. The Josephson supercurrent generated by the phase dependence of an ABS energy can be directly calculated as $I_{ABS} = \frac{\Phi_0}{2\pi} \frac{\partial E_{ABS}}{\partial \phi}$. A typical SNS junction has several Andreev bound states that contribute to its total current and are normally seen as different transmission channels. The junction potential can be expressed as the sum of the energies of all ABS contributing to the junction conductance.

$$V_{SNS}(\phi) = -\Delta \sum_{i=1}^N \sqrt{1 - T_i \sin^2(\phi/2)}. \quad (1.32)$$

In the limit of $T_i \ll 1$ for all i we can Taylor expand the square root and approximate $V_{SNS}(\phi)$ as

$$V_{SNS}(\phi) \simeq -N\Delta + \frac{\Delta \sum_{i=1}^N T_i}{2} \sin^2(\phi/2) = -\frac{\Delta \sum_{i=1}^N T_i}{4} \cos(\phi) + \text{constant} \quad (1.33)$$

recovering the cosine potential presented before. Comparing this expression with equation 1.18 we obtain $E_J \simeq \Delta \sum_{i=1}^N T_i / 4$.

For a semiconducting junction, transmission probabilities are not always necessarily much smaller than 1. Spectroscopy measurements in ballistic semiconducting nanowires show channels with transmission up to 0.9 [85]. Still, as we will see in the measurements in chapter 3, this will not have a strong impact on the spectra, which at low energies can normally be considerably well fitted assuming a cosine dependence of the Josephson term in the Hamiltonian. What is going to be more relevant for us is the dependence of E_J on the superconducting gap Δ and on the transmission probabilities T_i . This dependence is not important in typical experiments with regular superconducting qubits, because there Δ and the T_i 's are fixed. This will not be the case for us, the Δ and T_i 's dependence of E_J will result on a strong variation of the nanowire fluxonium spectrum with external magnetic field and cutter gate voltage.

Magnetic field dependence of E_J

In order to drive the superconducting sections of the wire into the topological regime one needs to apply a magnetic field. A combination of different effects will lead to a suppression of the induced gap with B . Since E_J is proportional to Δ , we expect to see a reduction of E_J when going up in field.

One of the most direct effects of the magnetic field is a **suppression of the gap in the parent superconductor** which induces Δ in the nanowire [67]. This dependence has the form

$$\Delta(B) = \Delta(B=0) \sqrt{1 - \frac{B^2}{B_C^2}}, \quad (1.34)$$

where B_C is the critical magnetic field. However, this effect is not expected to be the leading one in this system due to the small shell thickness of the proximitized aluminum, which leads to an Al critical field much greater than the bulk one.

As we saw in figure 1.2 f), the combination of **Zeeman effect and spin-orbit interaction** also leads to a reduction of the induced gap. A detailed treatment of the experimentally observed field dependence of the ABS energies, taking these two effects into account, is discussed in reference [85]. The authors carry out spectroscopy measurements of the ABSs and show that Zeeman and spin-orbit have a big impact on the suppression of the ABS energies with field. They observe a strong reduction of the ABS energy at B in the order of hundreds of mT, shown in figure 1.15 b).

Other effects of a parallel B can also be taken into account. As we discussed in section 1.1, the **orbital effect** due to magnetic field threading flux quanta through the nanowire cross section has a strong impact on the induced gap [43], [45]. This

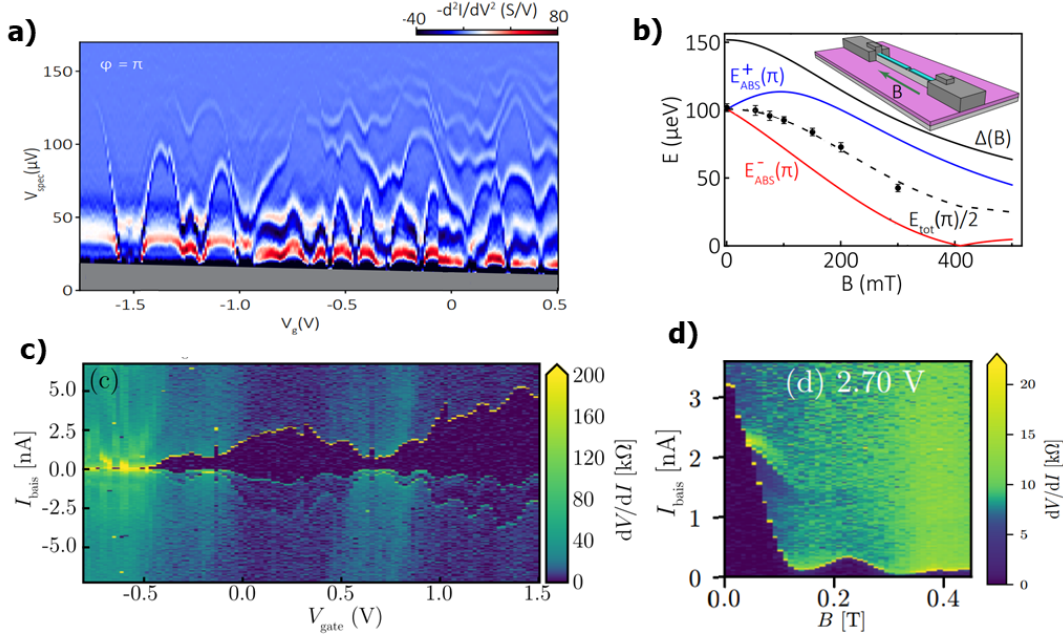


FIGURE 1.15: **Cutter gate and parallel magnetic field dependence of E_J .** Panels **a**) and **b**) show spectroscopy measurements of ABSs in an aluminum proximitized InAs nanowire junction, at $\phi = \pi$. Figures adapted from [85]. Panels **c**) and **d**) show supercurrent measurements of a NbTiN-InSb nanowire-NbTiN junction. The sudden differential resistance change from almost 0 to several k Ω determines the critical current, and can be linearly mapped to the value of E_J . Figures adapted from [86]. Panel **a**) shows how ABS appear sequentially as V_c is increased. This results in the non-monotonical overall increase of the critical current shown in **c**). $B = 0$ for both **a**) and **c**). Panels **b**) and **d**) show, respectively, the reduction of E_{ABS} and I_C with parallel magnetic field B .

effect contributes quadratically to the gap dependence on B

$$\Delta(B) = \Delta(B = 0) \left(1 - \frac{B^2}{B_*^2}\right). \quad (1.35)$$

where $B_* = \Phi_0/A$ and A is the cross sectional area of the nanowire. We can see this effect in the results of numerical simulations in figure 1.3. The magnitude of the topological gap decreases considerably when orbital effect is considered (panel c)) with respect to when it is not (panel b)).

Furthermore, magnetic field can induce **interference between the one-dimensional modes** at the junction. Supercurrent suppression due to this effect was experimentally and numerically studied by Zuo *et al.* [86] carrying out resistivity measurements across the junction. The critical current I_C can be directly mapped to E_J . Since the ABS supercurrent is $I_{ABS} = \frac{\Phi_0}{2\pi} \frac{\partial E_{ABS}}{\partial \phi}$ we have that, for a cosine phase dependence of the Josephson effect, I_C is proportional to E_J , $I_C = \frac{\Phi_0}{2\pi} E_J$. Figure 1.15 d) shows the strong suppression of the critical current, at magnetic fields parallel to the wire of the order of hundreds of mT, observed in Zuo *et al.* experiments. We expect a similar behaviour for E_J in our measurements, which will have a strong impact on the nanowire fluxonium in-field spectroscopy.

Cutter gate dependence of E_J

Since E_J also depends strongly on the transmission probabilities of the channels, being able to change the transparency of the junction would allow to tune E_J without having to change the external field. For this reason we include a cutter gate which can be used to electrostatically tune the electron density at the semiconducting junction. This gate is shown in yellow in figure 1.14 b).

It is difficult to deterministically predict in advance the exact value of E_J corresponding to a given gate potential V_c , due to the different contributions from various channels. The general trend observed in this work agrees, however, with previous observations in similar systems [80], [85], [86]. At low, typically negative, V_c , the junction is fully depleted. As V_c increases, different ABSs enter the superconducting gap one by one, but their energies increase and decrease in an oscillatory way, due to a non-monotonic dependence of the channel transmissions on V_c [85] (see figure 1.15 a) and c)). This translates, for our measurements, on a non-monotonic increase of E_J as the gate potential is increased.

In all the superconducting qubits shown above, E_J of a single junction is fixed by its geometry and material properties, and can not be changed after fabrication. A typical way of including some flexibility in E_J in the case of SIS junctions is replacing the single JJ by a dc SQUID containing two JJs and using the flux threaded through this loop to control the effective E_J value. Using, instead, an SNS junction, as in this case, allows to uncouple the knob for E_J from the control of the external flux through the loop Φ_{ext} . Gate noise could, however, become a new source of decoherence, due to its direct influence in E_J . The non-monotonic dependence of E_J on cutter voltage allows to find sweet spots (local maxima or minima of $E_J(V_c)$) where this decoherence rate is minimized.

ABS state dependence of E_J

At zero field each ABS level is degenerate (Kramers degenerate at the time-reversal invariant ϕ points 0 and π). Depending on its occupation it can be in four different fermionic many-body configurations [87]. Two of these configurations have even parity: the ground state and the doubly excited state with energy $2|E_{ABS}|$ above it. The other two states, singly excited, have odd parity and are spin-degenerate. Their energy is $|E_{ABS}|$ above the ground state. At non-zero field the degeneracy of the odd-parity states is broken, but there are still four possible states for a single ABS, two with odd parity ($|1\rangle$ and $|2\rangle$, with energies E_1 and E_2 respectively) and two with even parity ($|V\rangle$ and $|P\rangle$, with energies 0 and $E_1 + E_2$ respectively) [88].

Depending on the state of an ABS, its contribution to the total E_J is different. If it is in the vacuum state $|V\rangle$, it contributes as shown before, with $E_{J,i} \sim \Delta T_i/4$. However, if it is excited thermally or by a photon to its $|P\rangle$ state, then the contribution to the total Josephson energy changes sign. An Andreev channel can also change parity via quasiparticle poisoning event and be excited to an odd state. In this case, it doesn't contribute to the total E_J because its energy does not depend on phase.

Therefore, both parity conserving excitations and quasiparticle poisoning events can result in an effective change in E_J . If these transitions happen in a time scale small compared to the measurement time, spectral lines corresponding to different

values of E_J could in principle be observed simultaneously in spectroscopic measurements.

The dynamics of ABS many-body configuration in Al/InAs nanowire junctions has been studied in reference [89]. They find characteristic time scales for ABS parity switching and for $|V\rangle \leftrightarrow |P\rangle$ switches of around $160\ \mu\text{s}$ and $3.2\ \mu\text{s}$ respectively, both at $\sim 30\ \text{mK}$. Their study corresponds to a single ABS with high transmission ($T_i \sim 0.98$), so the extracted time scales are specific for that case. However, they can be taken as an order of magnitude estimate of the measurement time in which simultaneous effects from different effective E_J values will be observed in our experiments. The typical measurement time of a nanowire fluxonium spectrum is of the order of minutes or even hours. For cases in which at least one ABS has a big transmission, and therefore contributes strongly to the spectrum, this effect could potentially have a big impact on the experimental observations.

1.3.2 Spectrum of a nanowire fluxonium

The circuit model for a nanowire fluxonium is shown in figure 1.14 a). For now, we neglect the possible interaction between MZMs localized next to the junction (inner Majoranas, γ_1 and γ_2) and away from the junction (outer Majoranas, γ_0 and γ_3). The Hamiltonian for this system will therefore be the one for a regular fluxonium (equation 1.28) with the V_{SNS} potential instead of the cosine E_J term and with an extra term coming from the coupling between inner Majoranas

$$H = 4E_C n^2 - \Delta \sum_{i=1}^N \sqrt{1 - T_i \sin^2(\phi/2)} - E_M i \gamma_1 \gamma_2 \cos(\frac{\phi}{2}) + \frac{1}{2} E_L (\phi - \frac{2e}{\hbar} \Phi_{\text{ext}})^2. \quad (1.36)$$

The new energy scale $E_M = \sqrt{T_M} \Delta$, with T_M the transmission of the topological channel, denotes the magnitude of the coupling between γ_1 and γ_2 , which depends on the amount of overlapping of their wavefunctions.

In what follows we will study the spectrum of a nanowire fluxonium, focusing first on the effect of high transmission channels and afterwards on the Majorana coupling. We will ignore in both cases the auxiliary circuitry for control and readout discussed in previous sections (i. e. we will consider only the uncoupled fluxonium).

Zero field

At zero field both superconducting sections of the wire are in the trivial regime, so $E_M = 0$. The system's Hamiltonian is very similar to the one for a regular fluxonium, studied in section 1.2.3.

$$H = 4E_C n^2 - \Delta \sum_{i=1}^N \sqrt{1 - T_i \sin^2(\phi/2)} + \frac{1}{2} E_L (\phi - \frac{2e}{\hbar} \Phi_{\text{ext}})^2. \quad (1.37)$$

Figure 1.16 shows fluxonium spectra for a single channel with increasing transmission T . We plot, together in each panel, spectra for different Δ values, but with fixed effective $E_J = \Delta T/4$. As we see, the effect of high transmission is more noticeable at higher energies, specially for large E_J . Having a single channel with high

transmission can therefore strongly affect the fluxonium spectrum, and should be taken into account when interpreting the spectroscopy data.

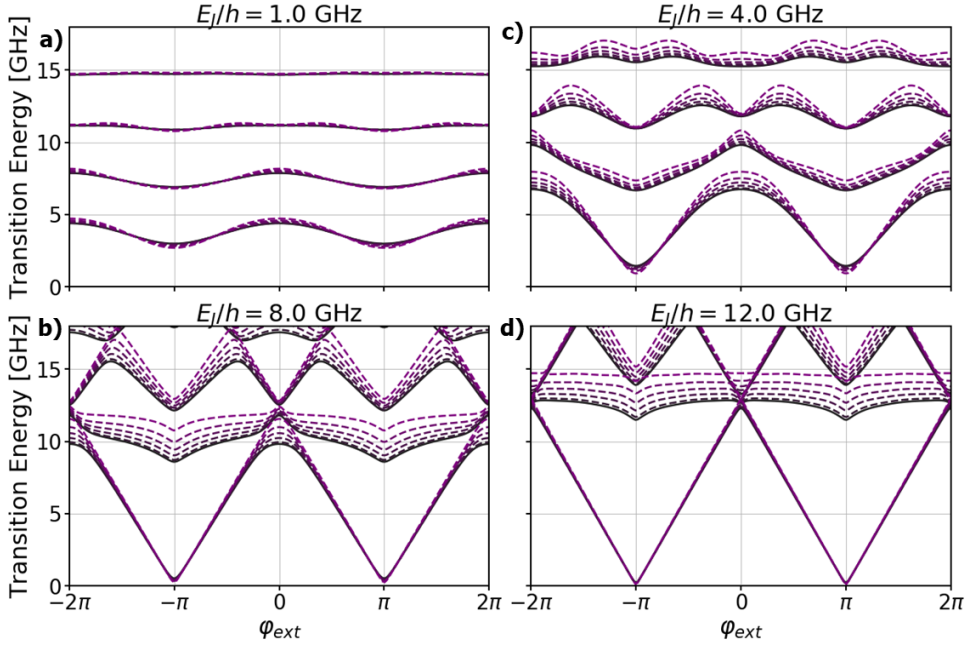


FIGURE 1.16: **Transition energies for fluxonium with a high transmission channel, obtained by diagonalization of Hamiltonian 1.37 with $N=1$.** Different E_J values are indicated on the titles of different panels. Continuous lines denote transitions corresponding to a cosine E_J term and they are equal to the spectra in figure 1.6. Dashed lines correspond to different T values, starting from $T = 0.1$ for the darkest color and increasing in steps of 0.2 until $T = 0.9$ for the brightest color. All transitions shown start from the ground state.

Topological regime

Now, we focus on the effect of the Majorana interaction across the junction, assuming a cosine dependence of the E_J term. We neglect for now the coupling to outer Majoranas γ_0 and γ_3 .

$$H = 4E_C n^2 - E_J \cos(\phi) - E_M i\gamma_1 \gamma_2 \cos\left(\frac{\phi}{2}\right) + \frac{1}{2} E_L \left(\phi - \frac{2e}{\hbar} \Phi_{\text{ext}}\right)^2 \quad (1.38)$$

Figure 1.17 shows the effect of a non-zero E_M on the potential, for different parities of $i\gamma_1 \gamma_2$. The potential is now 4π -periodic in external field, instead of 2π -periodic, as in the trivial case. We can see this comparing figure 1.7 to figure 1.17. In the first case, the potential shape is identical for $\varphi_{\text{ext}} = 0$ and $\varphi_{\text{ext}} = 2\pi$, while a non-zero E_M term changes this periodicity.

Assuming fixed total fermion parity of the four MZMs $-\gamma_0 \gamma_1 \gamma_2 \gamma_3 = \pm 1$, the state of the topological qubit embedded in the fluxonium circuit is determined by the parity $i\gamma_1 \gamma_2 = \pm 1$ (see discussion around equation 1.15). As shown in figure 1.18, the qubit state is encoded in the nanowire fluxonium spectrum, which can be seen as two copies of the trivial fluxonium spectrum, shifted in opposite directions depending on the state of the topological qubit. The separation is more clear for larger E_M values. The horizontal shift is proportional to E_M/E_L , for E_M values lower than $\pi^2 E_L$. At $E_M = \pi^2 E_L$, the minima with opposite parity, which would be at

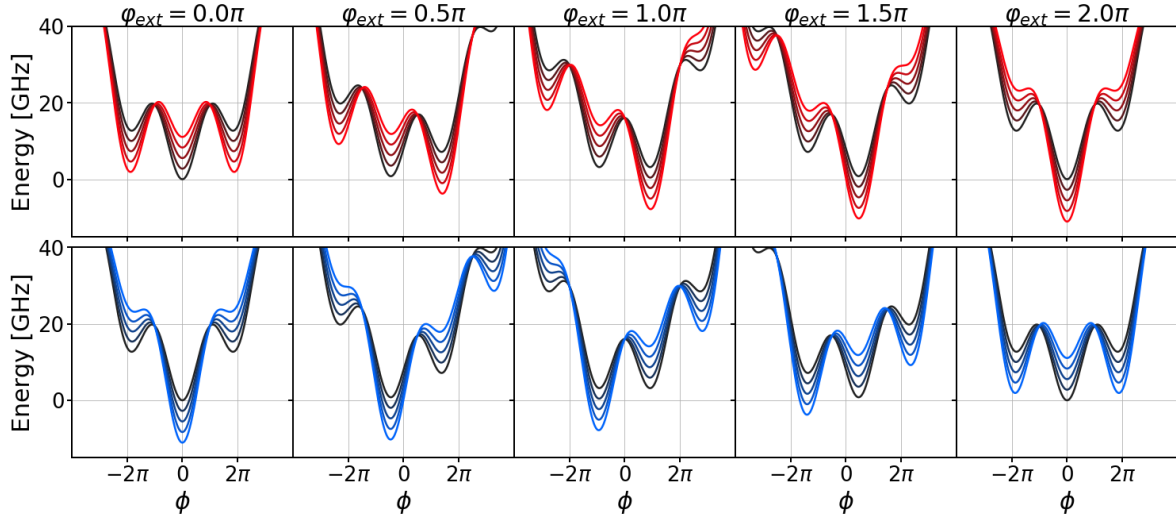


FIGURE 1.17: **Evolution of the nanowire fluxonium potential for increasing E_M .** This evolution is shown for a range of E_M values, starting from $E_M = 0$ (black lines) and until $E_M = 2\pi^2 E_L$ (brightest color lines). Different columns indicate different external field and different rows correspond to different $i\gamma_1\gamma_2$ parity, even for the top (red) row and odd for the bottom (blue) one. Black lines show the trivial fluxonium potential, and are therefore equal for both parities. For all panels $E_J/h = 8\text{GHz}$, $E_L/h = 0.7\text{GHz}$ and $E_C/h = 1.0\text{GHz}$, as in figure 1.6 row c).

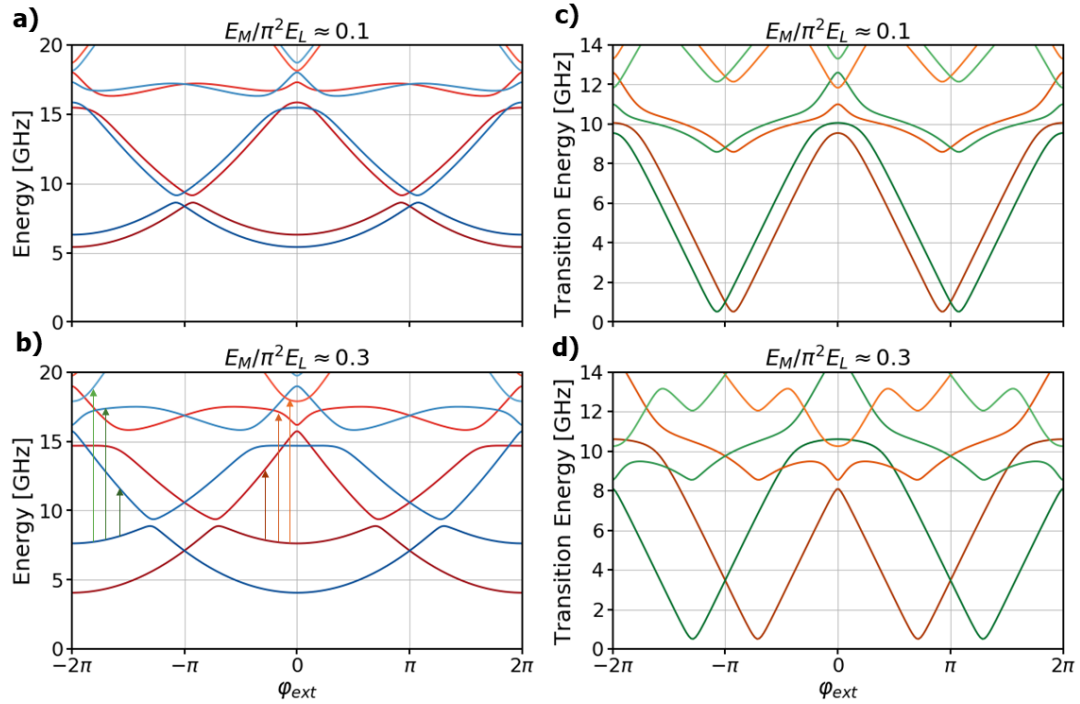


FIGURE 1.18: **Evolution of the nanowire fluxonium spectrum and transition energies for increasing E_M .** Left column shows the lowest eigenenergies of Hamiltonian 1.38, for two different values of E_M . Red and blue colors indicate even and odd parity $i\gamma_1\gamma_2$, respectively. Right column shows the lowest energy parity-conserving transitions from the ground state to the lowest excited states, indicated with color-matching arrows in the panel b). For all panels $E_J/h = 8\text{GHz}$, $E_L/h = 0.7\text{GHz}$ and $E_C/h = 1.0\text{GHz}$, as in figure 1.6 row c).

$\varphi_{\text{ext}} = \pi$ in the trivial case, reach $\varphi_{\text{ext}} = 0$ and $\varphi_{\text{ext}} = 2\pi$. For $E_M > \pi^2 E_L$ the two

minima stay at these same flux positions.

Depending on the state of the topological qubit, different transitions are available (figure 1.18 c) and d)) and the corresponding dispersive shifts change. This allows to carry out fast readout of the qubit state using standard superconducting qubits techniques.

Finite size effects

Due to the finite length of real nanowires and the spatial extension of the Majorana wavefunction, outer and inner Majoranas wavefunctions can also overlap⁴. This can lead to coherent junction parity oscillations, mixing the two parity-dependent sets of lines in the spectrum. This effect can be modeled including two extra terms in the Hamiltonian [30]

$$H = 4E_C n^2 - E_J \cos(\phi) - E_M i\gamma_1 \gamma_2 \cos\left(\frac{\phi}{2}\right) + E_M^{01} i\gamma_0 \gamma_1 + E_M^{23} i\gamma_2 \gamma_3 + \frac{1}{2} E_L \left(\phi - \frac{2e}{\hbar} \Phi_{\text{ext}}\right)^2 \quad (1.39)$$

Here, E_M^{01} and E_M^{23} are the coupling strengths between inner and outer Majoranas at both sides of the junction, and are not necessarily equal. These $i\gamma_0 \gamma_1$ and $i\gamma_2 \gamma_3$ couplings correspond to x and y interactions in the topological qubit (see equation 1.15).

Figure 1.19 shows the eigenenergies and transition energies for Hamiltonian 1.39 for two different values of $E_M^{01} = E_M^{23}$. As we mentioned, including these coupling terms results in anticrossings between energy levels with different parities, with a gap size proportional to the strength of the finite-size couplings. This gives rise to extra transitions, involving states with different $i\gamma_1 \gamma_2$ parity, which were forbidden before.

1.3.3 cQED with a nanowire fluxonium: implementation of quantum gates

Labels to the quantum states in figure 1.19 are assigned by comparison to the spectrum without E_M^{01} and E_M^{23} couplings. If these couplings are weak, which can be achieved using long wires, these states are strongly hybridized at the anticrossings, but almost separable away from them. Therefore, staying at flux points far from anticrossings, the quantum state of fluxonium and topological qubit can be addressed reliably and independently.

In order to realize **single qubit gates** on the topological qubit, one option is to drive transitions on the spectrum that change only the topological qubit state. To realize a rotation around x , for example, one can excite the $|-\rangle \leftrightarrow |+\rangle$ transition. However, as we see in figure 1.19, its frequency depends in principle on the state of the fluxonium qubit (i.e. $\omega_{|g,-\rangle \leftrightarrow |g,+\rangle}$ and $\omega_{|e,-\rangle \leftrightarrow |e,+\rangle}$ are different). One way of solving this issue is increasing the value of E_J , which makes $\omega_{|g,-\rangle \leftrightarrow |g,+\rangle}$ and $\omega_{|e,-\rangle \leftrightarrow |e,+\rangle}$ be degenerate over a range of Φ_{ext} values. This is shown in figure 1.20, which shows the same spectra but for $E_J/h = 14$ GHz instead of 8 GHz. By using standard cQED techniques and driving the qubit with a pulse with frequency close but slightly detuned from the $|-\rangle \leftrightarrow |+\rangle$ transition frequency, it is also possible to realize other single qubit rotations, like the Hadamard gate [59]. Furthermore, one can achieve coherent quantum amplitude exchange between the $|-\rangle$ and $|+\rangle$ qubit states by flux

⁴We do not consider here the coupling between non-neighbour Majoranas.

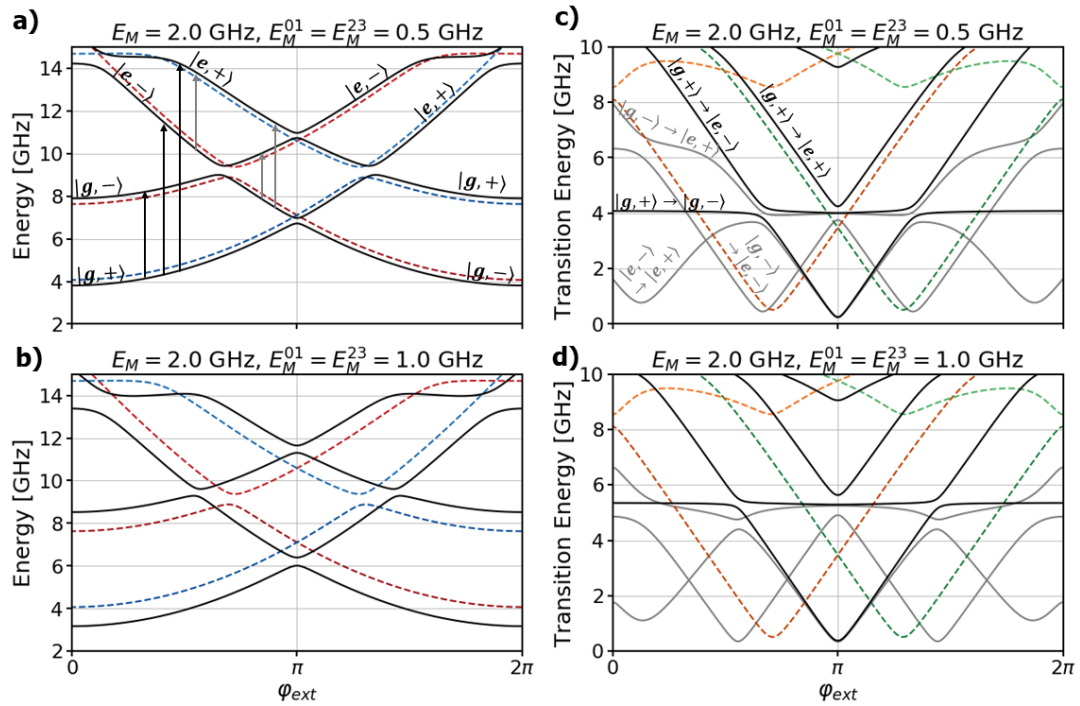


FIGURE 1.19: **Nanowire fluxonium spectrum and transition energies including inner to outer Majorana coupling terms** Different rows correspond to difference value of $E_M^{01} = E_M^{23}$, indicated in the titles. Left column shows the lowest eigenenergies of Hamiltonian 1.39 in black, superimposed to the corresponding levels in the absence of these couplings (red or blue dashed lines depending on the $i\gamma_1\gamma_2$ parity). Right column shows transitions from the ground state (in black) and from the first excited state (in grey), again, superimposed to the parity-conserving transitions in the absence of inner-outer couplings. In **a)** the energy levels are labeled by comparison with the decoupled spectrum. For all panels $E_J/h = 8$ GHz, $E_L/h = 0.7$ GHz, $E_C/h = 1.0$ GHz and $E_M/h = 2.0$ GHz.

pulsing into the avoiding crossing at $\Phi_{\text{ext}} = \Phi_0/2$, where these two states mix significantly. At this point coherent oscillations between the two states occur naturally, by characterizing the coupling and pulsing for the correct amount of time, one can also achieve a controlled rotation around the x axis.

By driving other transitions in this spectrum it is also possible to realize gates involving both the topological qubit and the fluxonium qubit. Being able to realize a **SWAP gate**, exchanging their states, would permit carrying out any gate available for fluxonium on the topological qubit. The simplest way of implementing a SWAP gate is by directly applying a π -pulse at the frequency of transitions $|g, -\rangle \leftrightarrow |e, +\rangle$ and $|g, +\rangle \leftrightarrow |e, -\rangle$ when they are degenerate. As before, this degeneracy appears only at a range of Φ_{ext} values, which becomes larger as E_J is increased (see figures 1.19 and 1.20).

It could be that the matrix element of this direct transition is too low, making it difficult to realize a SWAP gate by driving it. An alternative is to use a combination of cNOT gates. If cNOT_F and cNOT_M are, respectively, the cNOT gates having the fluxonium qubit and the Majorana qubit as a control, the SWAP gate can be implemented combining them: $\text{SWAP} = \text{cNOT}_F \text{cNOT}_M \text{cNOT}_F$. The **cNOT_F gate** can be implemented applying a π -pulse at frequency $\omega_{|g,+ \rangle \leftrightarrow |e,+ \rangle}$. The **cNOT_M gate** can be implemented by applying a π -pulse at frequency $\omega_{|e,- \rangle \leftrightarrow |e,+ \rangle}$ at a flux point where it is not degenerate with $\omega_{|g,+ \rangle \leftrightarrow |g,- \rangle}$.

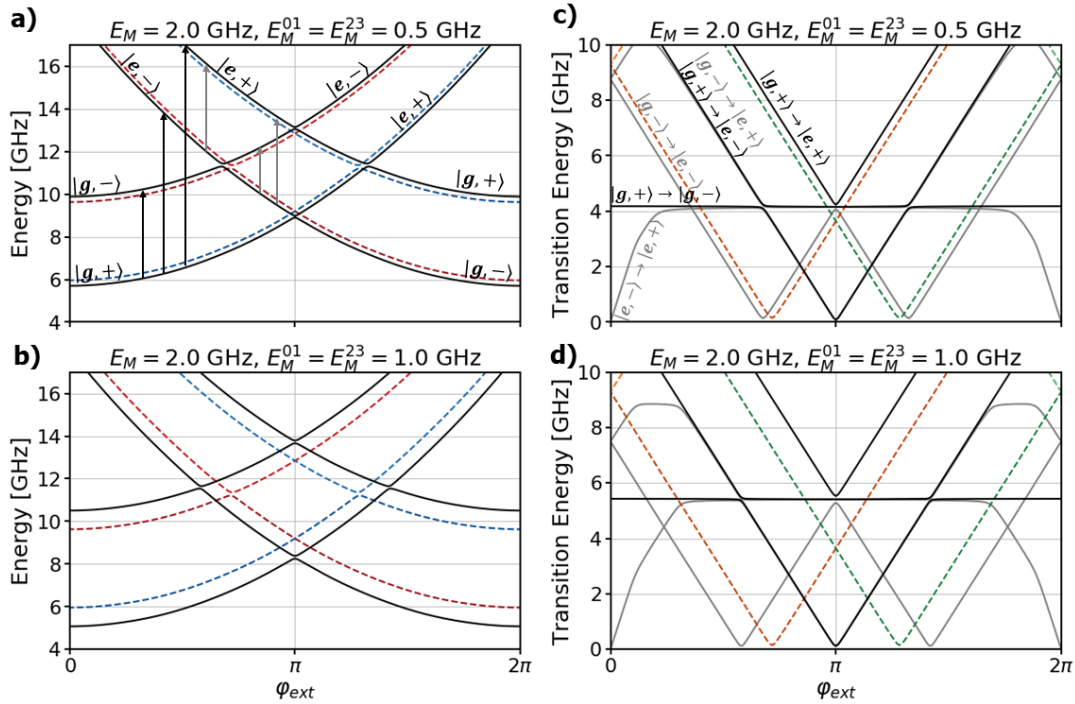


FIGURE 1.20: Same as figure 1.19 but now with $E_J/h = 14$ GHz instead of 8 GHz. Increasing the value of E_J increases the flux range over which some transitions are degenerate with each other. We observe this in the case of the $|g, -\rangle \rightarrow |e, +\rangle$ and $|g, +\rangle \rightarrow |e, -\rangle$ transitions, and also for $|g, +\rangle \rightarrow |g, -\rangle$ and $|e, -\rangle \rightarrow |e, +\rangle$.

A SWAP gate would be useful from the points of view of quantum computing with both superconducting qubits and topological qubits. First, due to the expected long coherence times of topological qubits, they could be used as quantum memories of the information processed in the superconducting circuitry. Having a simple way of realizing a SWAP gate would allow to directly exchange the processed information in fluxonium and store it in the Majorana qubit. Second, as we said before, braiding operations are topologically protected but they do not form a universal set of quantum gates. Being able to exchange the state of the topological qubit with fluxonium allows to complement these protected braiding operations with (unprotected) extra operations carried out on the fluxonium qubit.

Chapter 2

Design and fabrication

Figure 2.1 shows our overall chip design together with zoomed-in schematics of the most relevant elements in it. In this chapter we aim to explain the reasons for the incorporation of each of these elements in our design and the considerations behind the choice of their specific geometry and materials.

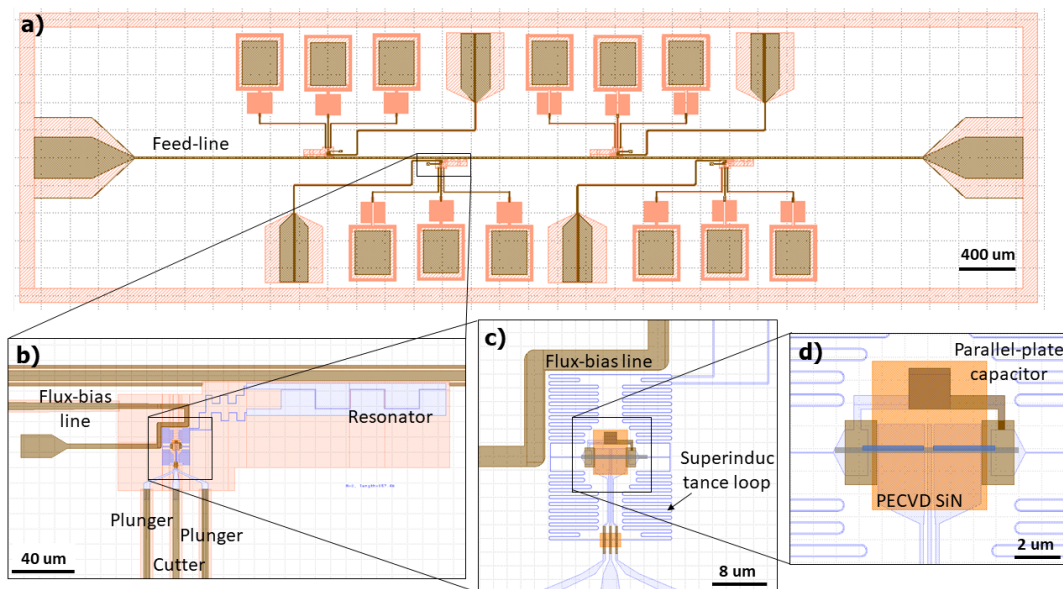


FIGURE 2.1: **Chip design overview.** White and light blue regions are thin (9 nm-thick) NbTiN. Pink indicates regions that have been etched out from the thin film. Brown shows thick NbTiN regions. Orange indicates dielectric windows. **a)** Schematic showing the whole 2×7 chip containing four nanowire fluxonium devices coupled to a feedline. One flux-bias line and three gate lines arrive to each of the devices. **b)** Enlargement of one of the devices showing the resonator, fluxonium, flux-bias line and gate lines. **c)** Enlargement of the fluxonium region showing the gradiometric design, gate jumps and fluxonium to resonator inductive coupling. **d)** Enlargement of the junction region showing the pre-patterned gates, dielectric window, wire, contacts, and capacitor.

Device fabrication starts by sputtering a 9 nm-thick film of NbTiN on a high resistivity ($>10\,000\ \Omega\text{cm}$) Si(100)/SiN(Low-stress-LPCVD) substrate. Relevant characteristics of this film are detailed in section 2.1. After that, most of the structures are defined by ebeam lithography and SF_6/O_2 reactive ion etching. Everything that is shaded in pink in figure 2.1 is etched out. In this step we define a lumped-element readout resonator and a superinductance loop to obtain the high inductance needed to shunt the fluxonium junction. Details of these structures are given in sections 2.2 and 2.3 respectively. In section 2.3 we also present the parallel-plate capacitor

used to obtain the wanted capacitance across the junction. Last fabrication step before nanowire deposition consists in sputtering thick (100 nm) NbTiN to make most of the elements shaded in brown in figure 2.1 (CPW feedline, flux-bias lines, gates bond pads, top capacitor plate and gate jumps). The designs of the flux-bias line and gate lines are explained in sections 2.4 and 2.5 respectively. Section 2.6 presents the nanowire deposition and junction etch details.

One last fabrication step right before measurement is wire bonding the chip. During this step, gate lines are connected to the dc lines on the PCB, the feedline is connected to the input and output coaxial lines and the flux-bias lines are connected to four extra coaxial ports. Apart from this, on-chip aluminum bonds crossing over control lines are included (not shown in figure 2.1). They connect interrupted regions of ground plane. This way, spurious modes are suppressed and the current from the flux bias lines is redistributed across the ground plane, reducing cross talk between different qubits and other unwanted effects.

2.1 NbTiN thin films on Si/SiN

In order to obtain an E_L of around 0.6 GHz we need an inductive element with a high inductance (of around 100 nH). However, we want it to have a low enough stray capacitance C_s such that its self-resonant frequencies do not interfere with the frequency window of interest (between 1 and 12 GHz in our case). We therefore want C_s to be smaller than $1/(200 \cdot 10^{-9} \cdot (2\pi \cdot 12 \cdot 10^9)^2) \text{F} \simeq 0.9 \text{ fF}$. This inductor would have an impedance of $Z = \sqrt{L/C_s} \simeq 15 \text{ k}\Omega$, much greater than the superconducting resistance quantum $R_Q = 6.5 \text{ k}\Omega$. A superconducting element with this characteristics is called a **superinductor** [74]. The inductance L of a radio-frequency circuit element measures the energy generated as a response to a current through it $E = \frac{1}{2}LI^2$. This energy is typically stored in a magnetic field around the circuit element and defines the regular magnetic self-inductance L_m . However, this inductance always comes together with a stray capacitance C_s , associated to the electric field around the circuit element. The $Z = \sqrt{L_m/C_s}$ impedance is restricted by the electromagnetic parameters of vacuum to be of the order of the vacuum characteristic impedance $Z_{\text{vac}} = 377.0 \Omega$, much smaller than R_Q . This means that one can not obtain a superinductor relying only on magnetic inductance [75], [90].

One way to implement a superinductor is to use Josephson junction arrays [10], [74]–[76], [91]. For excitation frequencies well below the plasma frequency of each junction, the array effectively behaves as a linear inductive wire. This happens because the phase drop across each of the junctions is small and the sinusoidal current-phase relations can be approximated to first order. If the array is sufficiently long and the parasitic capacitance to ground of the sections between junctions is small enough, one can reach the superinductance regime.

An alternative approach is to use disordered superconductors with a high kinetic inductance [90], [92], [93]. This is what we have done in this work. In what follows, we explain what is kinetic inductance and how to implement a superinductor with it.

2.1.1 Kinetic inductance

As we said, L_m measures the energy stored in the magnetic field as a response to a current. Any current comes also together with some kinetic energy stored in the

motion of the charge carriers E_k . The inductance that measures this kinetic energy is called kinetic inductance L_k . We have

$$E_k = \frac{1}{2}L_k I^2. \quad (2.1)$$

The kinetic energy of the charge carriers can be expressed as

$$E_k = \frac{1}{2}\rho l A m_e v^2 \quad (2.2)$$

where ρ is the density of the Cooper pair condensate, l and A are the length and cross section of the conductor, m_e is the electron mass and v is the carrier velocity. Comparing with equation 2.1, we have

$$L_k = \frac{m_e l}{\rho e^2 A}. \quad (2.3)$$

This type of inductance is in principle present in any conductor and contributes to the impedance with $Z_{L_k} = \omega \frac{m_e l}{\rho e^2 A}$, at frequency ω . However, for normal metals the Drude resistance $R_D = \frac{m_e l}{\tau \rho e^2 A}$, where τ is the momentum relaxation time, dominates Z_{L_k} up to the terahertz range [74]. Only for superconductors with $\omega\tau \gg 1$ the inertia of charge carriers becomes relevant.

The greater the disorder in the superconductor, the lower ρ and the greater the kinetic inductance. Examples of disordered superconductors with high kinetic inductance are Nb, NbN [90], NbTiN [93], [94] and TiN [95]. In our case we use a NbTiN thin film to fabricate the superinductor shunting the junction (section 2.3.2) and also the inductive part of the readout resonator (section 2.2).

The value of L_k is strongly dependent on temperature. For temperatures much smaller than the critical temperature T_C we can estimate L_k knowing only the value of T_C and the sheet resistance at room temperature R_s [90],

$$L_k(T \ll T_c) \simeq \frac{R_s h}{2\pi^2 1.76 K_B T_C}. \quad (2.4)$$

The thinner the film the lower its T_C and the greater its R_s . Therefore, thinner films have larger kinetic inductances. Also, as shown in equation 2.3, longer and narrower strips have larger L_k . There are multiple reasons why a narrow and thin strip is more convenient to fabricate our superinductance loop. First, if the film thickness t and width W are small, the field compatibility increases (details in the next section), and being able to operate at fields of around 1 T is essential to enter the topological regime with the currently available materials. Second, if the film inductance is high, the same total inductance can be achieved by using a shorter strip, which will have a lower stray capacitance to ground and therefore a resonance frequency further away from the region of interest. And third, the shorter the loop the smaller the area enclosed by it, and as a consequence the lower the sensitivity to flux noise.

We therefore use the thinnest film that maintains a high enough homogeneity of material parameters. In order to investigate the optimum thickness we deposit films with t ranging from 8 to 22 nm maintaining the same deposition parameters for all of them and varying only the sputtering time. Measured T_C and R_s values, together with the corresponding L_k are shown in table 2.1 for different film thicknesses.

t (nm)	T_C (K)	R_s (Ω/\square)	L_k (pH/ \square)
7	7.2	348	67
9	7.6	199	36
11	8.5	153	19
22	9.7	66	9.7

TABLE 2.1: Measured critical temperature T_C and sheet resistance at room temperature R_s and extracted kinetic inductance L_k (using equation 2.4) for NbTiN films with different thicknesses t .

Kinetic inductance depends very strongly on t , and therefore also on the deposition time. This time is controlled manually, and differences of around 1 s can have an impact on L_k of tens of pH/ \square . The deposition rate also varies over time, even maintaining the same deposition parameters. This means that it is very difficult to predict the kinetic inductance of a film before deposition. The film used for the fabrication of the fluxonium devices measured in this work (chapter 3) has a thickness of around 9 nm, which, for the sputtering recipe used in this work, corresponds to a deposition time of 20 s and a kinetic inductance of around 41 pH/ \square .

2.1.2 RF properties

To characterize the RF properties of the film, we fabricate lumped-element resonators capacitively coupled to a coplanar waveguide feedline. We measure transmission S_{21} through the feedline around the resonances. By comparing the resonant frequency to S_{21} simulations done with Microwave Office we can extract the value of the film L_k . Furthermore, by fitting the transmission data around the resonance, we extract the resonator internal quality factor Q_i , which is a measure of the loss at the dielectric below the superinductor.

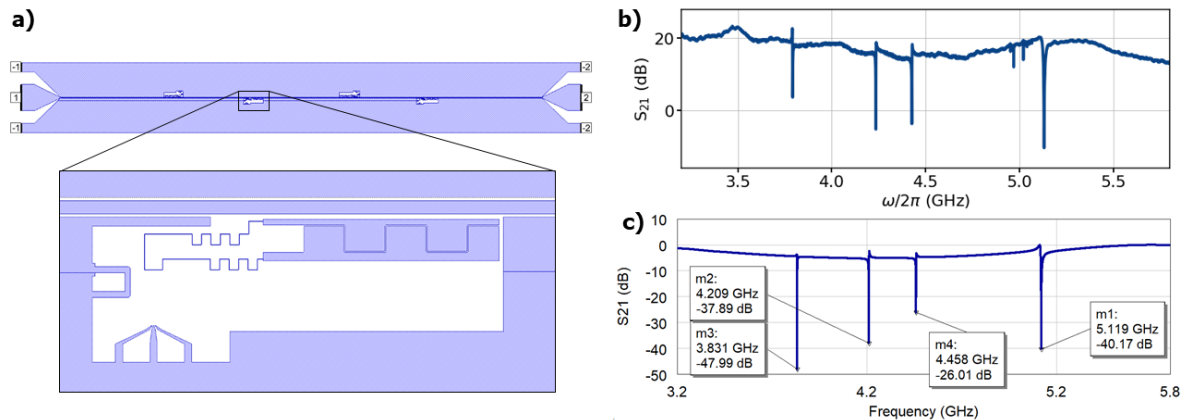


FIGURE 2.2: Extraction of L_K by comparing measured S_{21} (panel b) with Microwave Office simulations (panel c). Absolute value of the background transmission is not expected to be equal in both cases, due to the presence of attenuators, filters and amplifiers that are not taken into account in simulations. Measurement in b) is taken at 270 mK Panel a) shows the geometry of the simulated chip.

Figure 2.2 shows a comparison between the measured S_{21} versus frequency and the corresponding simulation for a chip with the same geometry. For this specific

example, the calculated L_k of the film (using the analytic formula 2.4) was $25 \text{ pH}/\square$. Comparing the measured resonant frequencies to the simulation results for different L_k values, the best agreement was found for $L_k = 29 \text{ pH}/\square$. The corresponding resonance frequencies are shown in table 2.2.

Measured frequencies (GHz)	Frequencies from simulations (GHz)
3.79	3.83
4.23	4.21
4.43	4.46
5.13	5.12

TABLE 2.2: Comparison between measured resonant frequencies and simulations using $L_k = 29 \text{ pH}/\square$.

The small difference between the analytically estimated L_k value for the NbTiN film and the one obtained with simulations was observed for all films studied. The reason for this may be an increase in kinetic inductance for the narrow strips that form the resonators (see section 2.2) with respect to the one measured for an extended film, due to a greater disorder close to the strip edges.

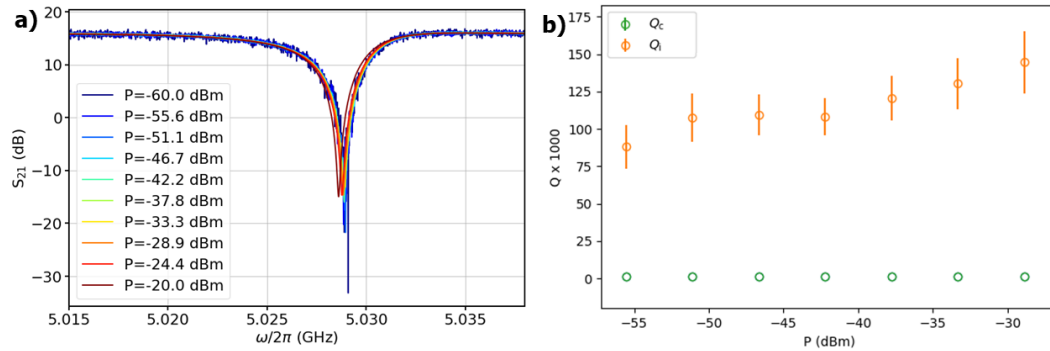


FIGURE 2.3: **RF characterization of NbTiN film at $B = 0$ and $T = 270 \text{ mK}$.** **a)** Example of a resonance measured for different input powers. **b)** Internal (orange) and coupling (green) quality factors extracted from fits of the resonance, as a function of input power.

In order to extract the film internal quality factors we fit the measured resonances with the diameter correction method (DCM) [96], which was shown to be better than other fitting methods when the asymmetry of the resonance is high (if the feedline is mismatched for example), since it accounts for a rotation of the resonance circle in the complex plane plus a diameter growth. This is done in practice by allowing Q_e to have an imaginary part. Figure 2.3 shows the power dependence of one of the resonances together with the quality factors extracted from the fits. The position and shape of the resonance stays almost fixed in the power range studied here. This indicates the absence of non-linear effects in this range of powers, and validates the single-mode resonator approximation that we did in chapter 1. Q_i 's extracted range between 10^4 and 10^5 for different films and powers, indicating that the dielectric losses are low and that the quality of the film is good enough for the intended applications. Regarding the coupling quality factors Q_c , also extracted from these fits, they range between 10^3 and $2 \cdot 10^3$ for the resonators used in this work.

2.2 Lumped element readout resonators resilient to magnetic field

We optimize the geometry of the readout resonators to minimize vortex generation and movement, and therefore to be able to operate at in-plane magnetic fields of the order of 1 T maintaining the high internal quality factors Q_i found for $B = 0$.

Vortices appearing in regions that carry microwave currents can alter the distribution of these currents and change the magnitude of the resonator inductance. If the dynamics of these vortices is unstable, frequency fluctuations can reduce the resonators Q_i . Furthermore, since vortices cores are no longer superconducting, the presence of vortices in our resonator could cause energy dissipation and also contribute to the decrease of Q_i .

Different approaches have been taken in previous works to deal with these type of effects. One option is pre patterning holes in the thin NbTiN film [97]–[99]. Holes act as defects that pin the vortices and prevent them from moving. This has been shown to increase Q_i by several orders of magnitude for CPW resonators [99]. A second alternative is to use narrow superconducting strips to prevent the formation of vortices [93], [94]. Our design combines these two methods. We use lumped-element readout resonators with a mainly inductive part and a mainly capacitive part. The highest current (inductive) part is very narrow (200 nm) and the capacitive part, which has a larger area, has artificial pinning sites of radius 40 nm. The geometry of these resonators is shown in figure 2.4. Figure 2.5 d) shows the simulated current distribution at the resonant frequency. As we see, most of the current is localized in the narrow meandering part.

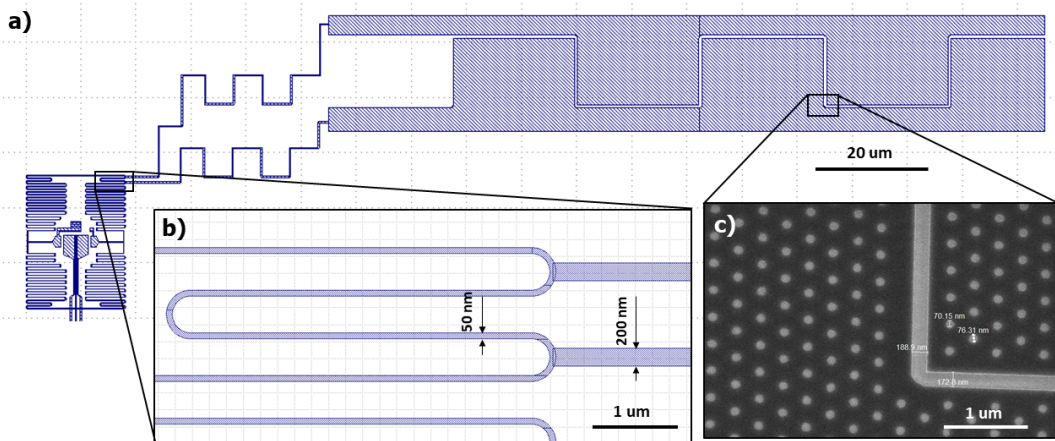


FIGURE 2.4: **Readout resonator.** a) Lumped element resonator coupled to the fluxonium superinductance loop. b) Enlargement of the coupling point. Shared inductance is around 20 % of the total resonator inductance. c) SEM image of the holes for vortex pinning.

2.2.1 Narrow strips to minimize the appearance of vortices

Vortex generation and dynamics on narrow type-II superconducting strips has been studied by several groups [100]–[102], finding that there is a critical field B_k below which no vortex trapping occurs when the device is cooled down in field. Different models predict different expressions for the magnitude of this critical field. However, even if the prefactor A of order 1 varies for different publications, the strip

width W dependence is consistently found to be of the form

$$B_k = A \frac{\Phi_0}{W^2} \quad (2.5)$$

with $\Phi_0 = \frac{h}{e}$ being the magnetic flux quantum. These models make two main assumptions. First, that the Pearl length $\Lambda = 2\lambda_L^2/t$, where λ_L is the London penetration depth and t the film thickness, is much larger than W . And second, they assume that the superconductor coherence length ξ is much smaller than W .

Regarding $\Lambda \gg W$, it is always fulfilled if the cool-down happens in field, because then the relevant λ_L is the one at T_C , when vortices are generated. In our case we turn the field on at base temperature, so λ_L has a much smaller value than the one at T_C and for typical superconductors the condition is not necessarily satisfied if the strips are very narrow. However, for disordered superconductors the effective field penetration depth λ_{eff} is larger than λ_L [67, p. 3.10.4]. For our 9 nm NbTiN film with $T_C = 7.7$ K and resistivity $\rho = 350 \mu\Omega\text{cm}$ we have [103, Appendix 9.2 (d)] [67, Eq. 3.120]

$$\lambda_{eff} = \sqrt{\frac{\hbar\rho}{\pi\mu_0\Delta_0}} \simeq 220\text{nm} \quad (2.6)$$

and therefore $\Lambda \simeq 10 \mu\text{m}$. Here, μ_0 is the vacuum permeability and $\Delta_0 \simeq 1.76K_B T_C$ is the superconducting gap at $T = 0$.

Regarding the assumption $\xi \ll W$, for a disordered superconductor and at zero temperature we have [103, Eq. 9.28]

$$\xi_0 = \sqrt{\frac{\Phi_0}{2\pi B_{c_2}}} \simeq 6 \text{ nm} \quad (2.7)$$

where we have used a (non-measured for this specific film) typical upper critical magnetic field B_{c_2} of 10T.

This means that we can use the expressions for the vortex nucleation critical fields for strip widths $6\text{nm} \ll W \ll 10\mu\text{m}$.

As we said, for our resonators we have $W = 200\text{nm}$. Taking $A = 1.65$ from reference [102] and using equation 2.5, we have a vortex critical **out-of-plane** field of $B_k = 1.65 \cdot \Phi_0(\text{Tm}^2)/(200 \cdot 10^{-9})^2\text{T} = \mathbf{83mT}$. We could do the same to estimate the vortex critical **in-plane** field, taking now as W the thickness of our film (9 nm). We obtain critical in-plane field of **40T**. We have to consider, however, that in this case $W \simeq \xi$ so we do not longer fulfill the conditions for the validity of the expression for B_k and this number is only a coarse estimate.

These results agree with the measurements of narrow strip NbTiN resonators very similar to ours in reference [94]. They find that the performance of the 8nm-thick 200nm-wide resonator is affected by magnetic field. The fields needed to shift the resonant frequency by a 1% are in their case ~ 5 T for in-plane field case and ~ 120 mT for out-of-plane.

DC signatures of Majorana states in InAs nanowires have been found at in-plane fields lower than 1 T [21], [40] and typical perpendicular fields in our experiments can go up to 2 mT during flux tuning and field alignment. We can therefore safely say that our resonators are compatible with the field conditions necessary to enter the topological regime.

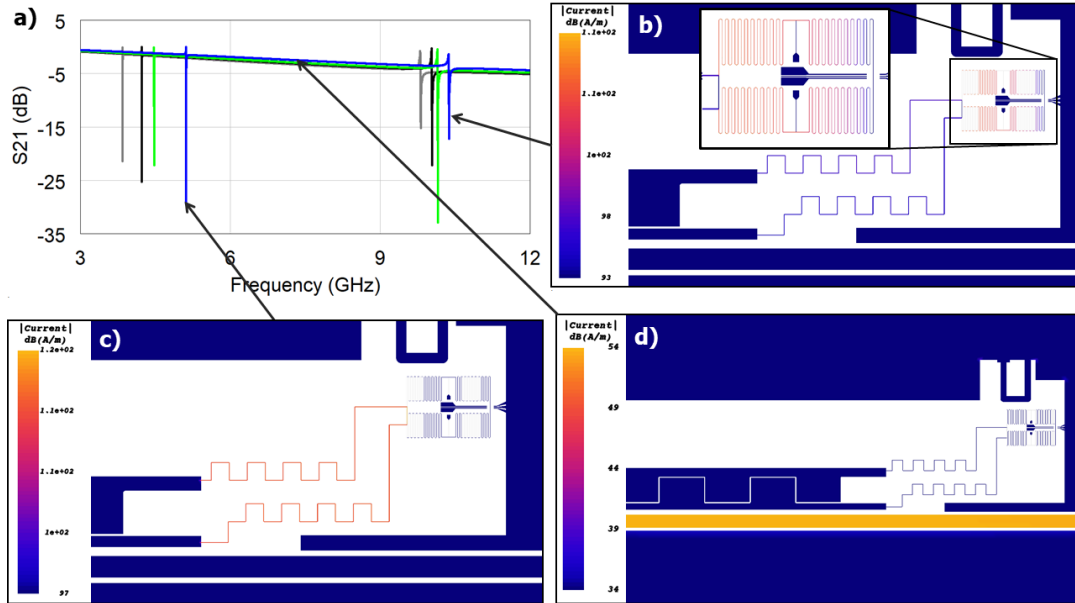


FIGURE 2.5: **Current distribution at different resonant frequencies.** a) Simulated S_{21} trace for four different devices coupled to the same feedline. Apart from resonances situated at the expected resonator resonant frequency, extra resonances appear at higher frequencies. b) Current distribution in one of the devices at the higher resonance. Most current is localized at the fluxonium superinductance loop. c) Same as b) but now for a frequency point with high transmission. Most current is now localized at the waveguide. d) Same as b) but now for the higher resonant frequency. Most current is now localized at the thin meandering part of the resonator.

2.2.2 Artificial pinning sites to trap vortices

Regarding the capacitive part of the resonators, we use interdigitated capacitor plates to increase capacitance while maintaining a small footprint. Still, this part is wider than the meandering part (it has uninterrupted regions of up to $16.8 \times 22.0 \mu\text{m}$), big enough for vortices to generate in the capacitor plates. The vortex critical field corresponding to a width of $17 \mu\text{m}$ is just $11 \mu\text{T}$. Only the earth magnetic field is already $49 \mu\text{T}$ in Delft [104] so vortices are for sure going to be trapped in the plates during cooldown.

This effect would not be a big problem in principle, since these vortices will appear only away from the areas carrying the highest currents (see figure 2.5). Even so, we decided to incorporate holes in this region to minimize effects coming from the vortices movement (figure 2.4 c)). They are arranged in an hexagonal pattern with a distance between holes of 320 nm and a hole radius of 40 nm . This corresponds to a hole density of $12 \mu\text{m}^{-2}$. In reference [99] it has been shown that vortices are strongly pinned by holes up to a threshold **out-of-plane** field for which each hole is filled with a single vortex. For our hole density this field would be $\sim 20 \text{ mT}$, higher than the maximum out-of-plane field we achieve in a typical experiment.

2.3 Design for E_C and E_L

As we discussed in chapter 1, the magnitude of E_J can be tuned using the cutter gate. However, E_C and E_L are fixed by design.

We aim for an E_C of around 2.4 GHz and an E_L of around 0.7 GHz. To obtain the wanted E_C we include a parallel plate capacitor across the junction (figure 2.6 a), section 2.3.1). The high inductance necessary for E_L comes from a long meandering NbTiN path shunting the junction (figure 2.6 b), section 2.3.2).

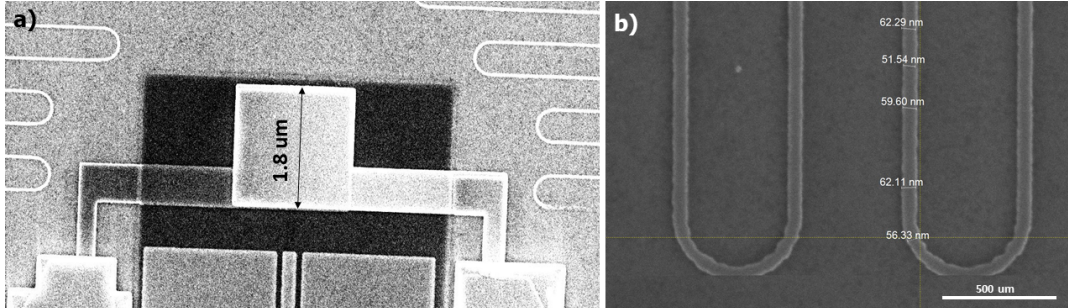


FIGURE 2.6: **Design for E_C and E_L .** **a)** SEM image of the parallel plate capacitor determining E_C . The black window is the SiN used as capacitor dielectric. **b)** SEM image of the high kinetic inductance long meandering path that determines E_L .

2.3.1 E_C : parallel plate capacitor

To determine the geometry of the capacitor that fixes E_C we simply use the equation for the capacitance of a parallel plate capacitor $C = \epsilon_r \epsilon_0 A / d$. Where $\epsilon_0 = 8.85 \cdot 10^{-15}$ is the permittivity of vacuum, ϵ_r is the dielectric constant, A is the plate area and d is the distance between plates.

Relating this capacitance to E_C using equation 1.19, and assuming a square plate with side l , we obtain this relation between l and E_C

$$l = \sqrt{\frac{e^2 d}{2\epsilon E_C}}. \quad (2.8)$$

We use, as dielectric, 29 nm-thick PECVD SiN, which is expected to have a dielectric constant of around $\epsilon_r \sim 8$. In order to have $E_C/h = 2.4$ GHz we need therefore $l = 1.8 \mu\text{m}$ (see figure 2.6 a)).

Variations of d and ϵ_r with respect to the expected values may change the value of E_C . For this reason, we try to use stable fabrication recipes and characterize the dielectric thickness and dielectric constant after deposition. Knowing the value of E_C in advance as well as possible provides a good initial estimate of the fit parameters when fitting the fluxonium spectra afterwards.

2.3.2 E_L : superinductance meandering path

E_L is determined by the kinetic inductance and geometry of a superinductance loop shunting the junction. Invoking equation 1.21, we see that in order to have E_L/h around 0.7 GHz we need a value of around 110 nH for the loop inductance.

We take 50 nm for the width of the meandering path that forms this loop. This is the thinnest width that allows maintaining homogeneity along the superinductor strip without risk of having it break. It is desirable to have it as narrow as possible for different reasons. First, to avoid the formation of vortices and therefore minimize decoherence effects resulting from changes in the value of E_L . The

critical out-of-plane field for vortices is, using equation 2.5 with $W = 50 \text{ nm}$, $B_k = 1.65 \cdot \Phi_0(\text{Tm}^2)/(50 \cdot 10^{-9})^2 \text{T} = 1.3 \text{ T}$, large enough to completely avoid the formation of vortices in the loop. Second, to reduce the total length of the superinductor and minimize the loop area (which reduces the effect of magnetic field noise on the external flux, helping also to reduce decoherence). Having a shorter strip is also beneficial because it reduces the stray self-capacitance of the loop. These are also the reasons why we aim for a high film kinetic inductance, having a larger L_K reduces the needed strip length, decreasing both self-capacitance and flux noise.

A second design aspect to consider is the separation between meanders. In this case they are separated by a distance 10 times larger than the path width. This contributes to the minimization of the stray-capacitance, avoiding the self-resonance frequency of the superinductance loop to end up inside the frequency window of interest. In figure 2.5 we showed the simulated S_{21} resonances for the resonator-fluxonium system. We see that, apart from the expected resonator resonances around 5 GHz, extra resonances appear at higher frequencies. The localization of the current in the fluxonium loop at these resonances (figure 2.5 panel b)) suggest they originate from this unwanted effect. For the final design, the ground plane was brought further away from the fluxonium loop, reducing capacitance and therefore bringing the loop resonance to higher frequencies.

As for the case of E_C before, it is important to estimate the value of E_L as well as possible before measurement. For this reason, we fully characterize the fabrication recipes in advance and monitor the path width for different devices to know E_L as precisely as possible.

2.4 Gradiometric design and flux-bias line design

Another important aspect of our design is the gradiometric shape of the superinductance loop. It helps both diminishing the device sensitivity to global flux noise and decoupling the global magnetic field knob for the topological regime from the flux knob that tunes the fluxonium spectrum. This design consist on doubling the superinductance loop symmetrically at both sides of the junction and is shown in figure 2.7. Ideally, the two symmetric sub-loops have exactly the same area (figure 2.7 a)). The presence of a global magnetic field noise would result in equal fluxes in both loops of the gradiometer, resulting in two propagating currents in the same direction that would cancel each other at the shared branch, where the junction is placed. This effect would therefore cancel the influence of any global flux noise over the phase across the junction, eliminating an important source of decoherence.

This gradiometric topology, however, does not cancel *local* flux. This has a down side, it does not get rid of sensitivity to local flux noise coming from isolated spins or unwanted current flowing close to the loop. However, it allows us to tune the effective flux Φ_{ext} by having an asymmetric flux-bias line that couples much more strongly to only one of the loops (figure 2.8). A dc current I is sent through the flux line, which is shorted to ground at its end (see the zoomed out design in picture 2.1). The mutual inductances between the line and each of the two loops (M_A and M_B) determine the flux that is thread through them as a consequence of the current.

$$\Phi_A = IM_A \quad \Phi_B = IM_B \quad (2.9)$$

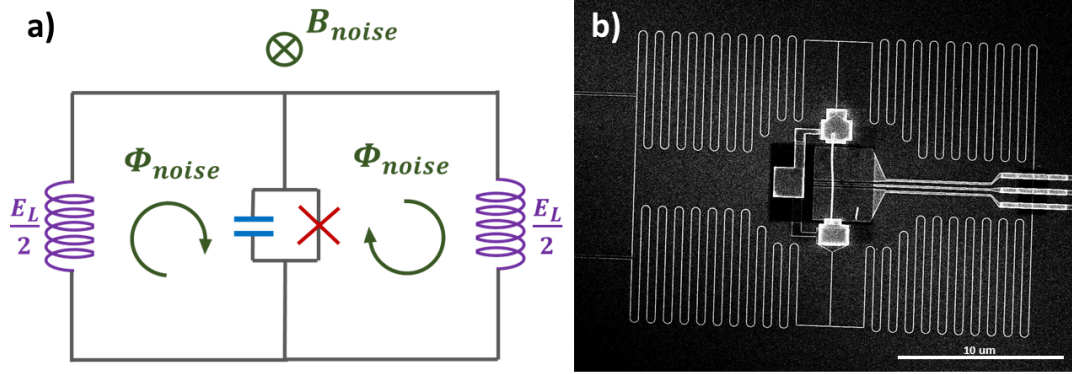


FIGURE 2.7: **Gradiometric design.** a) Schematic representation of two symmetric loops and global flux noise cancellation. b) SEM image of the loop, with gates and capacitor breaking the symmetry.

Knowing M_A and M_B one can calculate the current needed to thread an effective flux of one flux quantum Φ_0

$$\Phi_0 = \Phi_A - \Phi_B = I(M_A - M_B) \rightarrow I = \frac{\Phi_0}{M_A - M_B}. \quad (2.10)$$

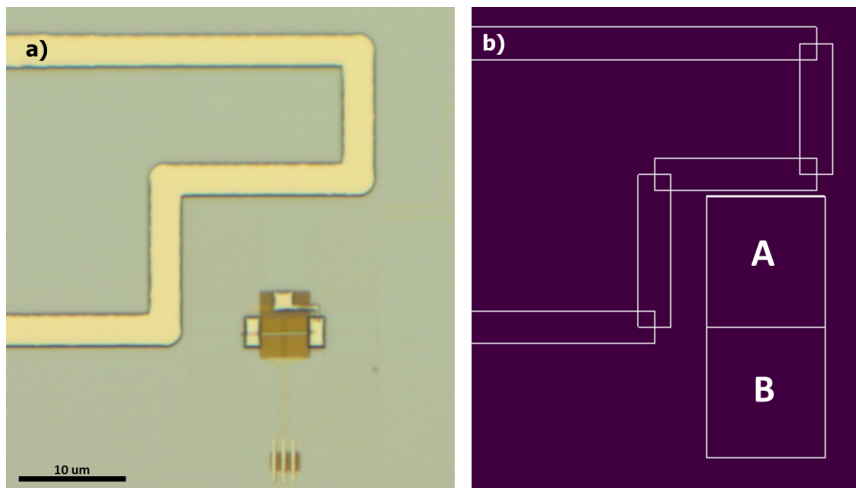


FIGURE 2.8: **Flux-bias line design.** a) Optical image of the 100 nm thick NbTiN flux-bias line. The fluxonium loop, being much thinner and narrow, is difficult to distinguish in an optical image. b) Simplified model of the flux-bias line and the two loops for numerical calculations using FastHenry.

We calculated numerically the mutual inductances M_A and M_B for various flux-bias line designs. Figure 2.8 b) shows the simplified geometry used for the simulations. The design shown here is one of the possibilities that result in a larger difference in mutual inductances. Applying equation 2.10 we obtain 1 mA for the current needed to drive a difference of one flux quantum through the two loops. To avoid problems coming from a low critical current of the line, we fabricate it with a 100 nm-thick film, much thicker than the one used for other structures in the chip (see 2.8 a)).

We fabricated devices with this fluxline design, which has the line only 500 nm away from the fluxonium loop. However, devices with an alternative design, with a less coupled line for which a current of 13 mA is needed, were also fabricated. A

less coupled line results both in a lower contribution to the loop capacitance and in a lower sensitivity to noise coming from possible vortices generating at the line. Both designs will be studied in experiments.

One last point to consider is the possibility of using the out-of-plane component of the fridge magnet to drive a flux. In principle, this should not be possible due to the gradiometric design. However, in practice the loops will not be totally symmetric, due to extra elements like the capacitor and the gate lines (figure 2.7 b)). The magnetic field corresponding to a flux quantum through one of the $12 \times 11 \mu\text{m}$ loops is $15 \mu\text{T}$. Due to the always present asymmetry in the gradiometer, using a field some orders of magnitude larger than this could lead to the effective flux difference between loops.

2.5 Gate-lines design

In order to tune the potential at the junction and at the proximitized section, one needs at least three independent gate lines arriving at the junction position. The central gate, the **cutter**, tunes the junction conductance, and therefore the value of E_J . The chemical potentials of the two superconducting sections of the wire are controlled independently by two extra bottom gates, the **plunger** gates. Their purposes is to drive the superconducting sections into the topological regime. Ideally each gate influences only the wire section above it. In practice, however, one always observes cross-talking between gates. After characterizing this effect experimentally one could create digital gates combining the potential of the three to maintain E_J fixed when the plunger gates are tuned.

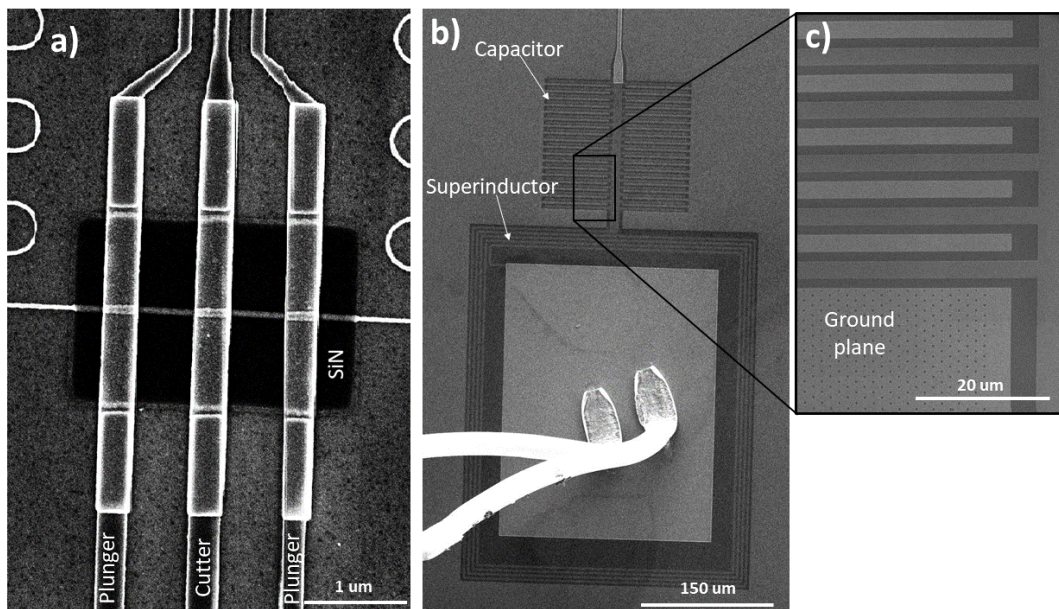


FIGURE 2.9: **Gate lines design.** **a)** Gates jump to cross over the superinductance loop. Black window is the 29 nm-thick SiN dielectric used to separate the gates from the loop section. **b)** Gate bonding pad showing the LC on-chip filter and to wire bonds. **c)** Enlargement of the capacitive part of the filter.

Since the wire position is surrounded by the gradiometer in all directions, the gate-lines have to bridge the inductor. One possibility would be to use air bridges. However, in this work we use a dielectric patch, which may lead to losses but is easier to fabricate. This is shown in figure 2.9 a), where the 9 nm thin gate lines are interrupted at the edges of the dielectric and reconnected using 100 nm-thick NbTiN patches.

Figure 2.9 also shows the LC filters included on chip right after the gate bonding pads. They are formed by a long spiraling strip of thin NbTiN, that constitutes the inductive element, and an interdigitated section with a high capacitance to ground (enlarged in figure 2.9 c)). These filters reduce any unwanted high frequency noise arriving to the gates.

2.6 Nanowire deposition and junction etch

VLS InAs nanowires are grown vertically in a growth chip, from which they are transferred into the processed chip using a micromanipulator under an optical microscope. The wire is deterministically deposited on top of the three gates covered by SiN dielectric, ensuring that both wire ends lay on top of the prepatterned contacts.

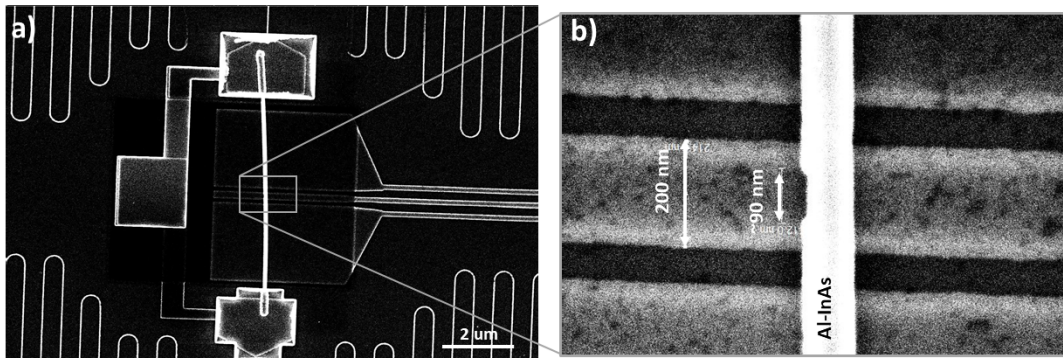


FIGURE 2.10: **Nanowire junction.** **a)** SEM image of the InAs nanowire deposited on top of the gates and contacted at both ends with NbTiN contacts. **b)** Enlargement of the junction region, showing the 80 nm-long junction aligned on top of the cutter gate.

Most fabrication steps are done before nanowire deposition, minimizing the post-deposition steps, that can detriment the wire quality, as much as possible. Two of this steps are junction definition and contacts deposition. The junction is made selectively removing a section of the Al shell by wet chemical etching. A resist mask is created and the chip is immersed in warm Transene D for some seconds. By controlling precisely the temperature and immersion time, different junction lengths can be achieved. All junctions in this work have a length of around 80 nm (figure 2.10 b)).

Together with the junction etch, two Al sections at both ends of the wire are also removed, uncovering the parts of the wire that will be contacted. After that, two NbTiN contacts are deposited, overlapping the wire end and the prepatterned contact to the loop.

After this, the device is wire bonded and ready to be loaded in the fridge and measured.

Chapter 3

Spectroscopy measurements

Before being able to operate the nanowire fluxonium as a qubit, realizing quantum gates useful for quantum information, different characterization measurements must be carried out. This chapter presents the characterization measurements that have been realized until now on the first generation of devices, both at zero field and applying an in-plane magnetic field.

We will start by introducing the details of the measurement setup, focusing on how the drive and readout signals arrive to the chip and on the treatment of the output signal before digitalization (section 3.1). After that, in section 3.2, we will go through the simplest measurements that can be done, measuring the transmission for fluxonium in equilibrium and studying the effect of fluxonium on the resonator. The device can be further characterized at zero field using two-tone spectroscopy to excite the qubit to higher energy levels. These measurements are presented in section 3.3. Finally, we present the study of the device field compatibility, with particular focus on the field dependence of E_J . With this we will end the chapter in section 3.4.

3.1 Measurement setup

Experiments are performed in a dilution refrigerator with operating temperatures of around 10-20 mK, low compared to the relevant energy scales in order to reduce unwanted effects coming from thermal noise of the order of $K_B T$. Figure 3.1 shows the measurement setup, including the fridge wiring and the electronics at room temperature.

Four different RF sources are used, each for a different purpose. Two of them are used to generate the readout and the drive tones, that together form the input signal. A third source is slightly detuned from the readout tone and is used as local oscillator (LO) for heterodyne interferometry purposes. The last source is used as a pump for the TWPA amplifier included in the output line [105], [106]. DC blocks are included at the output of each RF source, to make sure that no DC signals enter the fridge.

The readout tone, which is typically set at a frequency close to the resonator resonance frequency, and the qubit drive, used to excite the different energy levels of the device, are merged together and sent through the input line. This line is attenuated at different temperature stages before arriving to one of the launchers of the on-chip feedline. A variety of other lines also arrive to the chip. The current generated with Yokogawa current sources is sent to the flux-bias lines via four filtered and attenuated coaxial lines. Regarding the gates, they are connected via low-pass filtered DC

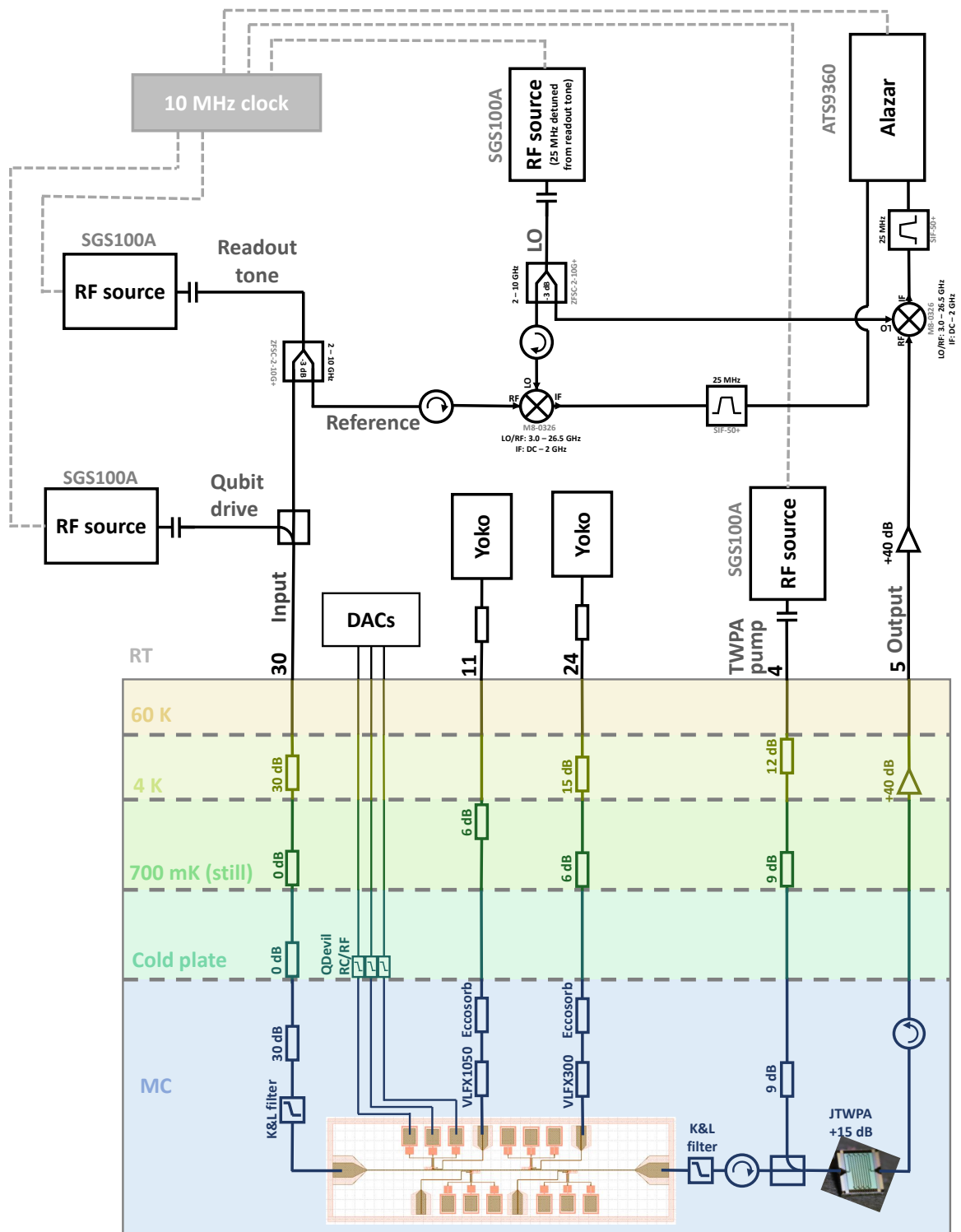


FIGURE 3.1: **Schematic diagram of the fridge wiring at cryogenic and room temperatures.** Different background colors indicate different temperature stages. Qubit drive and readout tone arrive at the chip through a common line, the input line, which is attenuated at different temperature stages. The output signal is amplified inside the fridge, downconverted to 25 MHz and digitalized.

lines to multiple DC voltage sources with a range of ± 10 V. The output RF signal leaves the fridge through a line containing two circulators that protect it from high temperature noise coming from the higher temperature stages. The output line is also amplified, at base temperature with a TWPA and at higher temperature stages with two more amplifiers.

Figure 3.1 also shows the room temperature heterodyne interferometry setup. The output readout signal is mixed with the LO tone, detuned from the readout frequency by 25 MHz. A reference signal at the same frequency and phase as the input readout tone, indicated as *Reference* in figure 3.1, is also mixed with the LO. Both downconverted signals are then band-pass filtered around 25 MHz and digitalized using an Alazar ATS9360. Comparing the frequencies and amplitudes of both signals, the complex transmission S_{21} is calculated.

To control the in-plane and out-of-plane magnetic fields we use a vector magnet, not included in figure 3.1. Maximum fields are around 6 T in the direction of the wire and in the in-chip direction perpendicular to the wire, and around 1 T out-of-plane. The magnet is connected to a room temperature high-voltage source.

3.2 S_{21} measurements

The most simple measurement that can be done in this setup is the measurement of the transmitted amplitude $|S_{21}|$ of a single microwave tone at a fixed frequency. This measurement probes the position of the resonator frequency, which varies due to the dispersive shift from fluxonium in its ground state (see section 1.2.2). Figure 3.2 shows the idea behind this type of measurement. A signal with complex amplitude V_1 and frequency ω is sent through the chip and a second signal at the same frequency, with amplitude V_2 , is detected at its output. Transmission S_{21} is calculated as V_2/V_1 and its amplitude is typically expressed in dB.

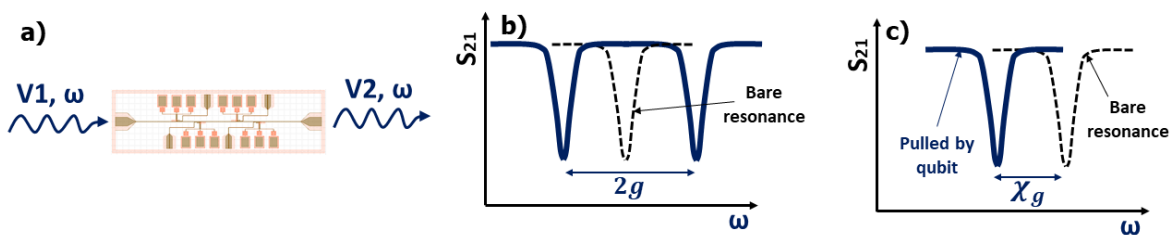


FIGURE 3.2: **Transmission measurement.** **a)** Schematic of the elements involved in an S_{21} measurement. **b)** Detected signal versus frequency when the resonator is in resonance with one of the fluxonium transitions. The bare resonance of the uncoupled resonator is indicated with a dashed line. **c)** Same as **b)** but for the dispersive regime. The resonance is shifted by χ_g with respect to its bare value when fluxonium is in the $|g\rangle$ state.

In an ideal S_{21} experiment one would observe a flat transmission excepting for four resonances coming from the four resonator in the chip. Figure 3.3 shows a transmission trace for the chip presented in this work. In this case, we observe some extra resonances and ripples that may come from the use of a thin non-impedance-matched feedline where standing waves can appear and from non flat behaviour of

different filters in the input and output lines.

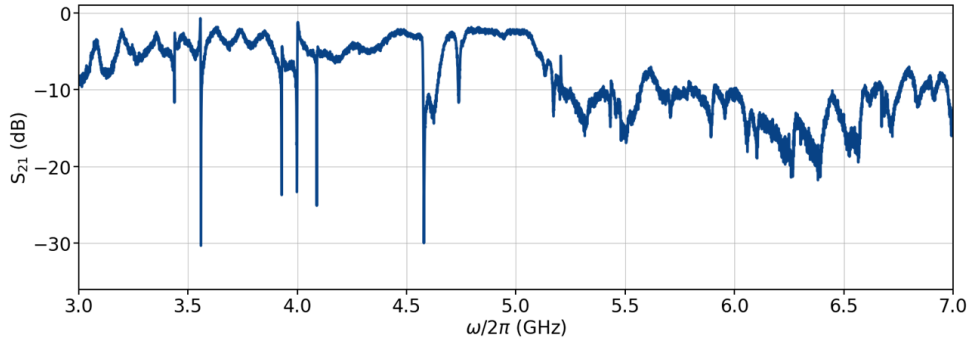


FIGURE 3.3: S_{21} trace versus readout frequency. Four of the observed resonances correspond to the four readout resonators and can be identified comparing the measurement to S_{21} simulations.

As we mentioned in chapter 1, the pull on the resonator depends strongly on the detuning of many fluxonium transitions. Several parameters of the system affect the distribution of fluxonium energy levels, so by varying them we expect to observe a shift in the pull over the resonator. In sections 3.2.1 and 3.2.2 we will zoom into one of the resonances and study its dependence on cutter gate voltage and external flux, respectively.

3.2.1 E_J dependence

As discussed in detail in section 1.3.1, by tuning the cutter gate voltage V_c we expect to observe a non-monotonic increase in the value of E_J , starting from a very low one at negative gate voltages and stabilizing again when V_c is of the order of 1 V.

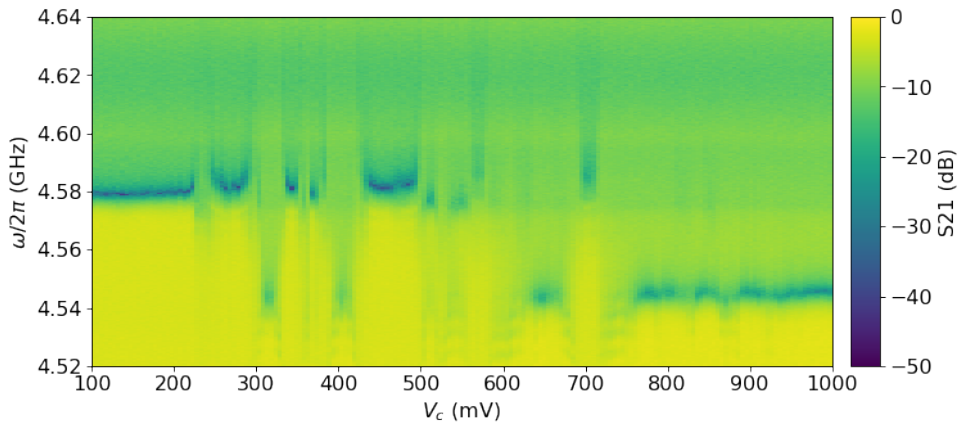


FIGURE 3.4: S_{21} trace versus readout frequency and cutter gate voltage. The avoiding crossings with fluxonium transitions at intermediate gate voltages agree with the expected non-monotonic increase of E_J .

This type of measurement is shown in figure 3.4. As expected, the position of the resonance varies with gate voltage. For negative V_c and up to $V_c \sim 225$ mV the position of the resonance is stable at 4.58 GHz. We interpret this regime as a low E_J regime where the lowest energy transitions are at low frequencies below the resonator (see simulated spectra at different E_J values in figure 1.11). At intermediate

V_c some avoided crossings are observed. They correspond to different fluxonium transitions getting in resonance with the resonator as E_J increases. Sometimes the avoided crossings indicate that the fluxonium level comes from below the resonator and other times from above. This agrees with the expected non-monotonic dependence of E_J on cutter. At large V_c 's the resonance stabilizes again at a lower frequency of around 4.54 GHz, agreeing with the stabilization of the supercurrent at high cutter voltages observed in previous work [86].

3.2.2 External flux dependence

To study the external flux dependence we stay at a fixed cutter voltage close to an avoided crossing, for which the fluxonium transitions are expected to be close to the resonator. For the chip presented here, the flux-bias line design was the most uncoupled one, presented in section 2.4, so it is not possible to explore a large Φ_{ext} using the flux-bias line. Instead, we do it by applying an out-of-plane field B_x of the order of 1 mT with the fridge magnet. Figure 3.5 shows these measurements for three V_c points.

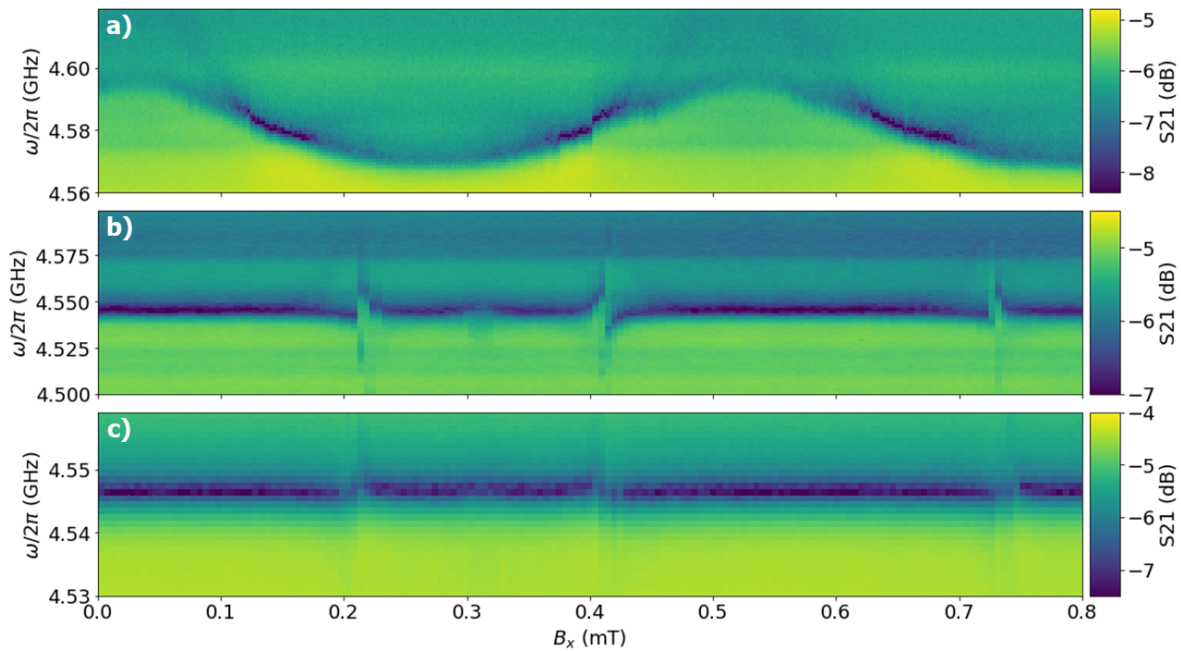


FIGURE 3.5: S_{21} trace versus readout frequency and external flux. Panels a), b) and c) are taken at $V_c = 432$ mV, 950 mV and 1710 mV respectively.

These measurements can be compared to column i) in figure 1.11, agreeing with the expected behaviour of the resonator pull when increasing E_J , with the dispersive shift becoming smaller for larger E_J values when the resonator is detuned from the second fluxonium transition. For the lowest E_J data, we observe dispersive shift differences as large as 30 MHz for different flux points. An out-of-plane field of around 550 μ T results in one effective flux quantum ($\Phi_{\text{ext}} = \Phi_0$). Comparing this to the 15 μ T needed to thread a flux quantum trough one of the two symmetric loops, proves the effectiveness of the gradiometric design, which reduces the effect of global flux noise by more than one order of magnitude.

3.3 Two-tone spectroscopy

As mentioned in section 1.2.2, the state dependence of the dispersive shift can be used to read out the state of the qubit. This state dependence can also be used to experimentally characterize the fluxonium spectrum. Fixing a readout tone at the bottom of the resonance for the system in equilibrium and using a second drive tone with variable frequency, one can detect different transitions. When the drive frequency does not match any fluxonium transition, the monitored transmitted amplitude of the readout tone will be low. If the drive tone frequency matches one of the fluxonium transitions that start from a populated state, it will drive Rabi oscillations. The change in occupation probabilities of the different states results in a change on the resonator pull. In this case the readout tone will not be at the bottom of the resonance anymore, showing a peak in transmission. An schematic for a two-tone measurement is shown in figure 3.6.

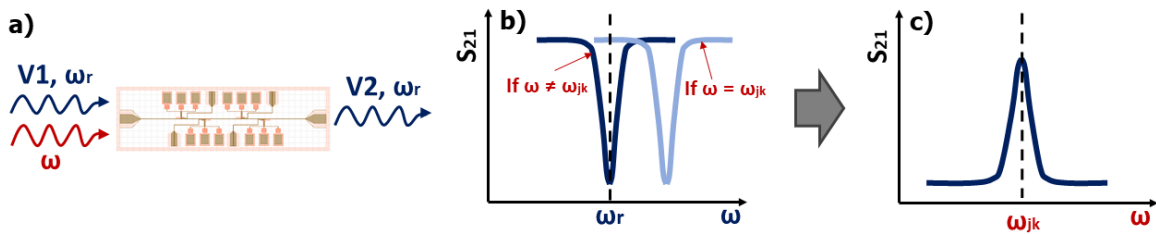


FIGURE 3.6: **Two-tone spectroscopy measurement.** **a)** Schematic of the elements involved in a two-tone measurement. In contrast to what is shown in figure 3.2, now the readout frequency ω_r is fixed and the frequency ω of a second drive tone is varied. **b)** When the drive frequency matches one of the fluxonium transitions, the pull on the resonator changes and its resonance moves from its initial position (in dark blue) to a shifted position in frequency (light blue). **c)** When the drive tone matches one of the fluxonium transitions, one observes a peak in the transmission of the readout tone.

The drive tone can be varied over a large frequency range. However, since it arrives to the qubit through the resonator, which attenuates signals away from its resonance frequency, it can be that drive powers much larger than the readout power are needed to excite the qubit. Figure 3.7 shows a two-tone measurement at fixed gate and external flux. The frequency readout tone is fixed at the bottom of the resonance when the system is not being excited, shown in figure 3.7 a). Panel b) shows the resulting peak in readout transmission versus qubit drive tone. As mentioned, the power needed to observe the resonator resonance is much lower than the one needed to excite the two-tone transition.

3.3.1 E_J and external flux dependence

Observing a peak in two-tone does not automatically mean that a fluxonium transition is being excited. It could be, for example, that some other multilevel system, with a transition at that specific frequency, is coupled to the resonator. In order to make sure that the observed peak comes from a fluxonium transition we can check whether it responds to the different knobs available for tuning the spectrum: cutter gate voltage and external flux.

Figure 3.8 shows this dependence for two different peaks observed in two-tone spectroscopy. The change in intensity in the background of panel a) is due to a shift

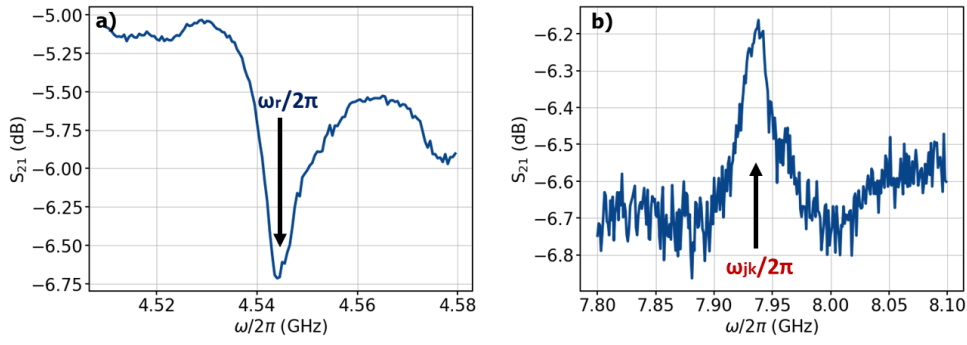


FIGURE 3.7: **Two-tone trace versus drive frequency.** Panel a) shows the resonator at equilibrium. The readout frequency is fixed at $\omega_r/2\pi = 4.544$ GHz and a peak is observed if the system is driven at $\omega/2\pi = 7.94$ GHz with a second tone, shown in panel b). Readout and drive powers are -60 dBm and -20 dBm, respectively.

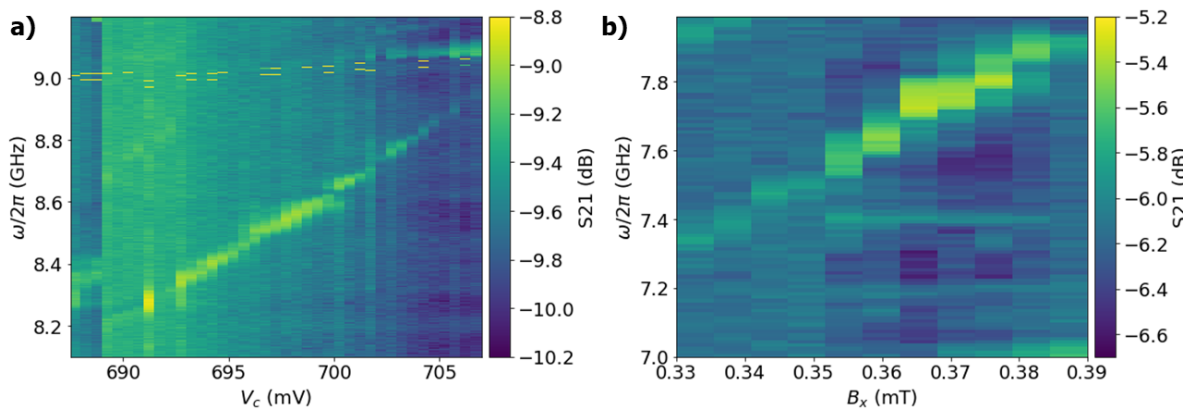


FIGURE 3.8: **Two-tone trace versus drive frequency and cutter voltage or flux.** a) Cutter gate dependence of a peak observed in two-tone spectroscopy. Color scale is in dB. b) External flux dependence of a two-tone peak. Color scale is linear.

in position of the bottom of the resonance with cutter. In order to avoid this effect in the spectra shown in the next section, which is expected to be larger because they are taken over a larger flux range, the readout frequency is updated at every different flux and cutter point.

3.3.2 Spectra at different E_J values

Combining the two available knobs for tuning the energy spectrum, we can obtain spectra over a full Φ_{ext} and at different E_J values. Figures 3.9, 3.10 and 3.11 show three different spectra taken at different cutter gate values. Each two-tone measurement is compared with an overlapped spectrum obtained by diagonalization of the coupled Hamiltonian following the method in reference [78]. All overlapped spectra share the same E_C and E_L values, since they are fixed by design, and only E_J is allowed to vary. For the fits we use $E_C/h = 2.4$ GHz, $E_L/h = 0.7$ GHz and a shared inductance that is 20% of the resonator inductance. It is worth mentioning that this is a very constrained fitting problem, since we are fitting several flux dependent transitions with a single free parameter E_J .

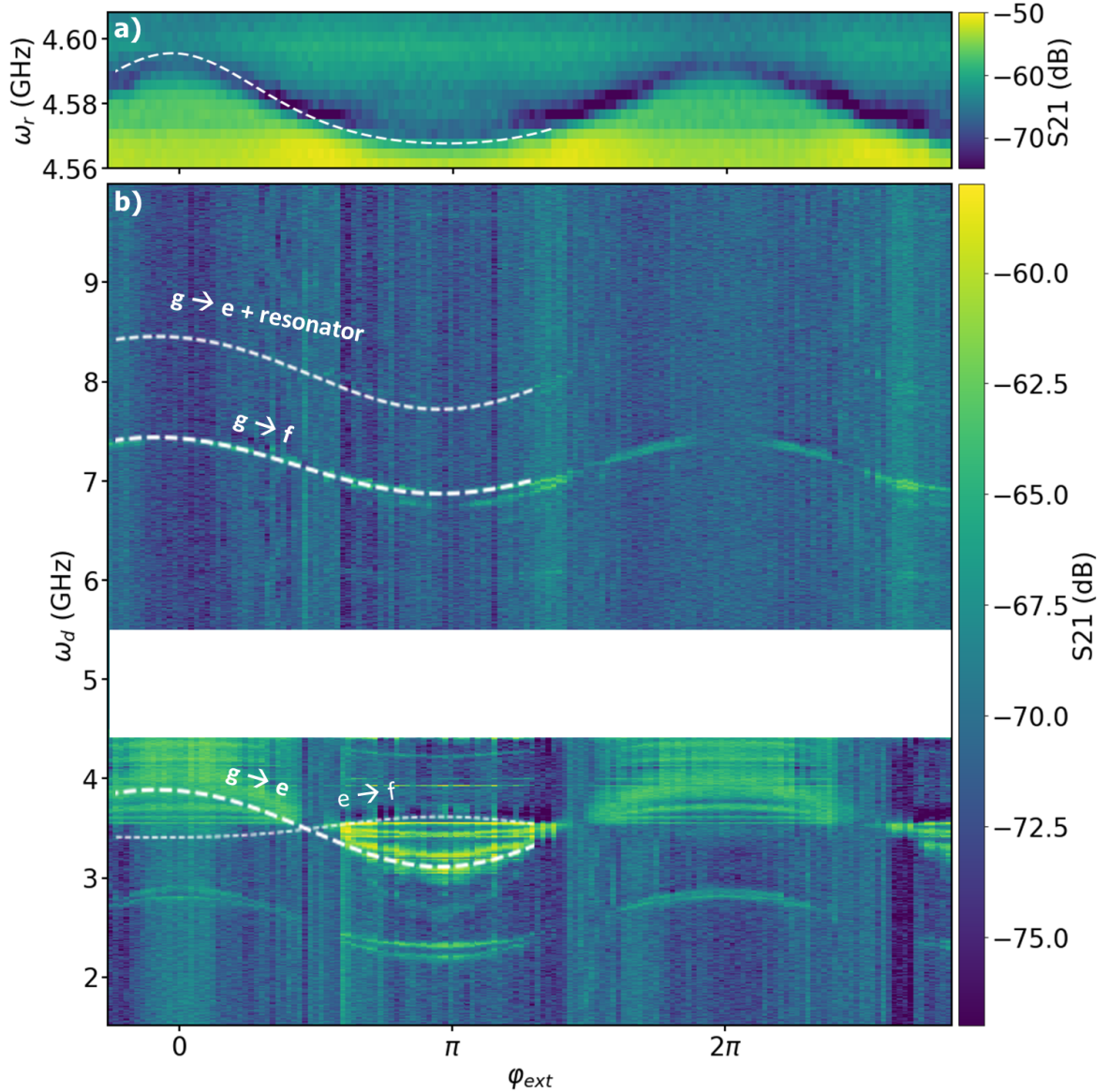


FIGURE 3.9: **Spectrum at $V_c = 447$ mV.** a) S_{21} measurement vs readout frequency and flux showing the dispersive shift on the resonator. b) Two-tone signal versus drive frequency and flux. Readout frequency is the minimum of the resonator resonance for each external flux point. Overlapped white lines indicate transition frequencies for the inductively coupled system with $E_C/h = 2.4$ GHz, $E_L/h = 0.7$ GHz and $E_J/h = 0.58$ GHz. Suppression of the $|g\rangle \rightarrow |f\rangle$ transition can be observed around zero and half-flux.

Figure 3.9 shows the fitted spectrum for $E_J/h = 0.7$ GHz. Transitions $|g\rangle \rightarrow |e\rangle$ and $|g\rangle \rightarrow |f\rangle$ match satisfactorily two flux-dependent lines in the spectrum. However, the line appearing at around 2.5 GHz is not fitted properly with this spectrum. As expected, we observe holes in the visibility of the $|g\rangle \rightarrow |e\rangle$ at integer multiples of half-flux, agreeing with the forbidden transition due to the even parity of the states involved (explained in section 1.2.3). This can also be clearly seen in figure 3.10.

Specially in figure 3.10, but also in 3.11 we can observe a transition appearing as an inverted peak only visible at around half-flux, similar to the observations in reference [79]. We interpret this spectroscopy line as the $|e\rangle \rightarrow |f\rangle$ transition. For high E_J values the frequency minimum reached by $|g\rangle \rightarrow |e\rangle$ at around $\Phi_{\text{ext}} = \Phi_0/2$ can

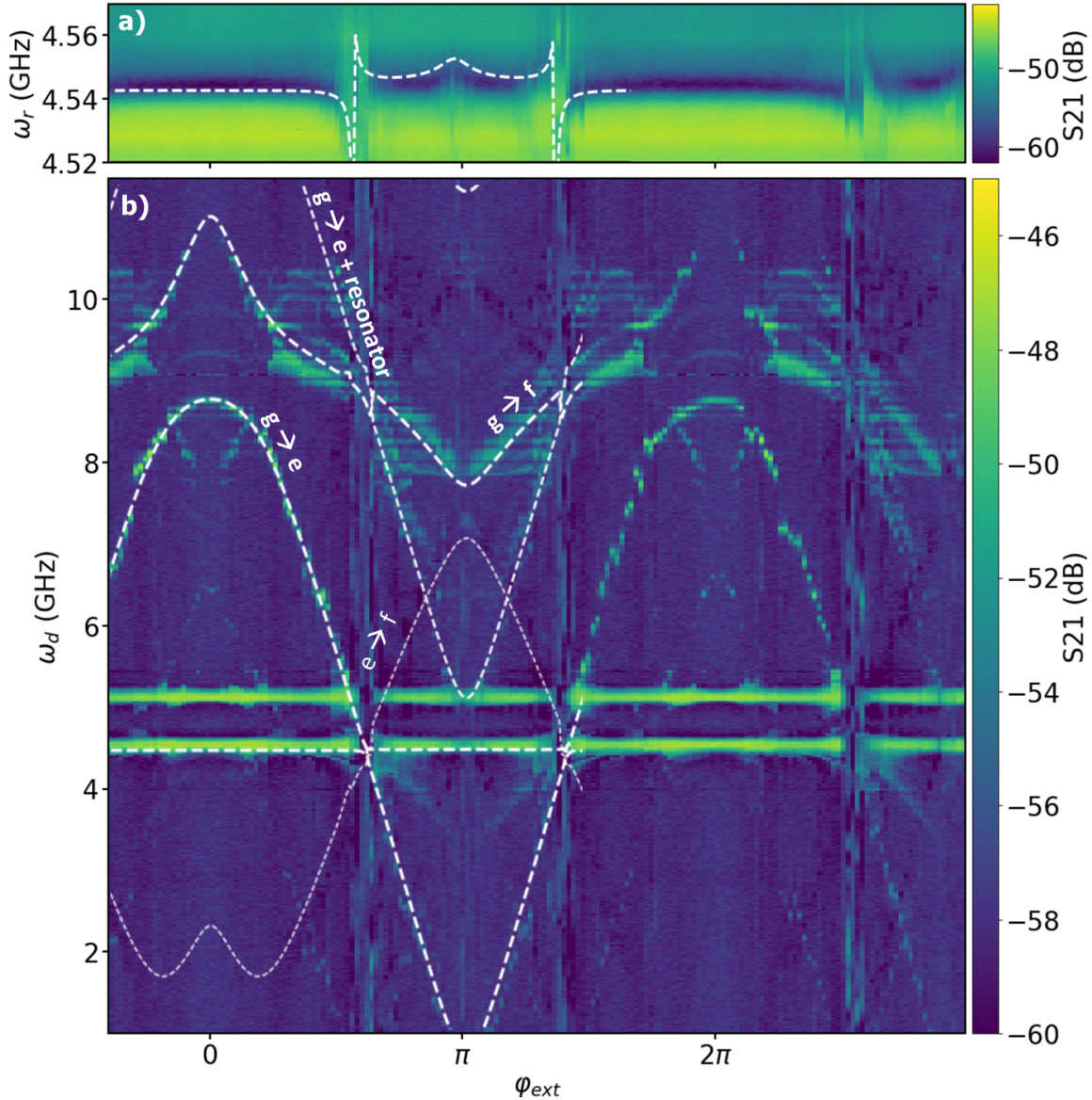


FIGURE 3.10: **Spectrum at $V_c = 871$ mV.** Same as figure 3.9 but now with $E_J/h = 6.9$ GHz. Transition $|e\rangle \rightarrow |f\rangle$ is now visible due to the thermal population of the $|e\rangle$ state around half-flux.

be below $\omega_{ge}/2\pi = 1$ MHz. For a typical temperature of 50 mK, with a characteristic energy $K_B T/h = 1$ MHz the occupation of the $|e\rangle$ state starts being noticeable at equilibrium. The observation of this transition in a small window around zero flux gives therefore an estimate for the electron temperature of around 50 mK.

Overlapping spectra with different E_J

An interesting effect observed in several spectroscopy measurements for this device is a doubling of some of the lines, resulting in a superposition of two spectra corresponding to the same E_C and E_L , but with a different E_J . This effect can be seen in figure 3.12, in which both the dispersive shift on the resonator and the two-tone data can be fitted with two different E_J values, indicated with different colors. The origin of the superimposed spectra may be oscillations of the value of E_J in a timescale

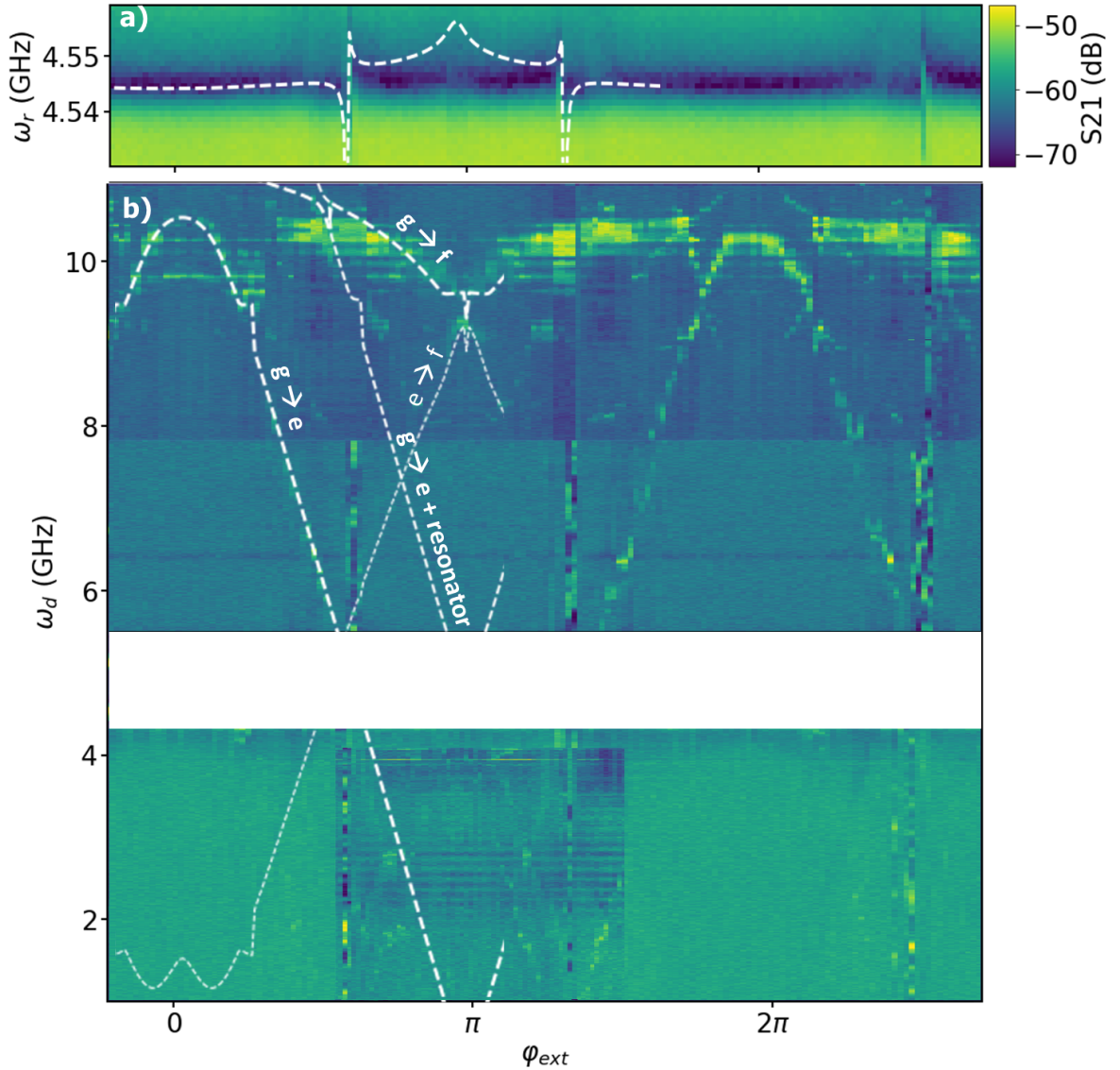


FIGURE 3.11: **Spectrum at $V_c = 1032$ mV.** Same as figure 3.9 but now with $E_J/h = 9.0$ GHz. Visibility of the $|g\rangle \rightarrow |e\rangle$ transition is lower than for lower E_J values. This is due to the large detuning of the $|g\rangle \rightarrow |f\rangle$ transition from the readout resonator.

faster than the measurement time. One possible reason for this is an electrostatic impurity close to the junction with an unstable charge. This would cause electrostatic instability at the junction, resulting in different effective gate potentials corresponding to different E_J values. A second explanation is the change of parity of one of the Andreev bound states at the junction. If an ABS state is excited, the value of E_J will change, as we saw in section 1.3. If the transmission of the ABS is large, this can result in a noticeable effect in the measured spectra. If this is the case, we can study the temporal dynamics of quasiparticle poisoning of ABSs by doing time domain measurements in the double spectroscopy lines. This will be discussed in the outlook of this work.

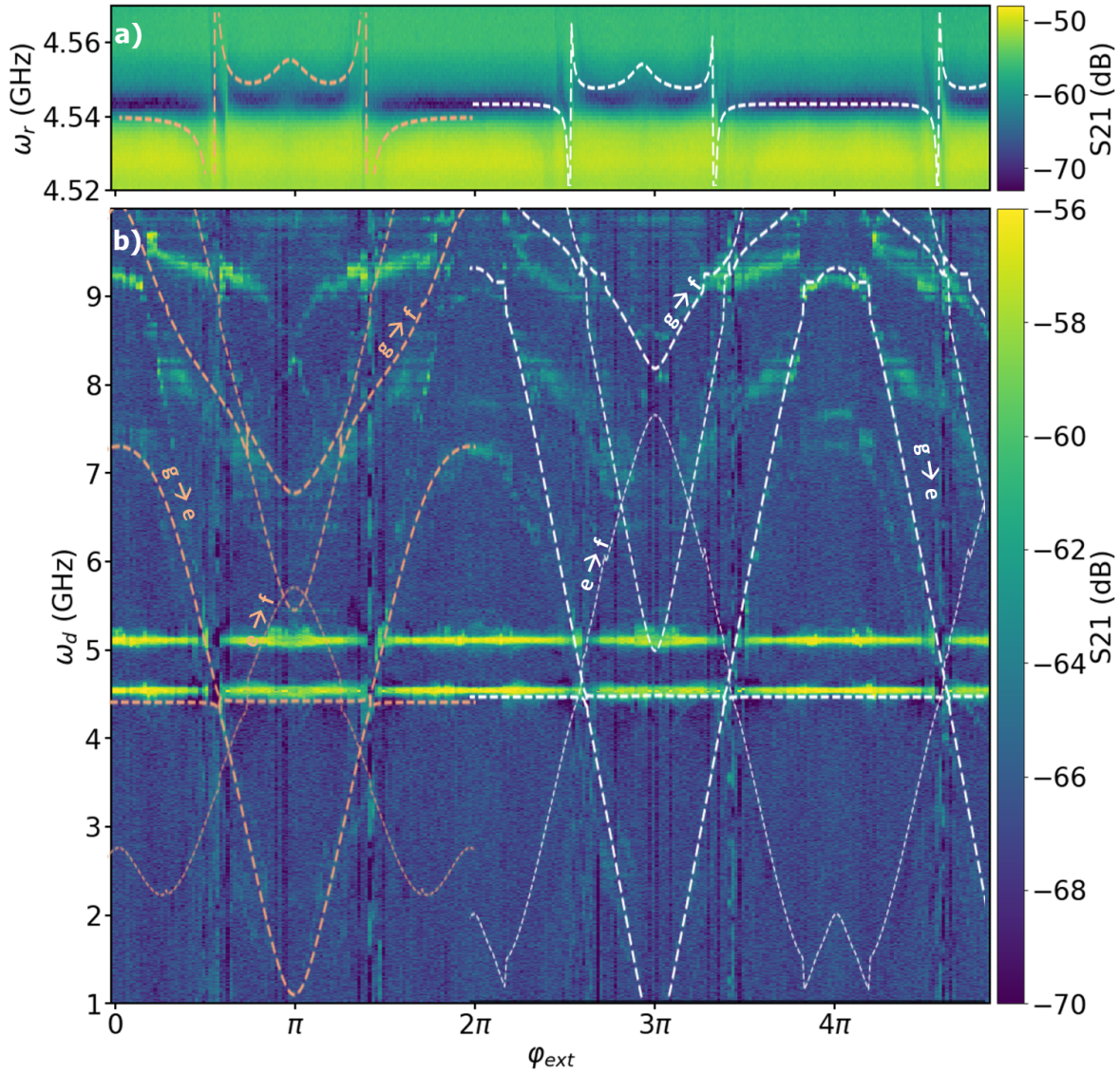


FIGURE 3.12: **Spectrum at $V_c = 650$ mV.** Two overlapping spectra corresponding to different E_J values are observed. White fitting lines correspond to $E_J/h = 7.3$ GHz and orange lines correspond to $E_J/h = 5.0$ GHz. In both cases $E_C/h = 2.4$ GHz and $E_L/h = 0.7$ GHz.

Mapping E_J vs. cutter gate

Maintaining the flux fixed and measuring the two-tone transmission versus drive frequency and cutter gate voltage V_c is an interesting measurement to study the dependence of E_J on V_c . This is shown in figure 3.13 for $\Phi_{\text{ext}} = 0$. For fixed $E_C/h = 2.4$ GHz and $E_L/h = 0.7$ GHz, the frequency of the $|g\rangle \rightarrow |e\rangle$ transition increases monotonically with E_J , so one can map the measured transitions to their corresponding E_J values. Figure 3.13 shows a non-monotonic increase of E_J with cutter, which agrees with the trend observed in previous supercurrent and spectroscopy experiments (see figure 1.15).

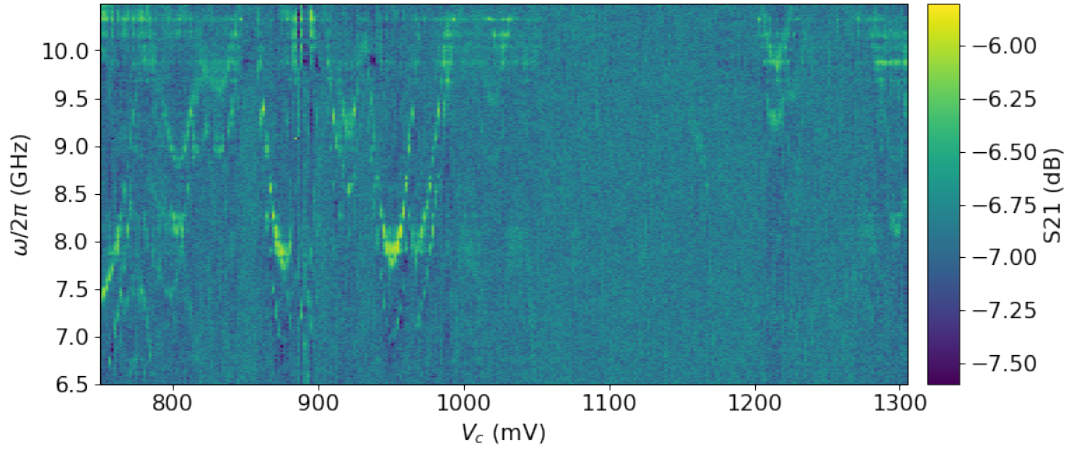


FIGURE 3.13: **Two-tone spectroscopy versus drive frequency and cutter gate.** Oscillations of the frequencies of the lowest energy transitions at $\Phi_{\text{ext}} = 0$ are observed, as expected.

3.4 In-plane magnetic field compatibility

In-plane magnetic fields of the order of 1 T are needed to enter the topological regime [21], [40]. For this reason, our device performance should be resilient up to at least these magnetic fields. Measurements presented in this section are carried out at in-plane fields with some degrees of missalignment with respect to the wire direction.

3.4.1 Spectroscopy measurements up to 300 mT

Two-tone spectra like the ones presented in the previous section were measured at fields up to 300 mT. Two examples are shown in figure 3.14.

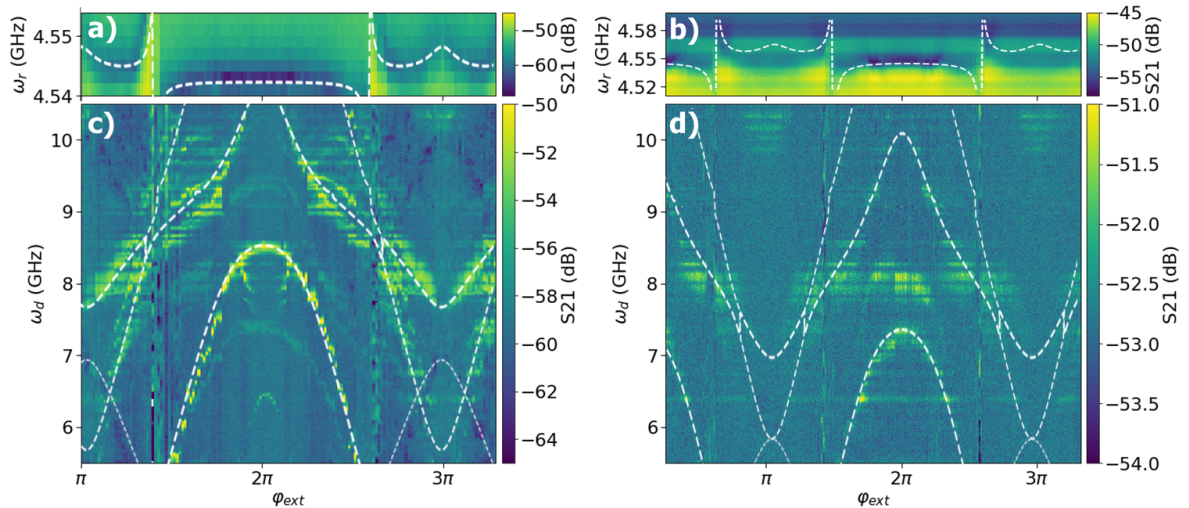


FIGURE 3.14: **Spectra at non-zero in-plane magnetic field.** **a)** Spectrum taken at $B = 185$ mT and $V_c = 940$ mV. Overlapped transitions correspond to a system with $E_J/h = 6.1$ GHz. **b)** Spectrum taken at $B = 300$ mT and $V_c = 1260$ mV. $E_J/h = 4.7$ GHz in this case. E_L and E_C are the same as for previous fits.

E_J is found to decrease strongly with field, agreeing with the supercurrent decrease with field observed in reference [86]. This effect prevents entering the fluxonium parameter regime at large fields. In the outlook section we will see how the design could be changed to account for this decrease in E_J and be able to stay in the fluxonium regime up to higher field values.

Measurements similar to the ones realized at zero field to map out E_J versus cutter can also be done at non-zero field. Figure 3.15 shows an example of this. The trend observed is similar to the one in figure 3.13.

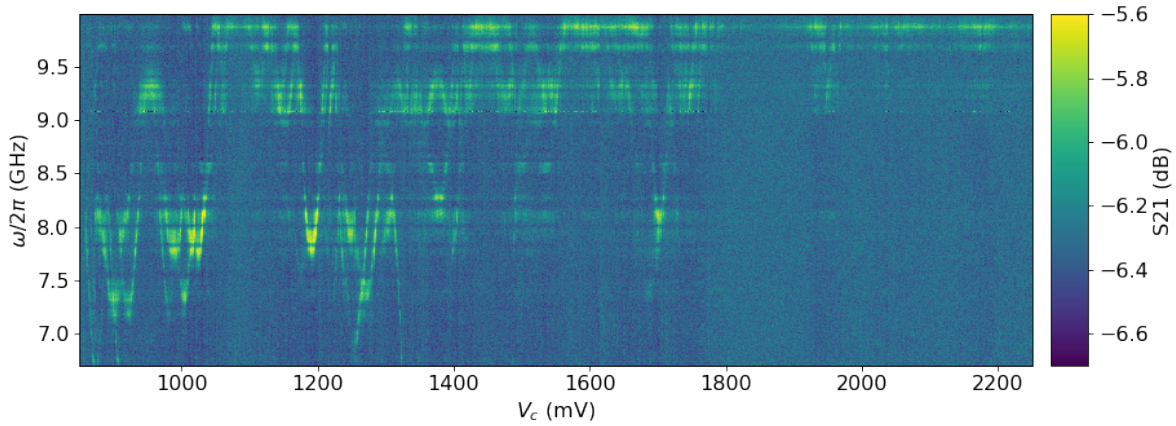


FIGURE 3.15: **Two-tone spectroscopy versus drive frequency and cutter gate at 300 mT in-plane.** Same as figure 3.13 but now at non-zero in-plane magnetic field.

3.4.2 Resonator compatibility at higher fields

What made it more complicated for this device to obtain clear spectroscopy data at high fields was a broadening of the readout resonator peak.

Figure 3.16 shows an example of this effect. For low magnetic fields (panels a) and b)) the resonator resonance stabilizes at around 4.54 GHz at high cutters and has a depth similar to the one at zero cutter. Maintaining the readout tone at the bottom of this resonance, one can carry out two-tone spectroscopy measurements (as shown in figure 3.14). As the in-plane field is increased, the avoided crossings at intermediate cutters are still observed (panels c)-e)). However, the readout resonance at large cutters becomes blurry and less deep. For this reason spectra could not be taken at larger fields for this specific device, even if the avoided crossings indicate that the fluxonium is still resilient and cutter-tunable up to at least 800 mT. This broadening may be related to the observed decrease in E_J , due to an stabilization of the spectral lines closer to the resonator when E_J is low. A change in the device design that allows staying in the fluxonium regime up to higher magnetic fields could help decreasing this unwanted effect. For larger fields, the avoided crossings are not observed anymore due to the low value of E_J (panel f)). We should however note that the position of the resonance at zero cutter does not change or become much worse in the range of fields studied. This indicates that the lumped element resonators used for readout are resilient to fields of the order of the ones needed to enter the topological regime. If the fluxonium design is changed to compensate the low values of E_J in field, spectroscopy could be done up to larger fields. We plan to do this

for future devices.

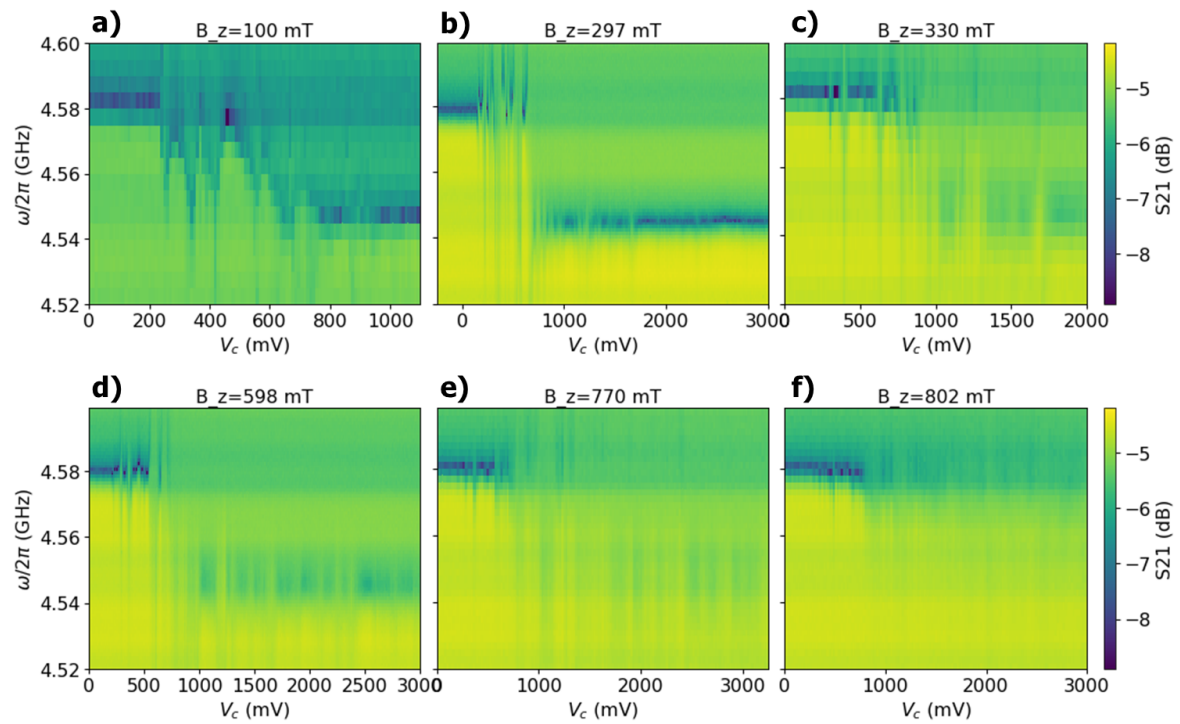


FIGURE 3.16: **Resonator compatibility at high in-plane fields a)-f)** S_{21} measurements of the resonator versus cutter at increasing in-plane fields, indicated in the title for each panel.

Conclusion and outlook

The work presented in this thesis includes the design, fabrication and initial characterization of a Majorana fluxonium in the trivial regime. It has been shown that all relevant parameters of the model for this device can be experimentally controlled. The values of E_C and E_L are fixed by design, while the external flux, the Josephson energy, the chemical potential in the topological sections and the external in-plane magnetic field can be tuned *in situ* and independently.

The main characterization measurements that have been carried out are the two-tone spectra in the whole Φ_{ext} range, both at zero field and in the presence of an in-plane field. The next step in characterization of the trivial device will be the measurement of coherence times of the different states. By studying the dependence of T_1 and T_2^* on E_J , Φ_{ext} and B , we will be able to study different sources of decoherence and try to adapt the design and measurement conditions to minimize their effect.

The main purpose of the development of this device is the study of topological effects of MZMs coupled at both sides of the junction. This will be the main focus of the future experiments in this device. It is possible, however, to realize interesting non-topological experiments in this platform, which will also be briefly introduced here.

Search for Majorana signatures

The main motivations of this project are the study a junction between two topological segments and the realization of a qubit with topologically protected states. Next steps are therefore going to be taken in this direction.

MZMs signatures are detectable with standard cQED techniques, by sitting at a fixed point in external flux and cutter voltage and monitoring a transition in the spectrum while the plunger gate voltages are varied. If the chemical potentials are such that a topological phase appears at both superconducting sections of the nanowire, a splitting of the first transition line will be observed. The magnitude of this splitting will be proportional to the inner Majorana coupling E_M , so observing such splitting would directly provide new information on the physics of MZMs. Apart from the doubling of a spectral line, a second clear signature of both sections entering the topological regime would be the observation of a shift in the flux sweet spot of the $|g\rangle \rightarrow |e\rangle$ fluxonium transition. Once one of these signatures is locally detected, one could take a whole spectrum versus Φ_{ext} and drive frequency and, by fitting it, extract the values of E_M , E_M^{01} and E_M^{23} . The former determines the magnitude of the shift and the two latter determine the magnitude of the gaps at the anticrossings.

However, the observation of these effects is not expected to be easy. It is already challenging to tune a single section of wire into the topological regime (as shown in references [44], [45]). Having two independent plungers to tune two different sections doubles the dimensionality of the space in which we will need to look for topological signatures. A non-realistic-at-this-stage solution for this problem would

be the incorporation of DC contacts at the end of the wires. This would permit the detection of a topological transition in each of the sections independently, using DC techniques, reducing the search space enormously. This would also be interesting for correlating DC signatures of Majoranas with the signatures coming from this experiment, giving stronger evidence of the topological origin of the observed effects. It would however be extremely challenging to incorporate these DC elements in this device, and due to their effect on the electrostatic environment they would detriment the performance of the device in RF. Four extra cutters would be necessary to pinch off the wire and effectively remove either the DC connection or the loop connection. The wire should also split in two sections at its ends, something that would be easier to realize in a SAG platform [107]. The correlation of DC and RF signatures is left as a long term goal for the moment when the device is controlled better and when material platforms are developed further.

Apart from the characterization of energy scales associated with MZMs, we intend to realize single-qubit quantum operations both on the topological qubit and on the fluxonium qubit, and also the two-qubit SWAP and cNOT operations. A first step in this direction will be the realization of gates in the trivial fluxonium at zero field and the characterization of their fidelity. More complex gates are a long term goal which requires the detection of topological signatures first.

Alternative materials and possible design changes

In parallel to the realization of physics experiments in the platform developed in this work, we plan to realize some design changes, explore new materials and continuously adapt the device design to the requirements learned from new measurements.

As discussed by the end of chapter 3, the decrease of E_J with field should be kept in mind when designing for specific E_J/E_C and E_J/E_L ratios. As we saw, the reduced value of E_J in field did not permit maintaining the fluxonium transitions at high frequencies when increasing B . For this reason, we plan to increase the size of the parallel plate capacitor for future devices, reducing therefore the fixed value of E_C (see equation 2.8).

Further design changes that could be considered in the future are the incorporation of air bridges and qubit drive lines. Air bridges connect the different pieces of ground plane together with a material resilient to large magnetic fields, what would avoid the potential problems arising from the thick aluminum wires used currently, that can lose superconductivity when increasing the field. Using extra lines to drive the qubit would allow to experimentally separate the lines used for addressing the qubit and for readout, avoiding having to send signals through the resonator to excite the fluxonium transitions.

Regarding alternative materials, a first possibility, which was discussed in detail in chapter 1, is the use of InSb nanowires instead of InAs ones. Their larger g -factor and shadowed junctions make them a more promising material for the detection of topological signatures at the junction. The next generation of devices will include devices with some design changes adapted for this material platform. Since InSb VLS nanowires are typically shorter than InAs ones, contacts must be brought closer together. Furthermore, due to the fixed position of the shadow junction in these

wires, it is not possible to deterministically place them aligned to a pre-patterned cutter gate. For this reason, future InSb devices will have a global gate that controls the electrostatic potential of the whole wire and wrapped gates deposited in a later step to independently control the plunger and cutter potentials.

Other interesting materials to explore are different superconductors with a high kinetic inductance. ALD TiN, for example, offers some advantages with respect to the currently used sputtered NbTiN [95]. ALD deposition times are normally controlled automatically, while the sputtering time in the current fabrication process is controlled by the user. The current variation of film parameters between different depositions would decrease in the case of ALD, making the device fabrication more systematic and its performance easier to predict. Another property of ALD deposition is the homogeneity of the resulting film thickness across the wafer. The kinetic inductance and T_C of current devices depend strongly on the location of the chip in the original wafer, with a bigger film-thickness for chips coming from the center of the wafer than for devices coming from close to its edge. The L_k values corresponding to a given film thickness are also larger for TiN than for NbTiN, reported to be larger than $200 \text{ pH}/\square$ for a 9 nm-thick ALD TiN film in reference [95].

Other experiments on the Majorana fluxonium platform

Apart from pursuing the main objective of studying the behaviour of a Majorana fluxonium in the topological regime, different experiments that do not require any topological effect can be realized in parallel.

There is still a lot to understand about the physics of Josephson junctions in semiconducting materials, specially in the presence of spin-orbit coupling and Zeeman effects. With a Majorana fluxonium we can study the gate and field dependence of the current-phase relation of a semiconducting junction, both at zero field and in the presence of a magnetic field, contributing to the understanding of the physics of Andreev bound states.

Due to the observation of superimposed spectra corresponding to different E_J 's, it would also be possible to study the dynamics of quasiparticle poisoning of ABSs. Large quasiparticle poisoning times at the junction are needed to realize topological qubits with large coherence times. Studying the dependence of the poisoning rates on different parameters would allow to minimize decoherence sources in this and other topological qubits. This type of doubling of the spectral lines can also be useful to study the number of high transmission channels at the junction, increasing the input power one can excite the different channels and count them based on the number of lines appearing in the spectrum. A reduced number of channels at the junction is preferred to study topological signatures in a Majorana fluxonium, since all channels contribute to the E_J term, while only a single channel contributes to the E_M coupling strength. Characterizing the dependence of the ABS channels on gate and field would therefore contribute to a better understanding of the nanowire fluxonium device and to the characterization of its optimum operational points.

Acknowledgements

The work presented in this thesis has been possible thanks to the combination of a perfect research environment, the support from brilliant people and an extraordinary guidance.

Angela has been the most exceptional supervisor I could imagine, full of knowledge, patience and positivity. You've thought about every detail of the nanowire fluxonium project and always have an answer ready for any question about it, from its physics, to its design, fabrication, simulation or measurements. Thanks for having been incredibly patient explaining in detail everything that I asked, often more than once. And thanks for not having lost your nerves when I didn't understand obvious things, when I destroyed devices or when I took forever tightening screws. Don't worry, I'll give you more chances.

Leo, you have given me the opportunity of working in one of the most excellent groups in the world. I really appreciate your support, your leadership and your dedication for maintaining and improving the amazing research environment, resources and excellence we are surrounded with.

I'm also grateful for the help, support and useful discussions with Gijs, Wolfgang, CK and David. It's great to have you around.

Topo-cQED team, Arno, Willemijn, James, Jouri, Vukan, the perfect combination of dedication and good vibes at our battle station. Arno, always available for discussions and ready to help. Willemijn, the most hard working person inside the cleanroom and the most enthusiastic outside of it. I've learned a lot from you.

Pulse?

Thanks also to the rest of the Topo group for all the fun moments and for providing a great research environment. I can't imagine a better work atmosphere than the one here at QuTech. These past months have been great thanks to the various QuTech activities and events.

I would probably had gone crazy in a world of Majoranas, ebeams and blue cables if it hadn't been for the h-bar people. Hugo, Boris, Eugenio, Mattias, Chian, Christian, Hélène, Santi, Ivan, Alina, Kat and Michail, thanks for forcing me to forget about the lab every now and then and for reminding me about the outside world. You are amazing.

Gracias también a mis amigos y familia. Óscar, gracias por aguantar tantas horas de Skype y por escuchar mis historias sobre gente extraña. Manuela, Alberto, ma, pa, gracias por vuestro apoyo. Vinisteis a Delft más veces de lo que habría podido imaginar. Hacéis que parezca más cerca.

Bibliography

- [1] M. A. Nielsen and I. L. Chuang, “Quantum computation and quantum information, 10th anniversary edition”, *Cambridge University Press*, 2010.
- [2] L. K. Grover, “A fast quantum mechanical algorithm for database search”, *ArXiv: ArXiv:quant-ph/9605043*, 1996. [Online]. Available: <https://arxiv.org/abs/quant-ph/9605043>.
- [3] P. Shor, “Polynomial-time algorithms for prime factorization and discrete logarithms on a quantum computer”, *SIAM J.Sci.Statist.Comput*, vol. 41(2), 303–332, 1997. DOI: [10.1137/S0097539795293172](https://doi.org/10.1137/S0097539795293172).
- [4] C. H. Bennett and G. Brassard, “Quantum cryptography: Public key distribution and coin tossing”, *Proceedings of the International Conference on Computers, Systems and Signal Processing*, 175–179, 1984. DOI: [10.1016/j.tcs.2014.05.025](https://doi.org/10.1016/j.tcs.2014.05.025).
- [5] R. P. Feynman, “Simulating physics with computers”, *International Journal of Theoretical Physics*, vol. 21, no. 6-7, pp. 467–488, 1982. DOI: [10.1007/BF02650179](https://doi.org/10.1007/BF02650179).
- [6] I. Kassal, J. D. Whitfield, A. Perdomo-Ortiz, M.-H. Yung, and A. Aspuru-Guzik, “Simulating chemistry using quantum computers”, *Annual Review of Physical Chemistry*, vol. 62, no. 1, pp. 185–207, 2011. DOI: [10.1146/annurev-physchem-032210-103512](https://doi.org/10.1146/annurev-physchem-032210-103512).
- [7] C. Nayak, S. H. Simon, A. Stern, M. Freedman, and S. Das Sarma, “Non-abelian anyons and topological quantum computation”, *Rev. Mod. Phys.*, vol. 80, pp. 1083–1159, 3 2008. DOI: [10.1103/RevModPhys.80.1083](https://doi.org/10.1103/RevModPhys.80.1083).
- [8] A. Kitaev, “Fault-tolerant quantum computation by anyons”, *Annals of Physics*, vol. 303, no. 1, pp. 2–30, 2003, ISSN: 0003-4916. DOI: [10.1016/S0003-4916\(02\)00018-0](https://doi.org/10.1016/S0003-4916(02)00018-0).
- [9] A. Y. Kitaev, “Unpaired majorana fermions in quantum wires”, *Physics-Uspekhi*, vol. 44, no. 10S, p. 131, 2001. [Online]. Available: <http://stacks.iop.org/1063-7869/44/i=10S/a=S29>.
- [10] V. E. Manucharyan, J. Koch, L. I. Glazman, and M. H. Devoret, “Fluxonium: Single cooper-pair circuit free of charge offsets”, *Science*, vol. 326, no. 5949, pp. 113–116, 2009, ISSN: 0036-8075. DOI: [10.1126/science.1175552](https://doi.org/10.1126/science.1175552).
- [11] E. Majorana, “Teoria simmetrica dell’elettrone e del positrone”, *Il Nuovo Cimento*, vol. 14, no. 4, p. 171, 1937. DOI: [10.1007/BF02961314](https://doi.org/10.1007/BF02961314).
- [12] F. Wilczek, “Majorana returns”, *Nature Physics*, vol. 5, 614 EP –, 2009, Perspective. DOI: [10.1038/nphys1380](https://doi.org/10.1038/nphys1380).
- [13] A. Stern, “Non-abelian states of matter”, *Nature*, vol. 464, 187 EP –, 2010. DOI: [10.1038/nature08915](https://doi.org/10.1038/nature08915).
- [14] P. W. Brouwer, “Enter the majorana fermion”, *Science*, vol. 336, no. 6084, pp. 989–990, 2012, ISSN: 0036-8075. DOI: [10.1126/science.1223302](https://doi.org/10.1126/science.1223302).

- [15] P. A. Lee, "Seeking out majorana under the microscope", vol. 346, no. 6209, pp. 545–546, 2014, ISSN: 0036-8075. DOI: [10.1126/science.1260282](https://doi.org/10.1126/science.1260282).
- [16] F. von Oppen, Y. Peng, and F. Pientka, "Topological superconducting phases in one dimension", *Lecture Notes of the École de Physique des Hautes Summer School: Topological aspects of condensed matter physics*, 2014. [Online]. Available: http://topo-houches.pks.mpg.de/wp-content/uploads/2015/09/lecture_Oppen.pdf.
- [17] R. M. Lutchyn, E. P.A. M. Bakkers, L. P. Kouwenhoven, P. Krogstrup, C. M. Marcus, and Y. Oreg, "Majorana zero modes in superconductor-semiconductor heterostructures", *Nature Reviews Materials*, vol. 3, no. 5, pp. 52–68, 2018. DOI: [10.1038/s41578-018-0003-1](https://doi.org/10.1038/s41578-018-0003-1).
- [18] G. Moore and N. Read, "Nonabelions in the fractional quantum hall effect", *Nuclear Physics B*, vol. 360, no. 2, pp. 362–396, 1991. DOI: [10.1016/0550-3213\(91\)90407-0](https://doi.org/10.1016/0550-3213(91)90407-0).
- [19] R. M. Lutchyn, J. D. Sau, and S. Das Sarma, "Majorana fermions and a topological phase transition in semiconductor-superconductor heterostructures", *Phys. Rev. Lett.*, vol. 105, p. 077001, 7 2010. DOI: [10.1103/PhysRevLett.105.077001](https://doi.org/10.1103/PhysRevLett.105.077001).
- [20] Y. Oreg, G. Refael, and F. von Oppen, "Helical liquids and majorana bound states in quantum wires", *Phys. Rev. Lett.*, vol. 105, p. 177002, 17 2010. DOI: [10.1103/PhysRevLett.105.177002](https://doi.org/10.1103/PhysRevLett.105.177002).
- [21] V. Mourik, K. Zuo, S. M. Frolov, S. R. Plissard, E. P.A. M. Bakkers, and L. P. Kouwenhoven, "Signatures of majorana fermions in hybrid superconductor-semiconductor nanowire devices", *Science*, vol. 336, no. 6084, pp. 1003–1007, 2012, ISSN: 0036-8075. DOI: [10.1126/science.1222360](https://doi.org/10.1126/science.1222360).
- [22] Y. V. Nazarov and D. Jeroen, "Advanced quantum mechanics: A practical guide", *Cambridge University Press*, 2013. DOI: [10.1017/CB09780511980428](https://doi.org/10.1017/CB09780511980428).
- [23] A. Akhmerov, J. Sau, B. van Heck, B. Nijholt, I. Muhammad, and T. Rosdahl. (). Topology in condensed matter, [Online]. Available: <https://topocondmat.org/> (visited on 12/29/2018).
- [24] D. A. Ivanov, "Non-abelian statistics of half-quantum vortices in p -wave superconductors", *Phys. Rev. Lett.*, vol. 86, pp. 268–271, 2 2001. DOI: [10.1103/PhysRevLett.86.268](https://doi.org/10.1103/PhysRevLett.86.268).
- [25] J. Alicea, Y. Oreg, G. Refael, F. von Oppen, and M. P. A. Fisher, "Non-abelian statistics and topological quantum information processing in 1d wire networks", *Nature Physics*, vol. 7, 412 EP–, 2011, Article. DOI: [10.1038/nphys1915](https://doi.org/10.1038/nphys1915).
- [26] J. D. Sau, D. J. Clarke, and S. Tewari, "Controlling non-abelian statistics of majorana fermions in semiconductor nanowires", *Phys. Rev. B*, vol. 84, p. 094505, 9 2011. DOI: [10.1103/PhysRevB.84.094505](https://doi.org/10.1103/PhysRevB.84.094505).
- [27] B van Heck, A. R. Akhmerov, F Hassler, M Burrello, and C. W. J. Beenakker, "Coulomb-assisted braiding of majorana fermions in a josephson junction array", *New Journal of Physics*, vol. 14, no. 3, p. 035019, 2012. [Online]. Available: <http://stacks.iop.org/1367-2630/14/i=3/a=035019>.
- [28] F. Hassler, A. R. Akhmerov, C.-Y. Hou, and C. W. J. Beenakker, "Anyonic interferometry without anyons: How a flux qubit can read out a topological qubit", *New Journal of Physics*, vol. 12, no. 12, p. 125002, 2010. DOI: [10.1088/1367-2630/12/12/125002](https://doi.org/10.1088/1367-2630/12/12/125002).

- [29] F Hassler, A. R. Akhmerov, and C. W. J. Beenakker, "The top-transmon: A hybrid superconducting qubit for parity-protected quantum computation", *New Journal of Physics*, vol. 13, no. 9, p. 095004, 2011. [Online]. Available: <http://stacks.iop.org/1367-2630/13/i=9/a=095004>.
- [30] D. Pekker, C.-Y. Hou, V. E. Manucharyan, and E. Demler, "Proposal for coherent coupling of majorana zero modes and superconducting qubits using the 4π josephson effect", *Phys. Rev. Lett.*, vol. 111, p. 107007, 10 2013. DOI: 10.1103/PhysRevLett.111.107007.
- [31] D. Aasen, M. Hell, R. V. Mishmash, A. Higginbotham, J. Danon, M. Leijnse, T. S. Jespersen, J. A. Folk, C. M. Marcus, K. Flensberg, and J. Alicea, "Milestones toward majorana-based quantum computing", *Phys. Rev. X*, vol. 6, p. 031016, 3 2016. DOI: 10.1103/PhysRevX.6.031016.
- [32] S. Plugge, A. Rasmussen, R. Egger, and K. Flensberg, "Majorana box qubits", *New Journal of Physics*, vol. 19, no. 1, p. 012001, 2017. [Online]. Available: <http://stacks.iop.org/1367-2630/19/i=1/a=012001>.
- [33] T. Karzig, C. Knapp, R. M. Lutchyn, P. Bonderson, M. B. Hastings, C. Nayak, J. Alicea, K. Flensberg, S. Plugge, Y. Oreg, C. M. Marcus, and M. H. Freedman, "Scalable designs for quasiparticle-poisoning-protected topological quantum computation with majorana zero modes", *Phys. Rev. B*, vol. 95, p. 235305, 23 2017. DOI: 10.1103/PhysRevB.95.235305.
- [34] Y.-J. Doh, J. A. van Dam, A. L. Roest, E. P.A. M. Bakkers, L. P. Kouwenhoven, and S. De Franceschi, "Tunable supercurrent through semiconductor nanowires", *Science*, vol. 309, no. 5732, pp. 272–275, 2005. DOI: 10.1126/science.1113523.
- [35] J. A. van Dam, Y. V. Nazarov, E. P.A. M. Bakkers, S. De Franceschi, and L. P. Kouwenhoven, "Supercurrent reversal in quantum dots", *Nature*, vol. 442, 667 EP –, 2006. DOI: 10.1038/nature05018.
- [36] A. Das, Y. Ronen, Y. Most, Y. Oreg, M. Heiblum, and H. Shtrikman, "Zero-bias peaks and splitting in an al-inas nanowire topological superconductor as a signature of majorana fermions", *Nature Physics*, vol. 8, 887 EP –, 2012, Article. DOI: 10.1038/nphys2479.
- [37] P. Krogstrup, N. L. B. Ziino, W. Chang, S. M. Albrecht, M. H. Madsen, E. Johnson, J. Nygård, C. M. Marcus, and T. S. Jespersen, "Epitaxy of semiconductor-superconductor nanowires", *Nature Materials*, vol. 14, 400 EP –, 2015, Article. DOI: 10.1038/nmat4176.
- [38] M. Leijnse and K. Flensberg, "Introduction to topological superconductivity and majorana fermions", *Semiconductor Science and Technology*, vol. 27, no. 12, p. 124003, 2012. DOI: 10.1088/0268-1242/27/12/124003.
- [39] S. R. Plissard, D. R. Slapak, M. A. Verheijen, M. Hocevar, G. W. G. Immink, I. van Weperen, S. Nadj-Perge, S. M. Frolov, L. P. Kouwenhoven, and E. P.A. M. Bakkers, "From insb nanowires to nanocubes: Looking for the sweet spot", *Nano Letters*, vol. 12, no. 4, pp. 1794–1798, 2012. DOI: 10.1021/nl203846g.
- [40] S. M. Albrecht, A. P. Higginbotham, M. Madsen, F. Kuemmeth, T. S. Jespersen, J. Nygård, P. Krogstrup, and C. M. Marcus, "Exponential protection of zero modes in majorana islands", *Nature*, vol. 531, 206 EP –, 2016. DOI: 10.1038/nature17162.

- [41] S. Gazibegovic, D. Car, H. Zhang, S. C. Balk, J. A. Logan, M. W. A. de Moor, M. C. Cassidy, R. Schmits, D. Xu, G. Wang, P. Krogstrup, R. L. M. Op het Veld, K. Zuo, Y. Vos, J. Shen, D. Bouman, B. Shojaei, D. Pennachio, J. S. Lee, P. J. van Veldhoven, S. Koelling, M. A. Verheijen, L. P. Kouwenhoven, C. J. Palmstrøm, and E. P.A. M. Bakkers, “Epitaxy of advanced nanowire quantum devices”, *Nature*, vol. 548, 434 EP –, 2017. DOI: [10.1038/nature23468](https://doi.org/10.1038/nature23468).
- [42] R. M. Lutchyn, T. D. Stanescu, and S. Das Sarma, “Search for majorana fermions in multiband semiconducting nanowires”, *Phys. Rev. Lett.*, vol. 106, p. 127 001, 12 2011. DOI: [10.1103/PhysRevLett.106.127001](https://doi.org/10.1103/PhysRevLett.106.127001).
- [43] B. Nijholt and A. R. Akhmerov, “Orbital effect of magnetic field on the majorana phase diagram”, *Phys. Rev. B*, vol. 93, p. 235 434, 23 2016. DOI: [10.1103/PhysRevB.93.235434](https://doi.org/10.1103/PhysRevB.93.235434).
- [44] A. E. Antipov, A. Bargerbos, G. W. Winkler, B. Bauer, E. Rossi, and R. M. Lutchyn, “Effects of gate-induced electric fields on semiconductor majorana nanowires”, *Phys. Rev. X*, vol. 8, p. 031 041, 3 2018. DOI: [10.1103/PhysRevX.8.031041](https://doi.org/10.1103/PhysRevX.8.031041).
- [45] G. W. Winkler, A. E. Antipov, B. van Heck, A. A. Soluyanov, L. I. Glazman, M. Wimmer, and R. M. Lutchyn, “A unified numerical approach to semiconductor-superconductor heterostructures”, *ArXiv e-prints*, arXiv:1810.04180, Oct. 2018. [Online]. Available: <https://arxiv.org/abs/1810.04180>.
- [46] G. W. Winkler, D. Varjas, R. Skolasinski, A. A. Soluyanov, M. Troyer, and M. Wimmer, “Orbital contributions to the electron g factor in semiconductor nanowires”, *Phys. Rev. Lett.*, vol. 119, p. 037 701, 3 2017. DOI: [10.1103/PhysRevLett.119.037701](https://doi.org/10.1103/PhysRevLett.119.037701).
- [47] , M.-T. Deng, J. Nygård, P. Krogstrup, and C. M. Marcus, “Effective g factor of subgap states in hybrid nanowires”, *Phys. Rev. Lett.*, vol. 121, p. 037 703, 3 2018. DOI: [10.1103/PhysRevLett.121.037703](https://doi.org/10.1103/PhysRevLett.121.037703).
- [48] V. Mourik and K. Zuo, “Signatures of majorana fermions in hybrid superconductor-semiconductor nanowire devices”, PhD thesis, TU Delft, 2016. DOI: [10.4233/uuid:3fd0aed5-000c-4e50-a772-269436637fc4](https://doi.org/10.4233/uuid:3fd0aed5-000c-4e50-a772-269436637fc4).
- [49] H. Zhang, C.-X. Liu, S. Gazibegovic, D. Xu, J. A. Logan, G. Wang, N. van Loo, J. D. S. Bommer, M. W. A. de Moor, D. Car, R. L. M. Op het Veld, P. J. van Veldhoven, S. Koelling, M. A. Verheijen, M. Pendharkar, D. J. Pennachio, B. Shojaei, J. S. Lee, C. J. Palmstrøm, E. P.A. M. Bakkers, S. D. Sarma, and L. P. Kouwenhoven, “Quantized majorana conductance”, *Nature*, vol. 556, 74 EP –, 2018. DOI: [10.1038/nature26142](https://doi.org/10.1038/nature26142).
- [50] C.-X. Liu, J. D. Sau, T. D. Stanescu, and S. Das Sarma, “Andreev bound states versus majorana bound states in quantum dot-nanowire-superconductor hybrid structures: Trivial versus topological zero-bias conductance peaks”, *Phys. Rev. B*, vol. 96, p. 075 161, 7 2017. DOI: [10.1103/PhysRevB.96.075161](https://doi.org/10.1103/PhysRevB.96.075161).
- [51] C.-X. Liu, J. D. Sau, and S. Das Sarma, “Distinguishing topological majorana bound states from trivial andreev bound states: Proposed tests through differential tunneling conductance spectroscopy”, *Phys. Rev. B*, vol. 97, p. 214 502, 21 2018. DOI: [10.1103/PhysRevB.97.214502](https://doi.org/10.1103/PhysRevB.97.214502).
- [52] L. Fu and C. L. Kane, “Josephson current and noise at a superconductor/quantum-spin-hall-insulator/superconductor junction”, *Phys. Rev. B*, vol. 79, p. 161 408, 16 2009. DOI: [10.1103/PhysRevB.79.161408](https://doi.org/10.1103/PhysRevB.79.161408).

- [53] L. Jiang, D. Pekker, J. Alicea, G. Refael, Y. Oreg, and F. von Oppen, "Unconventional josephson signatures of majorana bound states", *Phys. Rev. Lett.*, vol. 107, p. 236401, 23 2011. DOI: [10.1103/PhysRevLett.107.236401](https://doi.org/10.1103/PhysRevLett.107.236401).
- [54] D. Laroche, D. Bouman, D. J. van Woerkom, A. Proutski, C. Murthy, D. I. Pikulin, C. Nayak, R. J. J. van Gulik, J. Nygård, P. Krogstrup, L. P. Kouwenhoven, and A. Geresdi, "Observation of the 4π -periodic Josephson effect in InAs nanowires", *ArXiv:1712.08459*, 2017. [Online]. Available: <https://arxiv.org/abs/1712.08459>.
- [55] Y. Makhlin, G. Schön, and A. Shnirman, "Quantum-state engineering with josephson-junction devices", *Rev. Mod. Phys.*, vol. 73, pp. 357–400, 2 2001. DOI: [10.1103/RevModPhys.73.357](https://doi.org/10.1103/RevModPhys.73.357).
- [56] Y. Nakamura, Y. A. Pashkin, and J. S. Tsai, "Coherent control of macroscopic quantum states in a single-cooper-pair box", *Nature*, vol. 398, 786 EP –, 1999. DOI: [10.1038/19718](https://doi.org/10.1038/19718).
- [57] J. M. Martinis, S. Nam, J. Aumentado, and C. Urbina, "Rabi oscillations in a large josephson-junction qubit", *Phys. Rev. Lett.*, vol. 89, p. 117901, 11 2002. DOI: [10.1103/PhysRevLett.89.117901](https://doi.org/10.1103/PhysRevLett.89.117901).
- [58] C. H. van der Wal, A. C. J. ter Haar, F. K. Wilhelm, R. N. Schouten, C. J.P. M. Harmans, T. P. Orlando, S. Lloyd, and J. E. Mooij, "Quantum superposition of macroscopic persistent-current states", *Science*, vol. 290, no. 5492, pp. 773–777, 2000. DOI: [10.1126/science.290.5492.773](https://doi.org/10.1126/science.290.5492.773).
- [59] A. Blais, R.-S. Huang, A. Wallraff, S. M. Girvin, and R. J. Schoelkopf, "Cavity quantum electrodynamics for superconducting electrical circuits: An architecture for quantum computation", *Phys. Rev. A*, vol. 69, p. 062320, 6 2004. DOI: [10.1103/PhysRevA.69.062320](https://doi.org/10.1103/PhysRevA.69.062320).
- [60] S. M. Girvin, "Circuit qed: Superconducting qubits coupled to microwave photons", *Lecture Notes of the 12th Capri Spring School on Transport in Nanostructures*, 2016. [Online]. Available: http://www.capri-school.eu/capri16/lectureres/master_cqed_les_houches.pdf.
- [61] U. Vool and M. Devoret, "Introduction to quantum electromagnetic circuits", *International Journal of Circuit Theory and Applications*, vol. 45, no. 7, pp. 897–934, 2017. DOI: [10.1002/cta.2359](https://doi.org/10.1002/cta.2359).
- [62] J. Koch, T. M. Yu, J. Gambetta, A. A. Houck, D. I. Schuster, J. Majer, A. Blais, M. H. Devoret, S. M. Girvin, and R. J. Schoelkopf, "Charge-insensitive qubit design derived from the cooper pair box", *Phys. Rev. A*, vol. 76, p. 042319, 4 2007. DOI: [10.1103/PhysRevA.76.042319](https://doi.org/10.1103/PhysRevA.76.042319).
- [63] J. Majer, J. M. Chow, J. M. Gambetta, J. Koch, B. R. Johnson, J. A. Schreier, L. Frunzio, D. I. Schuster, A. A. Houck, A. Wallraff, A. Blais, M. H. Devoret, S. M. Girvin, and R. J. Schoelkopf, "Coupling superconducting qubits via a cavity bus", *Nature*, vol. 449, 443 EP –, 2007. DOI: [10.1038/nature06184](https://doi.org/10.1038/nature06184).
- [64] A. Blais, J. Gambetta, A. Wallraff, D. I. Schuster, S. M. Girvin, M. H. Devoret, and R. J. Schoelkopf, "Quantum-information processing with circuit quantum electrodynamics", *Phys. Rev. A*, vol. 75, p. 032329, 3 2007. DOI: [10.1103/PhysRevA.75.032329](https://doi.org/10.1103/PhysRevA.75.032329).
- [65] L. DiCarlo, J. M. Chow, J. M. Gambetta, L. S. Bishop, B. R. Johnson, D. I. Schuster, J. Majer, A. Blais, L. Frunzio, S. M. Girvin, and R. J. Schoelkopf, "Demonstration of two-qubit algorithms with a superconducting quantum processor", *Nature*, vol. 460, 240 EP –, 2009. DOI: [10.1038/nature08121](https://doi.org/10.1038/nature08121).

- [66] J. Koch, V. Manucharyan, M. H. Devoret, and L. I. Glazman, "Charging effects in the inductively shunted josephson junction", *Phys. Rev. Lett.*, vol. 103, p. 217004, 21 2009. DOI: 10.1103/PhysRevLett.103.217004.
- [67] M. Tinkham and M. Gordon, "Introduction to superconductivity. second edition.", *McGraw-Hill New York.*, 1996.
- [68] A. Shnirman, G. Schön, and Z. Hermon, "Quantum manipulations of small josephson junctions", *Phys. Rev. Lett.*, vol. 79, pp. 2371–2374, 12 1997. DOI: 10.1103/PhysRevLett.79.2371.
- [69] V Bouchiat, D Vion, P Joyez, D Esteve, and M. H. Devoret, "Quantum coherence with a single cooper pair", *Physica Scripta*, vol. 1998, no. T76, p. 165, 1998. [Online]. Available: <http://stacks.iop.org/1402-4896/1998/i=T76/a=024>.
- [70] J. E. Mooij, T. P. Orlando, L. Levitov, L. Tian, C. H. van der Wal, and S. Lloyd, "Josephson persistent-current qubit", *Science*, vol. 285, no. 5430, pp. 1036–1039, 1999, ISSN: 0036-8075. DOI: 10.1126/science.285.5430.1036.
- [71] I. Chiorescu, Y. Nakamura, C. J.P. M. Harmans, and J. E. Mooij, "Coherent quantum dynamics of a superconducting flux qubit", *Science*, vol. 299, no. 5614, pp. 1869–1871, 2003, ISSN: 0036-8075. DOI: 10.1126/science.1081045.
- [72] G. Zhu, D. G. Ferguson, V. E. Manucharyan, and J. Koch, "Circuit qed with fluxonium qubits: Theory of the dispersive regime", *Phys. Rev. B*, vol. 87, p. 024510, 2 2013. DOI: 10.1103/PhysRevB.87.024510.
- [73] A. Wallraff, D. I. Schuster, A. Blais, L. Frunzio, R.-S. Huang, J. Majer, S. Kumar, S. M. Girvin, and R. J. Schoelkopf, "Strong coupling of a single photon to a superconducting qubit using circuit quantum electrodynamics", *Nature*, vol. 431, 162 EP –, 2004. DOI: 10.1038/nature02851.
- [74] V. E. Manucharyan, "Superinductance", PhD thesis, Yale University, 2012. [Online]. Available: [http://qulab.eng.yale.edu/documents/theses/Manucharyan,%20Vladimir%20-%20Superinductance%20\(Yale,%202012\).pdf](http://qulab.eng.yale.edu/documents/theses/Manucharyan,%20Vladimir%20-%20Superinductance%20(Yale,%202012).pdf).
- [75] V. E. Manucharyan, "Fluxonium qubit", *Lecture Notes of the 44th IFF Spring School: Quantum information processing*, vol. D1, 2013. [Online]. Available: http://www.fz-juelich.de/SharedDocs/Downloads/PFI/EN/SpringSchool/Lecture-Notes-Book-Form/Skriptbuch-2013.pdf?__blob=publicationFile.
- [76] N. A. Masluk, "Reducing the losses of the fluxonium artificial atom", PhD thesis, Yale University, 2012. [Online]. Available: [http://qulab.eng.yale.edu/documents/theses/Masluk,%20Nicholas%20A.%20-%20Reducing%20the%20losses%20of%20the%20fluxonium%20artificial%20atom%20\(Yale,%202012\).pdf](http://qulab.eng.yale.edu/documents/theses/Masluk,%20Nicholas%20A.%20-%20Reducing%20the%20losses%20of%20the%20fluxonium%20artificial%20atom%20(Yale,%202012).pdf).
- [77] I. M. Pop, K. Geerlings, G. Catelani, R. J. Schoelkopf, L. I. Glazman, and M. H. Devoret, "Coherent suppression of electromagnetic dissipation due to superconducting quasiparticles", *Nature*, vol. 508, 369 EP –, 2014. DOI: 10.1038/nature13017.
- [78] W. C. Smith, A. Kou, U. Vool, I. M. Pop, L. Frunzio, R. J. Schoelkopf, and M. H. Devoret, "Quantization of inductively shunted superconducting circuits", *Phys. Rev. B*, vol. 94, p. 144507, 14 2016. DOI: 10.1103/PhysRevB.94.144507.

- [79] G. de Lange, B. van Heck, A. Bruno, D. J. van Woerkom, A. Geresdi, S. R. Plissard, E. P.A. M. Bakkers, A. R. Akhmerov, and L. DiCarlo, "Realization of microwave quantum circuits using hybrid superconducting-semiconducting nanowire josephson elements", *Phys. Rev. Lett.*, vol. 115, p. 127 002, 12 2015. DOI: [10.1103/PhysRevLett.115.127002](https://doi.org/10.1103/PhysRevLett.115.127002).
- [80] T. W. Larsen, K. D. Petersson, F. Kuemmeth, T. S. Jespersen, P. Krogstrup, J. Nygård, and C. M. Marcus, "Semiconductor-nanowire-based superconducting qubit", *Phys. Rev. Lett.*, vol. 115, p. 127 001, 12 2015. DOI: [10.1103/PhysRevLett.115.127001](https://doi.org/10.1103/PhysRevLett.115.127001).
- [81] L. Casparis, T. W. Larsen, M. S. Olsen, F. Kuemmeth, P. Krogstrup, J. Nygård, K. D. Petersson, and C. M. Marcus, "Gatemon benchmarking and two-qubit operations", *Phys. Rev. Lett.*, vol. 116, p. 150 505, 15 2016. DOI: [10.1103/PhysRevLett.116.150505](https://doi.org/10.1103/PhysRevLett.116.150505).
- [82] F. Luthi, T. Stavenga, O. W. Enzing, A. Bruno, C. Dickel, N. K. Langford, M. A. Rol, T. S. Jespersen, J. Nygård, P. Krogstrup, and L. DiCarlo, "Evolution of nanowire transmon qubits and their coherence in a magnetic field", *Phys. Rev. Lett.*, vol. 120, p. 100 502, 10 2018. DOI: [10.1103/PhysRevLett.120.100502](https://doi.org/10.1103/PhysRevLett.120.100502).
- [83] A. F. Andreev, "The thermal conductivity of the intermediate state in superconductors", *ZhETF*, vol. 46, p. 1823, 5 1964. [Online]. Available: http://www.jetp.ac.ru/cgi-bin/dn/e_019_05_1228.pdf.
- [84] L. Bretheau, "Localized excitations in superconducting atomic contacts: Probing the andreev doublet", PhD thesis, Ecole Polytechnique, 2013. [Online]. Available: https://pastel.archives-ouvertes.fr/file/index/docid/862029/filename/Bretheau_Thesis.pdf.
- [85] D. J. van Woerkom, A. Proutski, B. van Heck, D. Bouman, J. I. Väyrynen, L. I. Glazman, P. Krogstrup, J. Nygård, L. P. Kouwenhoven, and A. Geresdi, "Microwave spectroscopy of spinful andreev bound states in ballistic semiconductor josephson junctions", *Nature Physics*, vol. 13, 2017. DOI: [10.1038/nphys4150](https://doi.org/10.1038/nphys4150).
- [86] K. Zuo, V. Mourik, D. B. Szombati, B. Nijholt, D. J. van Woerkom, A. Geresdi, J. Chen, V. P. Ostroukh, A. R. Akhmerov, S. R. Plissard, D. Car, E. P.A. M. Bakkers, D. I. Pikulin, L. P. Kouwenhoven, and S. M. Frolov, "Supercurrent interference in few-mode nanowire josephson junctions", *Phys. Rev. Lett.*, vol. 119, p. 187 704, 18 2017. DOI: [10.1103/PhysRevLett.119.187704](https://doi.org/10.1103/PhysRevLett.119.187704).
- [87] L. Bretheau, Ç. Ö. Girit, H. Pothier, D. Esteve, and C. Urbina, "Exciting andreev pairs in a superconducting atomic contact", *Nature*, vol. 499, 312 EP –, 2013. DOI: [10.1038/nature12315](https://doi.org/10.1038/nature12315).
- [88] B. van Heck, J. I. Väyrynen, and L. I. Glazman, "Zeeman and spin-orbit effects in the andreev spectra of nanowire junctions", *Phys. Rev. B*, vol. 96, p. 075 404, 7 2017. DOI: [10.1103/PhysRevB.96.075404](https://doi.org/10.1103/PhysRevB.96.075404).
- [89] M. Hays, G. de Lange, K. Serniak, D. J. van Woerkom, D. Bouman, P. Krogstrup, J. Nygård, A. Geresdi, and M. H. Devoret, "Direct microwave measurement of andreev-bound-state dynamics in a semiconductor-nanowire josephson junction", *Phys. Rev. Lett.*, vol. 121, p. 047 001, 4 2018. DOI: [10.1103/PhysRevLett.121.047001](https://doi.org/10.1103/PhysRevLett.121.047001).

- [90] A. J. Annunziata, D. F. Santavicca, L. Frunzio, G. Catelani, M. J. Rooks, A. Frydman, and D. E. Prober, "Tunable superconducting nanoinductors", *Nanotechnology*, vol. 21, no. 44, p. 445 202, 2010. DOI: doi.org/10.1088/0957-4484/21/44/445202.
- [91] N. A. Masluk, I. M. Pop, A. Kamal, Z. K. Mineev, and M. H. Devoret, "Microwave characterization of josephson junction arrays: Implementing a low loss superinductance", *Phys. Rev. Lett.*, vol. 109, p. 137 002, 13 2012. DOI: [10.1103/PhysRevLett.109.137002](https://doi.org/10.1103/PhysRevLett.109.137002).
- [92] J. E. Mooij and Y. V. Nazarov, "Superconducting nanowires as quantum phase-slip junctions", *Nature Physics*, vol. 2, 169 EP –, 2006. DOI: [10.1038/nphys234](https://doi.org/10.1038/nphys234).
- [93] T. M. Hazard, A. Gyenis, A. Di Paolo, A. T. Asfaw, S. A. Lyon, A. Blais, and A. A. Houck, "Nanowire superinductance fluxonium qubit", *ArXiv:1805.00938*, 2018. [Online]. Available: <https://arxiv.org/abs/1805.00938>.
- [94] N. Samkharadze, A. Bruno, P. Scarlino, G. Zheng, D. P. DiVincenzo, L. DiCarlo, and L. M. K. Vandersypen, "High-kinetic-inductance superconducting nanowire resonators for circuit qed in a magnetic field", *Phys. Rev. Applied*, vol. 5, p. 044 004, 4 2016. DOI: [10.1103/PhysRevApplied.5.044004](https://doi.org/10.1103/PhysRevApplied.5.044004).
- [95] A. Shearrow, G. Koolstra, S. J. Whiteley, N. Earnest, P. S. Barry, F. J. Heremans, D. D. Awschalom, E. Shirokoff, and D. I. Schuster, "Atomic layer deposition of titanium nitride for quantum circuits featured", *Appl. Phys. Lett.*, vol. 113, p. 212 601, 2018. DOI: [10.1063/1.5053461](https://doi.org/10.1063/1.5053461).
- [96] M. S. Khalil, M. J. A. Stoutimore, F. C. Wellstood, and K. D. Osborn, "An analysis method for asymmetric resonator transmission applied to superconducting devices", *Journal of Applied Physics*, vol. 111, no. 5, p. 054 510, 2012. [Online]. Available: <https://aip.scitation.org/doi/10.1063/1.3692073>.
- [97] D. Bothner, T. Gaber, M. Kemmler, D. Koelle, and R. Kleiner, "Improving the performance of superconducting microwave resonators in magnetic fields", *Applied Physics Letters*, vol. 98, no. 10, p. 102 504, 2011. DOI: [10.1063/1.3560480](https://doi.org/10.1063/1.3560480).
- [98] D. Bothner, C. Clauss, E. Koroknay, M. Kemmler, T. Gaber, M. Jetter, M. Scheffler, P. Michler, M. Dressel, D. Koelle, and R. Kleiner, "Reducing vortex losses in superconducting microwave resonators with microsphere patterned antidot arrays", *Applied Physics Letters*, vol. 100, no. 1, p. 012 601, 2012. DOI: [10.1063/1.3673869](https://doi.org/10.1063/1.3673869).
- [99] J. G. Kroll, F. Borsoi, K. L. van der Enden, W. Uilhoorn, D. de Jong, M. Quintero-Pérez, D. J. van Woerkom, A. Bruno, S. R. Plissard, D. Car, E. P.A. M. Bakkers, M. C. Cassidy, and L. P. Kouwenhoven, "Magnetic field resilient superconducting coplanar waveguide resonators for hybrid cqed experiments", *ArXiv:1809.03932v1*, 2018. [Online]. Available: <http://arxiv.org/abs/1809.03932>.
- [100] J. R. Clem, "Vortex Exclusion from Superconducting Strips and SQUIDs in Weak Perpendicular Ambient Magnetic Fields", *APS March Meeting Abstracts*, K36.06, K36.06, 1998. [Online]. Available: <http://adsabs.harvard.edu/abs/1998APS..MAR.K3606C>.
- [101] G. Stan, S. B. Field, and J. M. Martinis, "Critical field for complete vortex expulsion from narrow superconducting strips", *Phys. Rev. Lett.*, vol. 92, p. 097 003, 9 2004. DOI: [10.1103/PhysRevLett.92.097003](https://doi.org/10.1103/PhysRevLett.92.097003).

- [102] K. H. Kuit, J. R. Kirtley, W. van der Veur, C. G. Molenaar, F. J. G. Roesthuis, A. G. P. Troeman, J. R. Clem, H. Hilgenkamp, H. Rogalla, and J. Flokstra, "Vortex trapping and expulsion in thin-film $\text{YBa}_2\text{Cu}_3\text{O}_{7-\delta}$ strips", *Phys. Rev. B*, vol. 77, p. 134504, 13 2008. DOI: [10.1103/PhysRevB.77.134504](https://doi.org/10.1103/PhysRevB.77.134504).
- [103] H. Bartolf, "Fluctuation mechanisms in superconductors", *Springer Spektrum*, 2016. DOI: [10.1007/978-3-658-12246-1_10](https://doi.org/10.1007/978-3-658-12246-1_10).
- [104] A. Chulliat, S. Macmillan, P. Alken, C. Beggan, M. Nair, B. Hamilton, A. Woods, V. Ridley, S. Maus, and A. Thomson, "The US/UK World Magnetic Model for 2015-2020", *Technical Report, National Geophysical Data Center, NOAA*, 2015. [Online]. Available: https://www.ngdc.noaa.gov/geomag/WMM/data/WMM2015/WMM2015_Report.pdf.
- [105] C. Macklin, K. O'Brien, D. Hover, M. E. Schwartz, V. Bolkhovskiy, X. Zhang, W. D. Oliver, and I. Siddiqi, "A near-quantum-limited josephson traveling-wave parametric amplifier", *Science*, vol. 350, no. 6258, pp. 307–310, 2015, ISSN: 0036-8075. DOI: [10.1126/science.aaa8525](https://doi.org/10.1126/science.aaa8525).
- [106] O. Yaakobi, L. Friedland, C. Macklin, and I. Siddiqi, "Parametric amplification in josephson junction embedded transmission lines", *Phys. Rev. B*, vol. 87, p. 144301, 14 2013. DOI: [10.1103/PhysRevB.87.144301](https://doi.org/10.1103/PhysRevB.87.144301).
- [107] P. Aseev, A. Fursina, F. Boekhout, F. Krizek, J. E. Sestoft, F. Borsoi, S. Heedt, G. Wang, L. Binci, S. Martí-Sánchez, T. Swoboda, R. Koops, E. Uccelli, J. Arbiol, P. Krogstrup, L. P. Kouwenhoven, and P. Caroff, "Selectivity map for molecular beam epitaxy of advanced iii-v quantum nanowire networks", *Nano Lett*, vol. 19, no. 1, pp. 218–227, 2018, 30521341[pmid], ISSN: 1530-6992. DOI: [10.1021/acs.nanolett.8b03733](https://doi.org/10.1021/acs.nanolett.8b03733).